Lab-on-a-Chip Designs for Airborne Spore Detection: Towards the Forecasting of Sclerotinia Stem Rot of Canola

by

Pedro Alejandro Duarte Riveros

A thesis submitted in partial fulfillment of the requirements for the degree of

Doctor of Philosophy

in

Biomedical Engineering

Department of Electrical and Computer Engineering

University of Alberta

Abstract

Sclerotinia stem rot (SSR), caused by the necrotrophic fungal pathogen *Sclerotinia sclerotiorum*, is one of the most devastating diseases affecting crops. More than 400 plant species around the globe are affected by this fungus. In canola, one of Canada's most important crops, yield losses due to SSR can be as high as 50%. Although chemical control with fungicides is currently the most common tool for the management of SSR, the routine application without prior information about the risk of the disease development is also financially inefficient. The early prognosis of an outbreak is critical to avoid the severe economic losses caused by SSR and can be achieved by the detection of a small number of *S. sclerotiorum* airborne ascospores, one of the main agents of infection in stem rot. However, the current lack of simple and effective methods to detect fungal airborne pathogens has hindered the development of an accurate early warning system.

In this thesis, we explored the design and development of lab-on-a-chip devices for the detection of *S. sclerotiorum* ascospores, aiming at their future integration with spore-trap samplers into an effective SSR forecasting system. Our first design is based on a Coulter counter approach, which consists of a microfluidic chip capable of quantifying single ascospores flowing in a microchannel. The target ascospores are injected into the device and selectively captured by dielectrophoresis, while other particles in the sample are flushed away to the outlet drain of the device. Subsequently, the target ascospores are released into the flow stream of the device and are detected when flowing through a constriction employing dynamic impedimetric sensing. Experimental results indicated a

0.3% change in the impedance signal produced by individual ascospores, which were detected using a benchtop potentiostat.

In our second approach, we developed a microfluidic device that contains a nano-thick aluminum electrode structure integrated with a picoliter well array for dielectrophoresis-driven capture of ascospores and on-chip quantitative detection employing static impedimetric sensing. Based on experimental results, we demonstrated a highly efficient ascospore trapping rate of more than 90% with an effective impedimetric sensing method that allowed the ascospore quantification of each column in the array and achieved a sensitivity of 2%/ascospore at 5 kHz and 1.6%/ascospore at 20 kHz, enabling single ascospore detection.

Finally, the dielectric properties of *S. sclerotiorum* ascospores were determined experimentally employing a microfluidic platform containing interdigitated aluminum microelectrodes. The dielectric properties of ascospores are of major importance for the development of dielectrophoretic filters, as it provides information about the dielectrophoretic response of the ascospores without the need for long iterative testing. The dielectric properties of ascospores were determined in media of different conductivities and they were modeled using a realistic ellipsoidal double-shell model based on the multi-shell theory. To validate the methodology and analysis, the dielectric properties of human embryonic kidney (HEK-293) cells were also determined and compared to values reported in the literature.

We envision that the devices proposed in this thesis will contribute to the development of a low-cost, miniaturized, and automated platform technology that can be integrated into an infectious plant disease forecasting tool for canola crop protection.

Preface

This thesis is an original work by Pedro Alejandro Duarte Riveros. Credit to work not conducted by the author himself and acknowledgments were given throughout the thesis in the form of footnotes. Most of the research work described in the chapters of this thesis has been published in authored and co-authored articles.

Parts of chapters 1 and 2 of this thesis have been published as: P. A. Duarte, L. Menze, G. N. Abdelrasoul, S. Yosinki, Z. Kobos, R. Stuermer, M. Reed, J. Yang, X. Li, and J. Chen, "Single ascospore detection for the forecasting of Sclerotinia stem rot of canola", Lab on Chip, DOI: 0.1039/d0lc00426j, Copyright 2020 Royal Society of Chemistry. I was responsible for the design, fabrication and testing of microfluidic devices. I was also responsible for designing and performing the experiments, data collection and analysis, as well as manuscript composition. L. Menze and R. Stuermer assisted with formal analysis, device testing and manuscript editing. G. N. Abdelrasoul assisted with device fabrication and manuscript editing. S. Yosinki and Z. Kobos assisted with interpretation of the results and manuscript editing. J. Yang, and X. Li provided spore cultures and valuable guidance on the SSR cycle. M. Reed and J. Chen were the supervisory authors, provided funding, and contributed to manuscript edits.

Parts of chapter 3 of this thesis has been published as: P. A. Duarte, L. Menze, L. Shoute, J. Zeng, O. Savchenko, J. Lyu and J. Chen, "Highly Efficient Capture and Quantification of the Airborne Fungal Pathogen *Sclerotinia sclerotiorum* Employing a Nanoelectrode-Activated Microwell

Array", ACS Omega, DOI: 10.1021/acsomega.1c04878, Copyright 2021 American Chemical Society. I was responsible for the design, fabrication and testing of the microfluidic device. I was also responsible for designing and performing the experiments, data collection and analysis, as well as manuscript composition. L. Menze helped with device testing, interpretation of results and manuscript editing. L. Shoute and J. Lyu helped with device fabrication. J. Zeng and O. Savchenko assisted with sample preparation for imaging and manuscript edits. J. Chen was the supervisory author, provided funding, and contributed to data analysis and manuscript edits. A part of chapter 3 was also published as: L. Menze, P. A. Duarte, L. Haddon, M. Chu, and J. Chen, "Selective Single-Cell Sorting Using a Multisectorial Electroactive Nanowell Platform", ACS nano, DOI:10.1021/acsnano.1c05668, Copyright 2021 American Chemical Society. L. Menze was the main responsible for the cell sorting project, the design, fabrication and testing of the device, as well as performing experiments, data collection, analysis, and manuscript composition. I contributed with the design, assembly, fabrication, and integration of the device. I also designed the experiments and helped with the interpretation of results and with manuscript edits. L. Haddon helped with cell culture, staining and manuscript edits. M. Chu and J. Chen were the supervisory authors, provided funding, and contributed to manuscript edits.

Chapter 4 of this thesis contains research work of an article recently submitted for revision to Lab on Chip as: P. A. Duarte, L. Menze, Z. Tian, O. Savchenko, B. Li and J. Chen, "Dielectric analysis of *Sclerotinia sclerotiorum* airborne inoculum by the measurement of dielectrophoretic trapping voltages using a microfluidic platform". I was responsible for the design, fabrication and testing of the microfluidic device. I was also responsible for performing the experiments, data collection and analysis, as well as manuscript composition. L. Menze helped with device testing and manuscript edits. Z. Tian helped with COMSOL simulations, cell culture and manuscript edits. O.

Acknowledgement

Contents

List of Tables

List of Figures

List of Acronyms

AC Alternating current

APTES (3-Aminopropyl)triethoxysilane

BSA Bovine serum albumin

CAD Computer aided design

CCD Charged coupled device

CM Clausius Mossotti

CV Coefficient of variation

DDS Direct digital synthesizer

DEP Dielectrophoresis

EIS Electrochemical impedance spectroscopy

FFC Flat flex cable

HEK Human embryonic kidney

HIM Helium ion microscopy

IME Interdigitated microelectrodes

IPA Isopropyl alcohol

PDMS Polydimethylsiloxane

PBS Phosphate buffer saline

PCB Printed circuit board

PCR Polymerase chain reaction

PDA Potato dextrose agar

PDMS Polydimethylsiloxane

PR Photoresist

RMS Root mean squared

SPST Single pole single throw

SSR Sclerotinia stem rot

TEM Transmission electron microscopy

VPP Peak to peak voltage

Chapter 1

Introduction

1.1 The Disease

Sclerotinia stem rot (SSR), caused by the necrotrophic fungal pathogen *Sclerotinia sclerotiorum* (Lib.) de Bary*,* is a destructive disease of canola (*Brassica napus*), one of the most widely cultivated crops in Canada [1]–[3]. Canola is a profitable crop, with a huge impact on the Canadian economy, as well as on countries like China, and India, the three largest canola producing countries in the world [4]. In Canada alone, the production of canola generates $26.7 billion annually [5], with an increase in production from about 12.7 million tons in 2010 to 20.4 million tons in 2018 [6]. To date, SSR is one of the major threats to the production of canola, with yield losses that can be as high as 50% when the environmental conditions are conducive to the development of the disease [7].

Sclerotinia sclerotiorum is a soil-born pathogen that affects over 400 plant species from 75 different families, including several economically important crops such as lettuce, carrot, lentils, mustard, and canola [1], [8]. The fungus has been reported all over the world, although it is more prevalent in temperate regions with cool and wet seasons [1]. Around 90% of the fungus' life cycle is spent as small structures called sclerotia, which are formed from aggregates of mycelium and

can survive in the soil for years. Sclerotia are dark in color due to the presence of melanin, which has been suggested to play a major role in the protection against adverse conditions in many fungi [9]. Under suitable environmental conditions, such as saturated soil and cool environments, sclerotia can germinate either myceliogenically or carpogenically [1], [8], [10]. The myceliogenic germination of sclerotia gives rise to mycelium, which can infect plants directly through the soil. Infection through myceliogenic germination occurs only in a few crops, like sunflower, and it is not the primary mode of canola infection [1], [11]. Sclerotia germinate carpogenically to produce mushroom-like structures called apothecia that can generate millions of microscopic airborne spores (ascospores) that can travel from field-to-field following wind currents[1] [1], [12], [13]. Researchers reported that, on average, 2 million ascospores can be released per apothecium over a period of 8 days, with a maximum recorded number of 30 million ascospores per apothecium [13]. Distances traveled by ascospores have been reported to vary from 100 m to several kilometers [14] and pollinating bees have been suggested to contribute to the even further dispersal of ascospores [15]. Since carpogenic germination has been observed as the primary mode of sclerotia germination in the field [16], the infection of canola plants occurs mainly due to ascospores, which land on the plant petals and germinate once they fall onto leaves, stems, and branches, producing abundant white mycelium, which penetrate the stem tissue. The infected plant then will again produce sclerotia within the stem, which return to the soil during harvest, thus completing the disease cycle [12]. The first visual symptoms of SSR appear as watery lesions on leaves and branches. The lesions expand becoming bleached (greyish white) in appearance, the reason for which SSR is commonly known as white mould. Figure 1.1 illustrates the cycle of SSR in canola plants.

---

[1] Throughout this thesis, the terms ascospore and spore are used interchangeably.
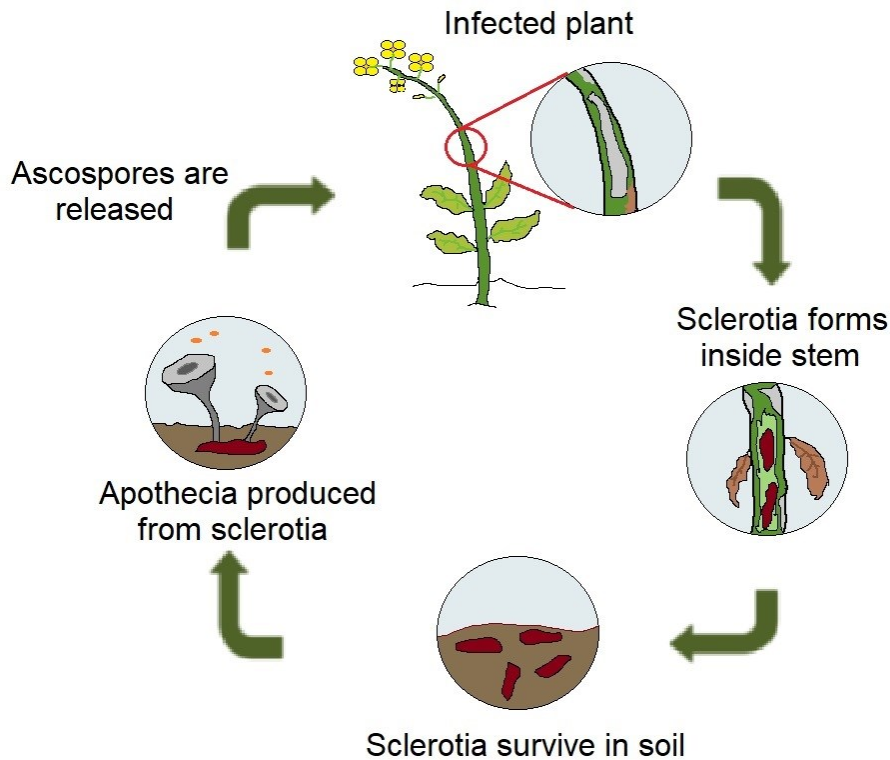
Figure 1.1: Cycle of Sclerotinia stem rot of canola. Figure was inspired and redrawn from [17].

1.2 Management of SSR in Canola

The two primary methods for the management of SSR are based on cultural and chemical control practices. Within cultural control, crop rotation with non-host species is the most common alternative employed by farmers. The goal of crop rotation is to reduce the amount of inoculum present in the field, mainly the density of sclerotia, so that infection of canola crops can be avoided or at least reduced in future years [2]. However, since sclerotia can survive in the soil for up to 7 years [10], [12], crop rotation is not very effective as a disease control measure. Furthermore, canola plants can still get infected, even without the in-field presence of sclerotia, due to

ascospores coming from external fields in wind currents [18]. In addition, the wide host range of *S. sclerotiorum* can contribute to maintaining the levels of sclerotia through the presence of susceptible weeds or plants other than canola [8]. Tillage of the soil is another alternative within cultural control that has been suggested as a tool for the management of SSR [19]. The goal of tillage is to bury sclerotia to avoid its germination. However, the efficiency of tillage as a management tool for SSR has not yet been effectively demonstrated [20].

In Canada, chemical control employing fungicides is the main strategy for the management of SSR [21], [22]. Although this approach can be highly effective, the application of fungicides is economically inefficient when done routinely and with no indication of the risk of infection. Furthermore, the systematic application of fungicides can also increase the selective pressure on pathogen populations to develop insensitivity. This was the case of the fungicide benomyl, marketed as BenLate, which was previously employed to manage SSR. In Canada, populations of *S. sclerotiorum* have been confirmed to develop insensitivity to this fungicide [20], [23]. Ideally, canola growers must apply fungicides during specific time frames in the flowering stage and only when necessary, that is, when ascospores are present in the field and when environmental conditions are conducive to the development of the disease but before symptoms are visible [21], [24]. Since the prediction of SSR outbreaks is hard to achieve, farmers typically apply fungicides without any objective information on the risk of infection, and their spray decision is typically based solely on their experience and intuition [25]. Due to these limitations, there has been a great interest in developing SSR forecasting systems that can provide farmers with reliable and field-specific information on the risk of disease development, so that they can apply fungicides only when necessary and thus avoid severe economic losses.

4

As *S. sclerotiorum* ascospores are the main source of canola crop infection, it is critically important to develop forecasting systems that can measure the in-field levels of these microscopic organisms in order to accurately predict the risk of SSR outbreaks.

1.3 Thesis Objectives

The main drive of the research presented in this thesis is the development of micromachined devices for the detection, in solution, of *S. sclerotiorum* airborne inoculum. The origin of this project was born many years ago through a collaboration between the Binary Lab, led by Dr. Jie Chen and research scientists from Innotech Alberta, led by Dr. Xiujie Li. The ultimate goal of the project was to develop an SSR forecasting system based on the integration of microdevices and commercially available spore-trap samplers. Clearly, the development of such forecasting system is a complex and ambitious project that requires the integration and collaboration between multidisciplinary fields of study and research backgrounds, including, but not limited to, nano and microfabrication, microfluidic design, crop protection, biology, chemistry, mechanical design, circuit and software design. From an engineering perspective, we can identify three general subsystems or components that will have to be developed: The development of microdevices; Fluidic integration between microdevices and spore-trap samplers; Data processing and communication. Each one of these components will require its own research and development in order to find the best system suitable for Canadian fields. The research work described in this thesis focuses mainly on aspects of device development.

The specific research objectives of this thesis are:

- To develop lab-on-a-chip devices for the detection and quantification of *S. sclerotiorum* airborne inoculum employing dielectrophoresis (DEP) and electrochemical impedance spectroscopy (EIS).

- To develop devices capable of quantifying single *S. sclerotiorum* ascospores in solution, aiming at their integration in SSR forecasting applications.

- To obtain an estimation of the dielectric properties of *S. sclerotiorum* ascospores.

1.4   Literature Review

As described in previous sections, the wide host range of *S. sclerotiorum*, the viability of sclerotia in the soil for many years, and the dispersion of ascospores in wind currents are the main factors for the reduced and limited effectiveness of cultural control practices as management tools for SSR. Although the application of fungicides can be an effective alternative, it is not profitable when applied routinely. Due to these problems, there has been great interest in developing SSR forecasting systems that can provide farmers with reliable information on which they can base their spray decisions. Ideally, and based on the disease triangle, a forecasting system or risk assessment tool should incorporate information on in-field inoculum, a measure of environmental conditions as well as information on the stage of development of the crop (host) [26]. In the following sections, a detailed description of the main strategies and methods that are employed for the forecasting of SSR are presented.

1.4.1   Risk Assessment Checklist

A risk assessment checklist created in Sweden is one of the first methods developed for the forecast of SSR [2]. The risk assessment checklist includes factors such as crop density, SSR incidence in

the last host crop, rain in the last two weeks prior to flowering, and the number of apothecia per 100 sclerotia in the field [2]. Points are assigned to levels within each factor and then added and compared with a threshold to determine if fungicide application is required. This method was tested in Swedish fields, where spray recommendations were given in 75% of the fields that required fungicide application and in 16% of the fields that did not need fungicide application. These percentages changed when the risk point threshold changed. Although the checklist provides a simple and field-specific assessment of SSR risk, it is very time-consuming and labor-intensive. Furthermore, since SSR has been reported in fields with no apothecia [18], the checklist method may not provide an accurate prediction of SSR infection. The Swedish checklist has been adapted to Canadian conditions [27], and similar methods were also developed in Denmark [2] and Germany [28].

1.4.2   Weather-based forecast

Weather-based forecasting systems have also been developed to assess the risk of SSR in canola and other plants. Clarkson et al. [29] developed a mathematical model for *S. sclerotiorum* infection and disease development on lettuce, which incorporates environmental parameters such as relative humidity, and temperature. Measurements of ascospore density in a controlled environment were also added to the model to increase the prediction accuracy. Similarly, Sharma et al. [30] developed a forecasting system for SSR in Indian mustard, incorporating parameters such as temperature, rainfall, soil moisture, relative humidity and hours of sunshine [30]. For the canola case, a forecast system based on weather maps has also been developed and employed in the prairie provinces of Canada [20], [24]. In this system, weather parameters obtained from *Environment Canada* stations were employed to create, twice a week, risk maps of SSR development. These maps were employed by Canadian farmers, but they are no longer available [20]. On the other hand, similar

risk maps based on temperature and precipitation patterns are still available online to farmers of North Dakota [31]. The main limitation of these systems is that they only indicate the regional risk of an outbreak, ignoring characteristics of specific-field microclimates [20]. Furthermore, they are based exclusively on weather parameters, without the inclusion of any measurement of inoculum levels.

1.4.3   Forecast based on presence and level of disease inoculum

The measurement of inoculum levels present in the field is an important factor influencing the accuracy of forecasting systems, as it indicates the amount of pathogen available for SSR development. Inoculum levels can be measured in numerous ways, including counting the number of apothecia and/or sclerotia [2], measuring the concentration of ascospores [18], [21], [29], [32] as well as petal infestation measurements [30], [33], [34].

Counting the number of apothecia and/or sclerotia accounts only for inoculum present in the field, which might not provide an efficient forecasting system, as SSR has been reported in fields with no apothecia [18], [35], [36]. On the other hand, the estimation of airborne inoculum through petal infestation measurements or by monitoring the concentration of ascospores using spore-trap samplers may provide a more accurate and field-specific indication of SSR risk.

Petal infestation is commonly measured by collecting canola petals from the field, which are then cultured in Petri dishes containing potato dextrose agar (PDA). The Petri dishes are incubated for 3-5 days, after which the percentage of petals infested with *S. sclerotiorum* is visually determined by colony morphology [33]. The percentage of infested petals is then correlated to the risk of disease development, information that growers use to decide on whether fungicide application is required or not [33], [34]. When environmental data was included, the petal test has shown good assessment risk [37]. Molecular methods such as real-time PCR can also be employed

8

to measure petal infestation [38]–[40]. In Canada, petal-test kits following this protocol are commercially available.

The major limitation of the petal test based on PDA plating is the long incubation time (3-5 days), during which the disease can spread throughout the crop causing significant economic losses. Moreover, it is labor-intensive and requires skilled personnel to correctly identify *S. sclerotiorum* colonies. Petal infestation measurements with PCR analysis can reduce the time delay associated with the incubation time of the agar test as well as potential errors associated with the wrong identification of *S. sclerotiorum* colonies [39]. However, farmers still need to ship their samples to a testing laboratory, which can take some time and thus delay their spray decision. Measurements obtained with PCR are robust, highly reproducible and have excellent selectivity and sensitivity, but can be inhibited by sample matrices [41], requiring sample pre-treatment before PCR. This, together with their elevated cost and complexity, makes them unsuitable for on-site applications.

Spore-trap samplers have also been employed for the collection of in-field *S. sclerotiorum* airborne inoculum [29], [32], [42]. Up until recently, spore-traps were mainly restricted to research applications. However, since 2018, a passive spore-trap sampler, marketed as *Spornado Sampler* has been commercially available in Canada. The samplers are placed in the field to directly collect ascospores from the air in "sample cassettes". Farmers can then send these cassettes to laboratories for PCR analysis. After the analysis, farmers receive information about the risk level (low, medium, or high) of disease development, so that they can take better spray decisions.

Here is important to explain what "spore-trap samplers" are. Although this might be a well-known tool for those with a background in agriculture, it might not be clear for most of the readers with a background in engineering. Spore-trap samplers are commercially available tools or

instruments that are employed to collect (or sample) particles present in the air employing a vacuum pump (active spore-trap samplers) or without a vacuum pump (passive spore-trap samplers). Depending on the brand and model, trapped particles can be collected in vessels containing a liquid media or culture media. Chapter 5 presents images of a spore-trap sampler.

1.4.4   Forecast employing micromachined devices

Advances in microfabrication technologies and microfluidic platforms have allowed the development of lab-on-a-chip systems that can alleviate some of the drawbacks presented by conventional methods bound exclusively to research laboratories, such as PCR, and flow cytometry. The demand for a low-cost, miniaturized, field-specific and on-site SSR forecasting system may be met with the increasing progress of lab-on-a-chip platforms. Although there have been several reports of micromachined devices used for plant pathogen diagnosis [43]–[47], approaches aiming at the detection and quantization of SSR airborne inoculum have been limited to one [21]. In a collaboration between InnoTech Alberta and our research group at the University of Alberta (Binary Lab), the first immuno-impedimetric biosensor for ascospore detection was developed [21]. *S. sclerotiorum* ascospores were detected employing an impedimetric non-faradaic biosensor coated with anti-S. *sclerotiorum* polyclonal antibodies as the biorecognition element. Antibodies were employed to bind ascospores to the surface of interdigitated electrodes and thus generate a detectable electrical signal. Figure 1.2 shows the developed biosensor. Ascospores in solution were successfully detected with this device, but the limit of detection reported as 7.8×10^4 ascospores/mL, was far from the threshold that is required for SSR forecasting applications. A reliable system for the forecasting of SSR must be able to detect a threshold of about 10 ascospores/m^3 of air to provide an early warning to farmers [42]. This threshold allows an 8-day advanced forecasting of SSR outbreaks. As seen in Figure 1.2, the biosensor was based on a design

containing a PDMS mask with 8 wells, that need to be loaded and unloaded manually. The microdevices developed in this thesis, and described in more detail in the following chapters, have their foundations in the biosensor's early work.
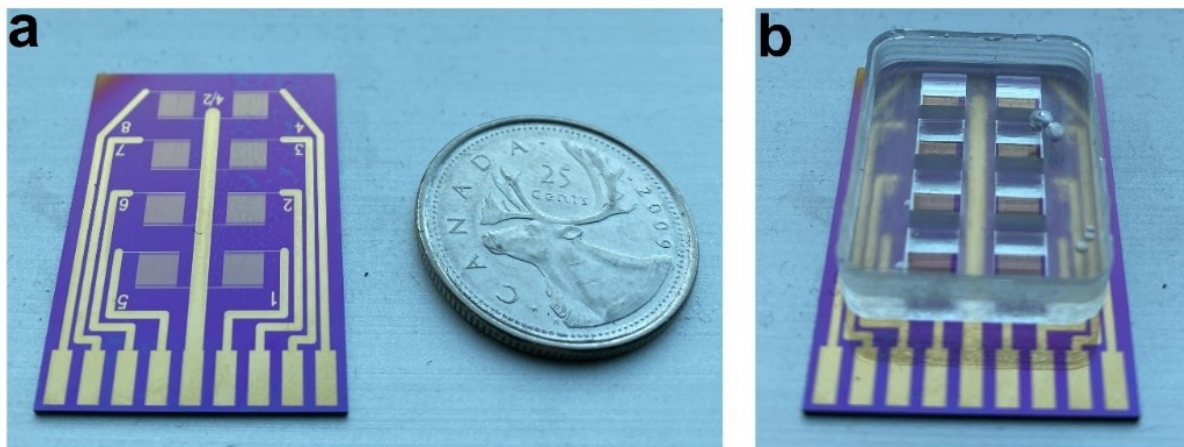
Figure 1.2: First biosensor for *S. sclerotiorum* ascospore quantification. (a) Biosensor showing gold microelectrodes for impedimetric detection. (b) Biosensor with PDMS mask for ascospores loading.

1.4.5   Microdevices employed for plant pathogen detection

As mentioned in the previous section, there have been several reports of micromachined devices used for plant pathogen detection, other than *S. sclerotiorum* [43]–[47]. Typically, methods employed by these portable devices are classified into direct and indirect techniques [46]. Direct methods are those that can detect the pathogen itself while indirect methods can detect the effects on the plant in response to the pathogen. Immunological approaches based on antigen-antibody binding reactions and molecular techniques using nucleic acid sequences of target pathogens comprise the direct methods. Recent reports include a microfluidic device that incorporates an electrochemical immunosensor for the detection of *Xanthomonas arboricola,* a disease that affects hazelnuts and walnut [48], and an impedimetric immunosensor fabricated with

gold microelectrodes for the detection of Plum Pox Virus, a disease that affects stone fruits [44]. Similarly, Cebula *et. al.* demonstrated the detection of the pathogen *Pseudomonas Syringae pv. Lachrymans,* the causative agent of cucumber angular leaf spot, by immobilizing antibodies on gold electrodes and employing impedimetric sensing as the transduction mechanism [49]. Within molecular methods, a foldable LAMP (Loop-mediated isothermal amplification) device was recently reported for the detection of two pathogens of rice, *Magnaporthe oryzae* and *Sarocladium oryzae,* causative agents of rice blast and sheath rot, respectively [50]. Employing a similar approach, Natsuhara *et. al.* developed a PDMS-based microfluidic device for the detection of tomato yellow leaf curl virus using LAMP and fluorescence microscopy [51].

On the other hand, indirect methods are typically based on imaging and volatile organic compounds (VOC) detection. The VOC profile produced by plants changes in response to a pathogen, thus, it can be used as a non-invasive diagnostic method. Using a commercial e-nose (gas sensor), Zhang *et.al.* successfully classified wheat of different storage ages and different degrees of insect damage [52]. Similarly, Laothawornkitkul *et. al.* employed an e-nose to discriminate VOC profiles of cucumber and pepper leaves under mechanical damage and pest attacks compared to healthy leaves [53].

Imaging techniques can include fluorescence spectroscopy and hyperspectral imaging [54]–[57]. The main idea of these techniques is that the response of plants to radiated light varies with the wavelength of the light, which can change in response to a pathogen. Recently, and employing hyperspectral imaging, Kong *et. al.* developed an application for detecting SSR symptoms in canola stems covering the spectral range of 384 - 1034 nm [58]. Although this approach can help identify SSR symptoms, it is not suitable to provide an early warning of SSR infection, which is in general a challenge associated with indirect methods [46].

1.5 Thesis outline

This thesis presents work done for the development of lab-on-a-chips devices for the label-free detection of *S. sclerotiorum* ascospores, aiming at their future integration with spore-trap samplers. This thesis intents to lie the foundations for the development of an SSR forecasting system based on micromachined devices. The work described here is organized into five chapters.

Chapter 1 introduces SSR, the literature review as well as the thesis objectives. Chapter 2 describes the first generation of devices that were developed based on the Coulter principle and dielectrophoretic force. The theory of the fundamentals of particle manipulation using dielectrophoresis is also described in chapter 2. Chapter 3 discusses the development of the second generation of devices based on an electroactive microwell array design. Chapter 4 describes the dielectric characterization of *S. sclerotiorum* ascospores and their relevance to the development of dielectrophoretic filters. Chapter 5 summarizes the work presented in this thesis as well as future work.

Chapter 2

A Coulter counter approach

2.1 Introduction

As previously noted, *S. sclerotiorum* ascospores were successfully detected with the devices based on an immuno-impedimetric approach [21]. However, those devices have deficiencies that could limit their potential integration with commercial spore-trap samplers into an effective SSR forecasting system. The main issue is related to the low sensitivity, where too many ascospores (7.8×10^4 ascospores/mL) are needed to generate a detectable signal. The second issue is related to the integration and automation of the device. The previous design has a PDMS mask with 8 wells that need to be loaded and unloaded manually, which makes automation and integration with commercial pumps difficult.

With these constraints in mind, a new device based on a microfluidic design was developed for the real-time detection of *S. sclerotiorum* ascospores, employing impedimetric sensing and dielectrophoresis.

The device measuring system is based on the Coulter principle, in which electrodes are submerged in an electrolyte solution, and changes in the impedance of the solution are monitored in a narrow fluidic constriction between the electrodes [59], [60]. When a microparticle such as a biological cell flows through the constriction, it will momentarily dislocate the solution's volume

14

in this region, producing a change in the measured impedance. Thus, for every passage event, impedance pulses proportional to the displaced volume of solution will be generated. These pulses can contain information about the size, number, speed, and type of the particles flowing through the constriction. This method was first developed by Walter Coulter [60], which laid the foundations of modern flow cytometers.

Advances in micro and nanofabrication have allowed the development of portable impedance-based flow cytometers, previously confined exclusively to benchtop equipment. First reports on micromachined impedance-based flow cytometers were published by Renaud et al.[61]–[63] using coplanar and parallel microelectrodes to extract cell information. Later on, approaches aiming to increase the sensitivity of these devices were also proposed, using insulating fluids [64], [65] and by shrinking channels to confine cells [66], [67]. More complex systems, which employ laser excitation and optical lenses, were also investigated by researchers [68], [69].

To selectively capture the target ascospores, a dielectrophoretic filter implemented through interdigitated microelectrodes (IME) was also integrated into our microfluidic device. Dielectrophoresis is an electrokinetic phenomenon widely employed for the selective manipulation of polarizable particles, such as bacterial and mammalian cells within a spatially non-uniform electric field [70]–[72].

The goal of our microfluidic device is to employ dielectrophoresis to selectively capture target ascospores that are injected into the microchannel of the device, while others in the sample are flushed away. Afterward, the target ascospores will be released into the flow stream of the microchannel and detected when flowing through channel constrictions employing dynamic impedimetric sensing based on the Coulter method. In the following sections, a detailed description

15

of the development (design, fabrication, and test) of these devices is presented, as well as a description of the theory of dielectrophoresis.

2.2 Fundamentals of Dielectrophoresis for Particle Manipulation

Dielectrophoresis (DEP) is the force exerted on a polarizable particle that arises from the interaction between a non-uniform electric field and the particle's induced dipole. As such, the DEP force strongly depends on the dielectric properties (electrical permittivity and conductivity) of the particle and surrounding medium [73], [74]. Unlike electrophoresis (EP), particles are not required to be charged for DEP manipulation. Figure 2.1 illustrates the difference between EP and DEP.
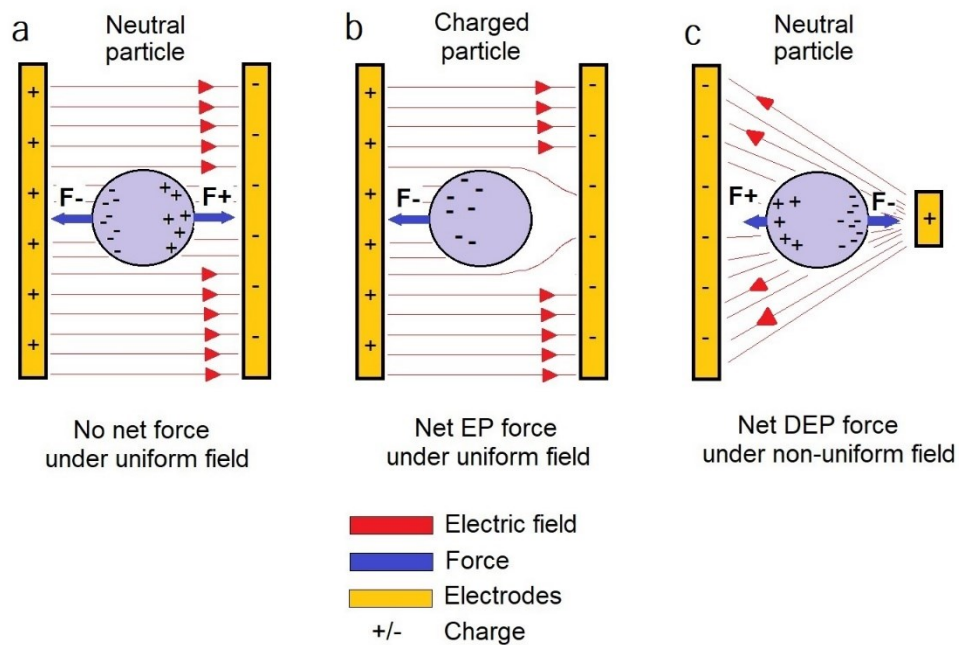
Figure 2.1. Difference between electrophoretic and dielectrophoretic forces. (a) Under a uniform electric field, the net force acting on a neutral and polarizable particle is zero as forces cancelled out. (b) EP force is exerted on a charged particle under a uniform electric field. (c) A net DEP

16

force acts on a neutral and polarizable particle under a non-uniform electric field (F- > F+) and the particle moves toward the positively charged electrode.

DEP was first described by Herbert Pohl [70], [72] and since then, it has been extensively used for the spatial manipulation of particles like cells and even DNA [75]. Besides being an efficient label-free particle manipulating technique, DEP's main advantage is that it can be easily integrated into lab-on-chip devices, which is linked to the ease of manufacturing electrodes that are required for the generation of electric fields at the microscale.

The general form of the DEP force $\boldsymbol{F}_{\text{DEP}}$ acting on an infinitesimal dipole is given by,

$$\boldsymbol{F}_{DEP} = \boldsymbol{p} \cdot \nabla \boldsymbol{E} \tag{2.1}$$

where $\boldsymbol{p}$ is the dipole moment and $\boldsymbol{E}$ is the external electric field. From this equation, it is clear that the electric field must be non-uniform in order to induce a net DEP force. The force on equation (2.1) is an approximation for the force induced on any physical (finite) dipole. Thus, to obtain the expression of a practical force acting on polarizable particles like cells or plastic beads, the effective dipole moment $\boldsymbol{p}_{eff}$ that is induced in these particles (by the external electric field) need to be determined and replace in equation (2.1). The effective dipole moment of a polarizable particle is, by definition, the moment of an equivalent point dipole that, when placed at the same location as the center of the particle, generates the same electric potential [76]. The electric potential Φ_{dipole} due to a point dipole of moment $\boldsymbol{p}$, at a distance $r = |\boldsymbol{r}|$ from the center of the dipole is given by:

$$\Phi_{dipole} = \frac{pcos\theta}{4\pi\varepsilon_m r^2} \tag{2.2}$$

where ε_m is the electric permittivity of the medium in which the dipole is immersed and θ is the angle between $\boldsymbol{r}$ and the dipole's axial direction. Therefore, the effective dipole moment $\boldsymbol{p_{eff}}$ of a dielectric particle can be determined by solving the boundary value problem and then comparing equation (2.2) to the potential of the particle due to the induced dipole [76].

If we consider the ideal case of an insulating sphere of radius R and permittivity ε_p in the presence of an electric field $\boldsymbol{E}$, and that is placed in a medium of permittivity ε_m, then the effective dipole moment is given by [76], [77]:

$$\boldsymbol{p_{eff}} = 4\pi\varepsilon_m R^3 \left\{ \frac{(\varepsilon_p - \varepsilon_m)}{(\varepsilon_p + 2\varepsilon_m)} \right\} \boldsymbol{E} \qquad (2.3)$$

By replacing $\boldsymbol{p_{eff}}$ into equation (2.1), and provided that the particle is small compared to the non-uniformities of the field, the DEP force acting on the sphere is:

$$\boldsymbol{F_{DEP}} = 2\pi\varepsilon_m R^3 \left\{ \frac{(\varepsilon_p - \varepsilon_m)}{(\varepsilon_p + 2\varepsilon_m)} \right\} \nabla|\boldsymbol{E}|^2 \qquad (2.4)$$

where the bracketed fractional term is known as the Clausius-Mossotti (CM) factor, which gives a measure of the strength of the effective polarization as a function of the permittivities [76], [77]. If $\varepsilon_p > \varepsilon_m$ the CM factor is positive, and the DEP force is directed towards regions of maximum electric field gradient, known as positive DEP or pDEP. If $\varepsilon_p < \varepsilon_m$ the CM factor is negative and the DEP force is directed towards regions of minimum electric field gradient, known as negative DEP or nDEP.

The DEP force from equation (2.4) is the induced force on a perfect insulator. In reality, particles and mediums have finite conductivities. Therefore, we can find a more realistic expression for the DEP force by considering a sphere of permittivity ε_p and electrical conductivity

18

σ_p, placed in a medium of permittivity ε_m with a conductivity of σ_m. Considering a sinusoidal electric field $\boldsymbol{E}(\boldsymbol{r}, t) = \mathrm{Re}(\boldsymbol{E_o}(\boldsymbol{r})e^{j\omega t})$, the effective dipole moment of the particle will be given by [76], [77]:

$$\boldsymbol{p_{eff}} = 4\pi\varepsilon_m R^3 \mathrm{Re}\left\{\frac{\left(\varepsilon_p{}^* - \varepsilon_m{}^*\right)}{\left(\varepsilon_p{}^* + 2\varepsilon_m{}^*\right)}\right\} \cos(\omega t)\boldsymbol{E_o}(\boldsymbol{r}) \tag{2.5}$$

where $\varepsilon_p{}^*$ and $\varepsilon_m{}^*$ are the complex permittivity of the particle and medium, respectively, each given by $\varepsilon^* = \varepsilon + \sigma/j\omega$, where ω is the frequency of the applied electric field. Again, by replacing equation (2.5) into equation (2.1), the DEP force acting on the particle can be calculated as [76], [77]:

$$\boldsymbol{F}_{DEP}(\boldsymbol{r}) = 2\pi\varepsilon_m R^3 Re\left\{\frac{\left(\varepsilon_p{}^* - \varepsilon_m{}^*\right)}{\left(\varepsilon_p{}^* + 2\varepsilon_m{}^*\right)}\right\} \cos^2(\omega t)\nabla|\boldsymbol{E_o}(\boldsymbol{r})|^2 \tag{2.6}$$

By taking the time average, $cos^2(\omega t)$ it is simplified to ½, thus the time average DEP force acting on the particle is given by [76], [77]:

$$\langle\boldsymbol{F}_{DEP}(\boldsymbol{r})\rangle = \pi\varepsilon_m R^3 Re\left\{\frac{\left(\varepsilon_p{}^* - \varepsilon_m{}^*\right)}{\left(\varepsilon_p{}^* + 2\varepsilon_m{}^*\right)}\right\}\nabla|\boldsymbol{E_o}(\boldsymbol{r})|^2 \tag{2.7}$$

Equation (2.7) is the most common equation employed to describe the DEP force acting on particles such as biological cells, as it is more realistic than the force on eq. (2.4).

The direction of the DEP force is given by the sign of the real part of the CM factor, which is a frequency dependent function. Figure 2.2 shows an example of CM factor curves for red blood cells in saline solution of different conductivities. When the real part of the CM factor is positive, the particle will experience pDEP force, and when it is negative, the particle will experience nDEP force. These DEP responses depend on the applied frequency and the dielectric properties of the

particle and medium. Therefore, different species will have different DEP responses at different frequencies and is mainly this dependency that enables DEP filters to electrically separate different species of cells and other biological particles.
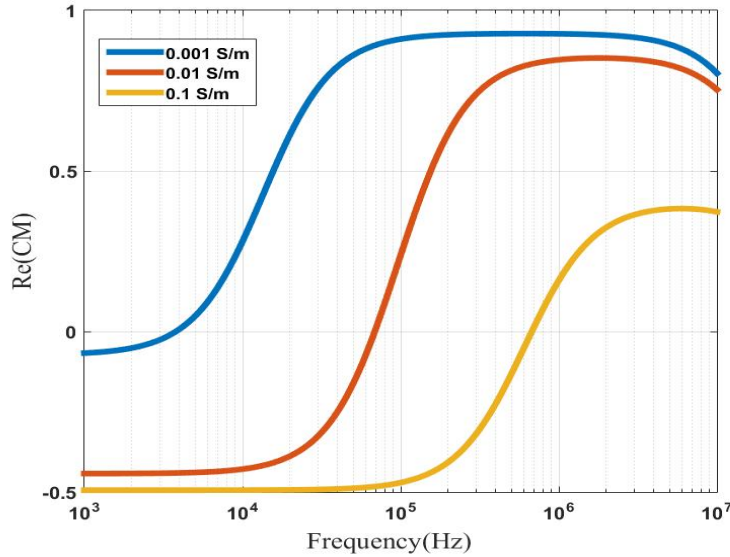
Figure 2.2. The real part of CM factor for red blood cells in saline solution of different conductivities. Curves were plotted using the dielectric properties reported in reference [78].

2.3 Materials and Methods

2.3.1 Design considerations

The design guidelines for the first generation of devices were mainly driven by the limitations encountered in the previously introduced biosensor [21]. To facilitate the integration with commercial pumps, a microfluidic approach was chosen. On the other hand, a Coulter counter with additional on-chip functionality implemented through a dielectrophoretic filter was chosen to increase the sensitivity and achieve single ascospore detection. Both structures (DEP filter and Coulter counters) were designed to be fabricated based on coplanar microelectrodes. Figure 2.3

shows the CAD design of a single microfluidic device[2]. The complete photolithography mask employed for the fabrication of devices is provided in Appendix A (Figure A. 1).
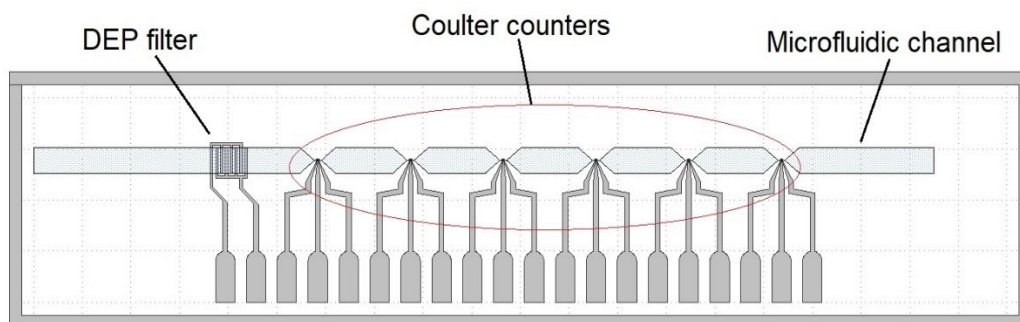
Figure 2.3. CAD design of a single die. The device is based on a microfluidic design that integrates a DEP filter and Coulter counters.

The sealing of our devices was initially designed to be done with polydimethylsiloxane (PDMS), a standard material used in microfluidics. However, Coulter counters are very prone to clogging issues due to small channel constrictions, roughly in the order of the largest particle to be detected [79]. In our devices, the constriction is in the order of 20 µm, and a clogged channel can considerably reduce the lifetime of the chip, especially when considering that the sealing of PDMS to glass substrates is irreversible. For this reason, the microchannels were designed to be fabricated with a negative photoresist and sealed using hydrophilic adhesive tape, providing a simple, re-usable, and straightforward sealing mechanism. Furthermore, this process does not require specialized training or equipment and allows for easy sterilization of channels for re-use, hence reducing the chip cost and increasing the yield per wafer.

2.3.2 Device fabrication

---

[2] The design of the microfluidic chip was based on a similar device employed by our collaborators at Yale University, led by Dr. Mark Reed. With their help, I adapted the design for my project. I designed the photolithography masks and fabricated all versions of the devices that are described in this thesis.

Microfluidic chips were fabricated using standard photolithography processes on borosilicate glass substrates of 4-inch diameter and 1 mm thickness.[3] Substrates were first cleaned with piranha solution (3:1, H_2SO_4/H_2O_2) for 15 min. Subsequently, aluminum was sputtered and patterned to form an interdigitated microelectrode (IME) structure for the DEP filter, consisting of 8 electrode fingers of 1mm length, 100 μm width, and 100 μm spacing. Six sets of coplanar microelectrode structures of 20 μm wide and 20 μm spacing were also patterned on the substrate for impedimetric detection. The aluminum electrodes were patterned using the positive photoresist (PR) HPR 504, which was spread at 500 rpm for 10 s, then increased to 4000 rpm for 40 s, and finally baked at 115 °C for 90 s. Metalized wafers coated with the PR were exposed under UV light at 200 mJ/cm^2 using a mask aligner (ABM-USA, Inc.) and developed using Microposit 354 developer for 30 s. After PR patterning, the metal was etched using aluminum etchant type A (Transene Company Inc.). The total thickness of the deposited aluminum was 210 nm. Aluminum was selected due to its low cost and ease of fabrication compared to gold. To fabricate the microfluidic channels, a second photomask was used after depositing 20 μm of the negative PR SU-8 2015 (Kayaku Advanced Materials Inc) on top of the patterned aluminum layer. SU-8 was spread on top of the substrates at 500 rpm for 15 s and then increased to 2000 rpm for 30 s to form a 20 μm thick layer. These substrates were soft baked at 65 °C for 2 min and then for 4 min at 95 °C. Subsequently, UV light exposure was done at 150 mJ/cm^2, followed by a post-exposure bake step at 65 °C for 2 min and then for 5 min at 95 °C. Finally, the substrates were developed for 2 min using SU-8 developer (Kayaku Advanced Materials Inc.). Channel constrictions of 20, 30, 40, 50, and 60 μm width and a constant depth of 20 μm were fabricated. Afterward, chips were cleaned with ethanol in an ultrasonic bath for 2 minutes and left to dry for 1 hour at room temperature. Finally,

---

[3] I would like to thank Dr. Gaser Abdelrasoul for always being open to discuss with me about fabrication processes.

hydrophilic and pressure-sensitive adhesive tape (Adhesive Research, ARflow 93049) was carefully applied on top of the surface, and then inlet/outlet holes were created to connect the chip to a syringe pump. The schematic representation of the fabrication process[4] is shown in Figure 2.4a and the fabricated chip is shown in Figure 2.4b. The IME structure and the microelectrodes located in the channel constrictions are highlighted in Figure 2.4c and 2.4d. Every chip is integrated with six sets of microelectrode structures (Figure 2.4b), allowing multiple measurements at the same time. In the experiments described here, only one of these microelectrode sets was used (Figure 2.4d).
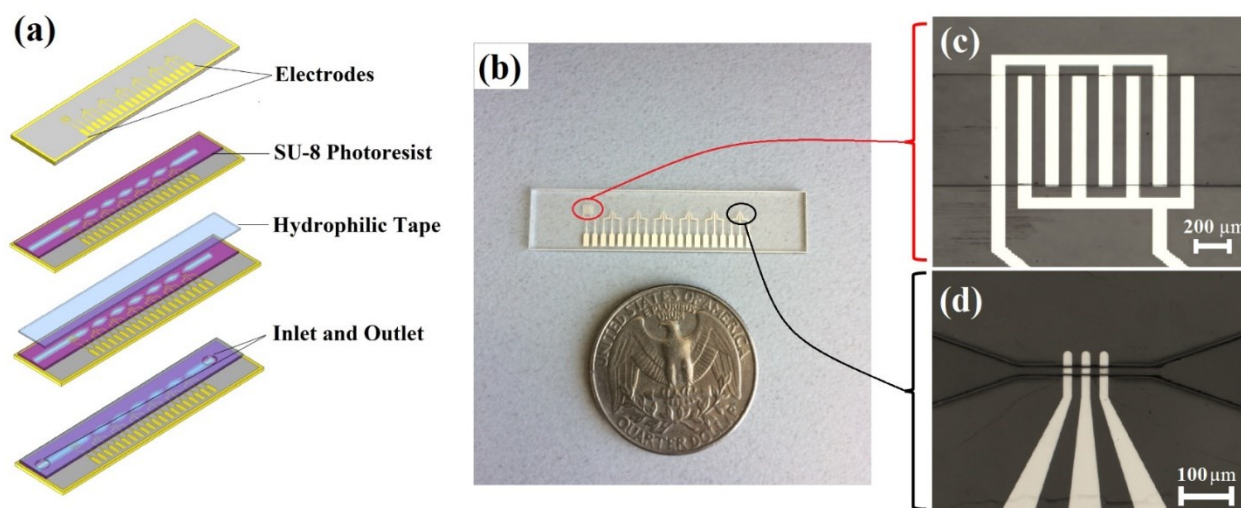
Figure 2.4. Microfluidic device for ascospore detection employing dielectrophoresis and impedimetric sensing: (a) Fabrication process; (b) Chip after fabrication; (c) Microscopic image of the IME structure with 8 electrode fingers of 1mm length, 100 μm width, and 100 μm spacing. The microfluidic channel width is 1mm, and the height is 20 μm; (d) Microscopic image of microelectrodes in channel constriction: dimensions of microelectrodes are 20 μm wide and 20 μm spacing. The channel constriction dimensions are 20 μm for both width and height with a length of 300 μm.

2.3.3 Equivalent circuit

The equivalent electrical circuit of the measuring system can be modeled as shown in Figure 2.5a, where Z_{ch-A} and Z_{ch-B} represent the channel impedance between the left-center and right-center electrodes, respectively. Z_{dl} is the double layer impedance generated at the electrode-electrolyte interface, and C_p is a parasitic capacitance in parallel with the channel impedance. A more simplified model is shown in Figure 2.5b, where the channel impedance is given by the solution resistance R_{sol} and the double layer impedance is assumed to be dominated by the double layer capacitance C_{dl}. It should be noted that this is a simplified model for a non-faradaic application (no-redox reaction), which is the case of Coulter counters. For this reason, factors such as charge transfer, non-uniform currents, and double-layer resistors were not considered, as they do not affect the interpretation of our results.
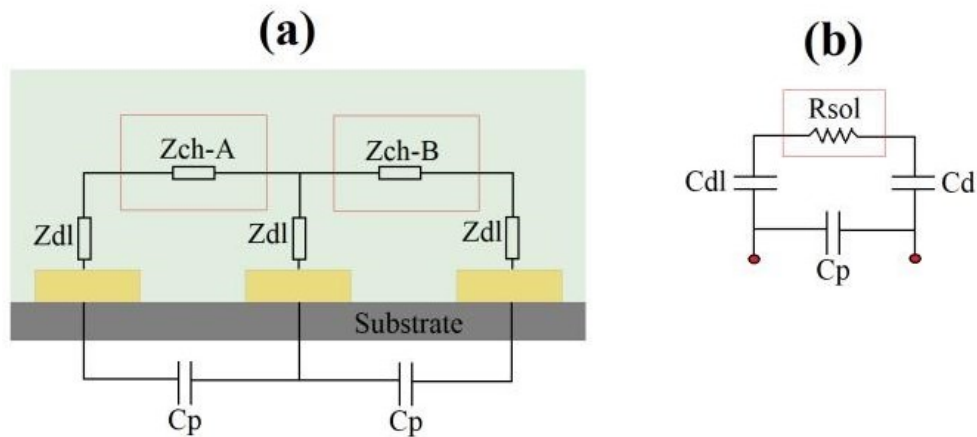
Figure 2.5: Equivalent circuit of the measuring system. (a) Basic electrical impedance model of the Coulter counter, Zch-A and Zch-B represent the channel impedance, Zdl is the double layer impedance and Cp is a parasitic capacitance; (b) Simplified electrical impedance model, Rsol is the solution resistance and Cdl is the double-layer capacitance.

The electrical double-layer is formed through the interaction of ions in the electrolyte solution and charge carriers at the surface of energized electrodes, and it is typically modeled as an ideal capacitor or a constant phase element [80], [81]. The impedance of the double layer is known to dominate the net impedance of an electrode-electrolyte system, such as the one employed in our device, at low frequencies. However, since the principle of Coulter counters relies on detecting changes in the impedance of the solution due to flowing particles, they are typically operated at frequencies where the double layer impedance is negligible. The impedance of the solution depends on the ionic concentration of the electrolyte and is typically modeled as a resistor. In this device, we employ phosphate-buffered saline (PBS) and dilutions of PBS with milli-Q water as the electrolyte. Finally, the parasitic impedance, which is modeled as a capacitor, is in parallel with the channel impedance and arises mainly from the cables employed to connect our device to measurement equipment, as well as from the substrate. The parasitic impedance dominates the systems' net impedance at very high frequencies because parallel impedances combine reciprocally, and thus the smaller term dominates. Parasitic effects are typically unavoidable, but they should be minimized to avoid significant attenuations of the output signal, even if the Coulter is not operated at very high frequencies.

Initially, our devices were fabricated on silicon wafers with 500 nm of thermally grown silicon dioxide as the insulator, as shown in Figure 2.6a. Initial tests with these devices showed a masking effect. Measuring the impedance spectrum between two electrodes of the Coulter, and with the microchannel filled with solutions of different conductivity, yielded no significant difference over a wide range of frequencies (Figure 2.6c). This issue was mainly attributed to

parasitic effects coming from the substrate, reason for which we decided to abandon the use of silicon dioxide wafers[5] and employ glass wafers instead (Figure 2.6b).
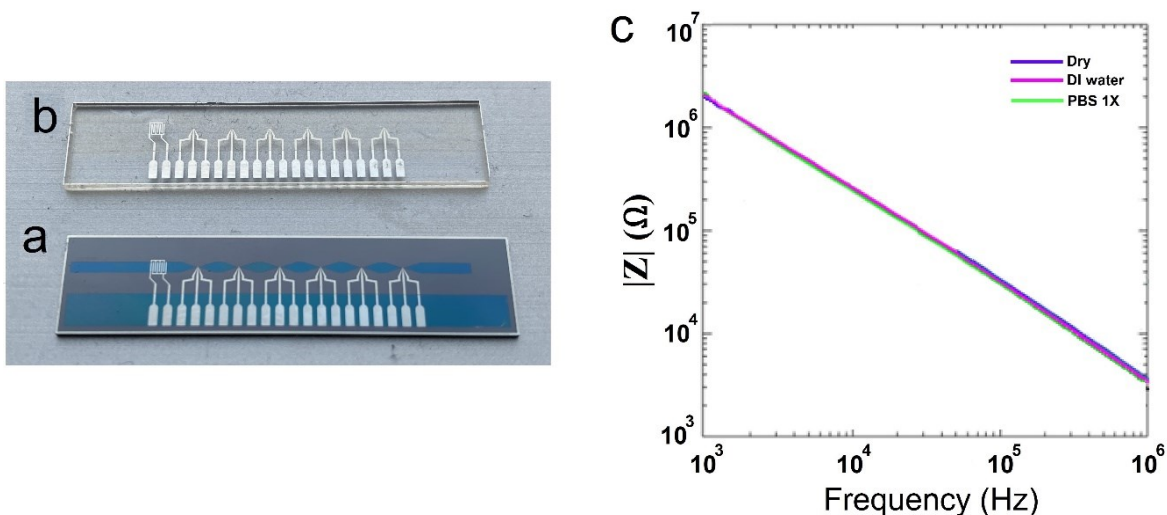
Figure 2.6: (a) Microfluidic device fabricated on silicon with 500 nm of thermally grown silicon dioxide. Devices based on silicon dioxide substrates were abandoned very early on in the project due to parasitic effects encountered during impedimetric measurements. (b) Microfluidic device fabricated on a glass substrate. (c) Initial impedance spectrum measurement of devices fabricated with silicon dioxide substrates. The microchannel was filled with solutions of different conductivities and no significant changes in the impedance were observed.

2.3.4 Methodology and instrumentation

To measure the channel impedance (Zch-A and Zch-B), a potentiostat SP-200 controlled by EC lab software from BioLogic Science Instruments Inc. (Knoxville, Tennessee) was employed. The chip was connected to the SP-200 through a custom chip-holder shown in Figure 2.7.[6]

---

[5] Silicon wafers with 500 nm of silicon dioxide were bought directly from the nanoFAB. A thicker oxide layer could reduce the parasitic effects, but it was easier and cheaper to change to glass substrates.
[6] I would like to thank Riley Stuermer for designing and fabricating the first version of the chip-holder as well as Lukas Menze, who fabricated the second version.
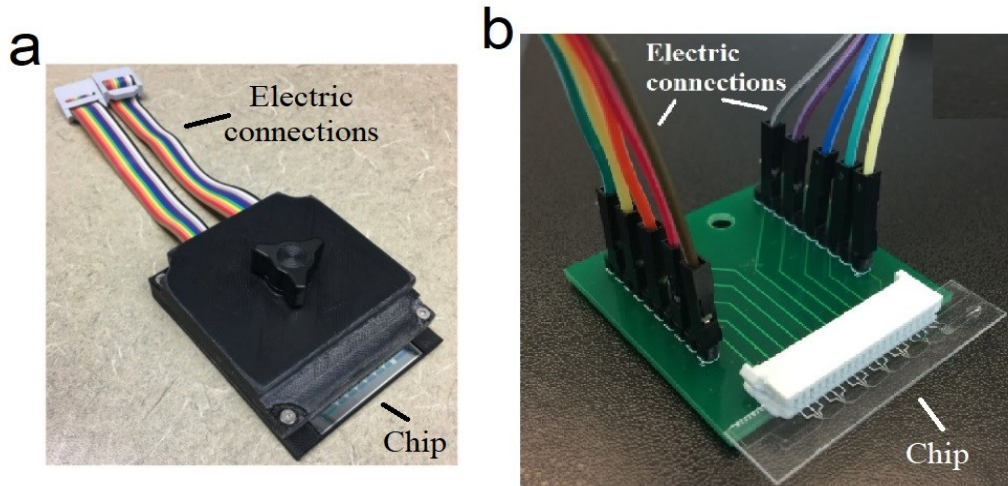
Figure 2.7: Chip-holders employed for connecting the microfluidic device to measurement equipment. (a) Holder based on spring-loaded pogo pins. Photograph courtesy of Riley Stuermer (b) Holder based on FFC connector.

The first version of the chip-holder, shown in Figure 2.7a, was based on a 3D printed piece made of polylactic acid (PLA) and integrated with spring-loaded pogo pins that contacted the pads of the chip. The second version, shown in Figure 2.7b, was based on a PCB integrated with an FFC connector. The first version of the holder was not employed for long, as it required constant soldering of cables to the spring-loaded pins. All the experiments described in this chapter were performed using the chip-holder with the FFC connector.

Fluid flow was achieved using a syringe pump (NE-1000, New Era Pump Systems Inc.) with plastic tubes (Tygon tubing) connected to inlet-outlet ports of the device. During all experiments, an upright fluorescence microscope (Amscope FM820TMF143) integrated with an ultra-sensitive 1.4MP monochrome CCD digital camera (Sony ICX825ALA) was used for imaging and video recording. The measured impedance data was recorded and processed with MATLAB (MathWorks, USA). The typical experimental setup is shown in Figure. 2.8.
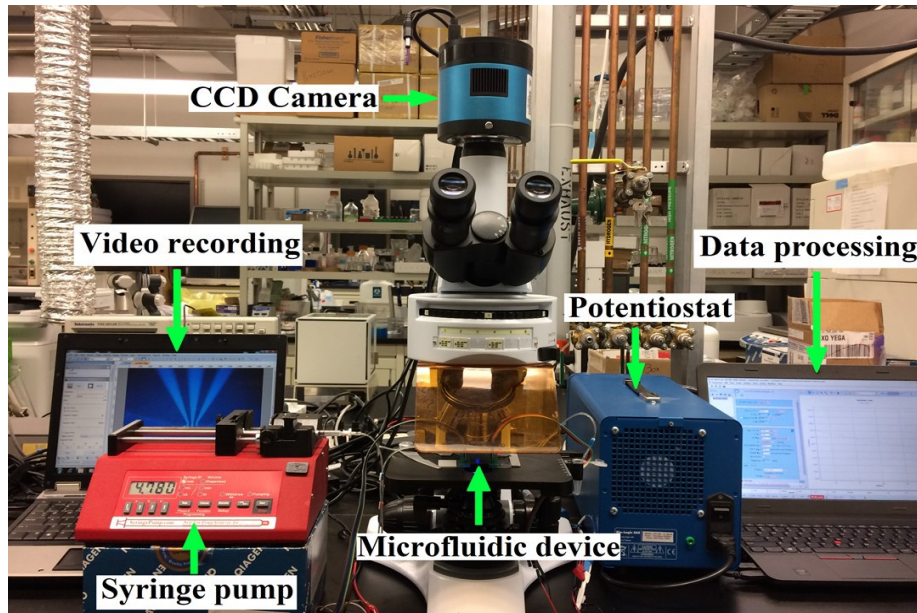
Figure 2.8: Experimental setup employed for experiments.

In order to validate the chip design, I performed initial experiments with fluorescent polystyrene beads (Spherotech) of 10 μm and 16 μm in diameter (nominal values). Chips with microfluidic constrictions of different sizes (width) were also fabricated and tested with polystyrene beads. Lastly, experiments with *S. sclerotiorum* ascospores were performed. For this, a heterogeneous spore sample containing *S. sclerotiorum* and *F. graminearum* was prepared. Before the impedimetric detection of target ascospores, they are selectively captured at the beginning of the microfluidic channel employing DEP, while contaminants in the sample are flushed away to the outlet drain. Subsequently, the DEP signal is turned off, allowing target ascospores to flow freely through the channels for subsequent detection. A function generator (Tektronix AFG 3251) was employed for the generation of the DEP signal. The time-stamps of impedance pulses that are generated by the passage of beads/ascospores through the constriction area were compared with video data to avoid false positives.

2.3.5 Spore production

S. sclerotiorum ascospores were obtained by planting sclerotia in wet sand and incubating them at 10 °C until they germinate to form apothecia.[7] Afterward, ascospores produced by apothecia were captured by directing them to filter paper discs using a vacuum pump. Ascospores can easily be released from the paper disk by vortexing it in any liquid solution. To facilitate identification and imaging, ascospores were stained using acridine orange (Thermo Fisher Scientific).

Fusarium graminearum[8] spores were also employed in our experiments to produce a heterogenous spore sample and were obtained by culturing the fungus in SNB (synthetic nutrient-poor broth) medium (KH_2PO_4 1 g, KNO_3 1 g, $MgSO_4 \cdot 7H_2O$ 0.5 g, KCl 0.5 g, glucose 0.2 g, sucrose 0.2 g / L) on a shaker (150 rpm) at room temperature for 7 days. The spores were separated by filtration of the liquid culture through a 20 μm filter and further centrifugation.

2.4   Experimental Results and Discussion

I first started by characterizing the impedance spectrum of the microelectrodes. Figure 2.9 presents the magnitude of the impedance over a wide range of frequencies between a pair of microelectrodes while the channel was filled with different concentrations of PBS. As expected, higher concentrations provide higher conductivity and thus lower impedance.

---

[7] *S. sclerotiorum* ascospores were produced by our collaborators at the research facilities of InnoTech in Vegreville.

[8] I would like to thank Dr. Oleksandra Savchenko for culturing *F. graminearum* spores. These were initially provided by our collaborators at InnoTech, but later on we started culturing them in our Lab as it is simpler to produce compared to *S. sclerotiorum* ascospores.
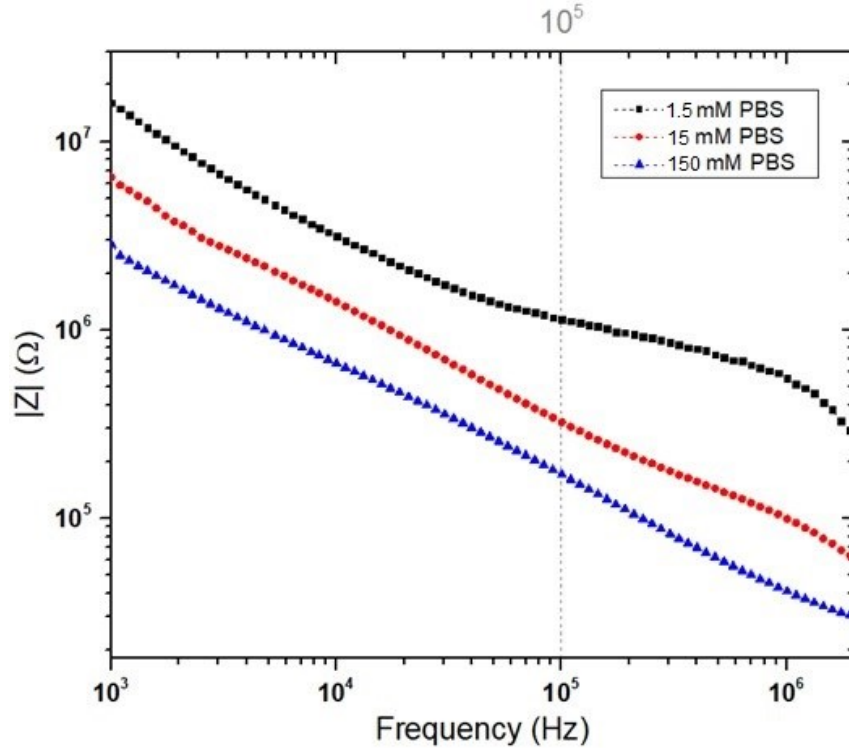
Figure 2.9. Impedance spectroscopy measurements ranging from 1 kHz to 2 MHz at different PBS concentrations. Symbols show the average value of five impedance measurements per frequency. The dashed vertical line indicates the frequency at which subsequent experiments are performed (100 kHz).

At 0.01X (1.5 mM) PBS, the impedance spectrum exhibits three distinct frequency ranges. Electrode polarization, attributed to the formation of ionic double layers around the microelectrodes dominates the impedance at low frequencies, while parasitic capacitances in the system cause the impedance to roll-off at higher frequencies. The middle frequency range reflects the resistance of the solution between the microelectrodes. To avoid masking effects due to the double layer and parasitic effects, real-time impedance measurements were performed at 100 kHz.

The chip was first tested with fluorescent polystyrene beads with diameters of 10 μm and 16 μm. Beads were diluted and mixed in a 1:1000 dilution of 0.01X PBS at pH 7.4. When the beads

flowed through the channel constriction area, peaks in the impedance were generated and measured with the SP-200. In order to avoid false positives due to noise and interference signals, video data was recorded simultaneously with the impedance measurement and employed to match every peak with the passing event of beads. Figure 2.10a illustrates an example of this process, while Figure 2.10b shows the average change in the impedance magnitude between a pair of microelectrodes obtained for 10 μm and 16 μm beads.
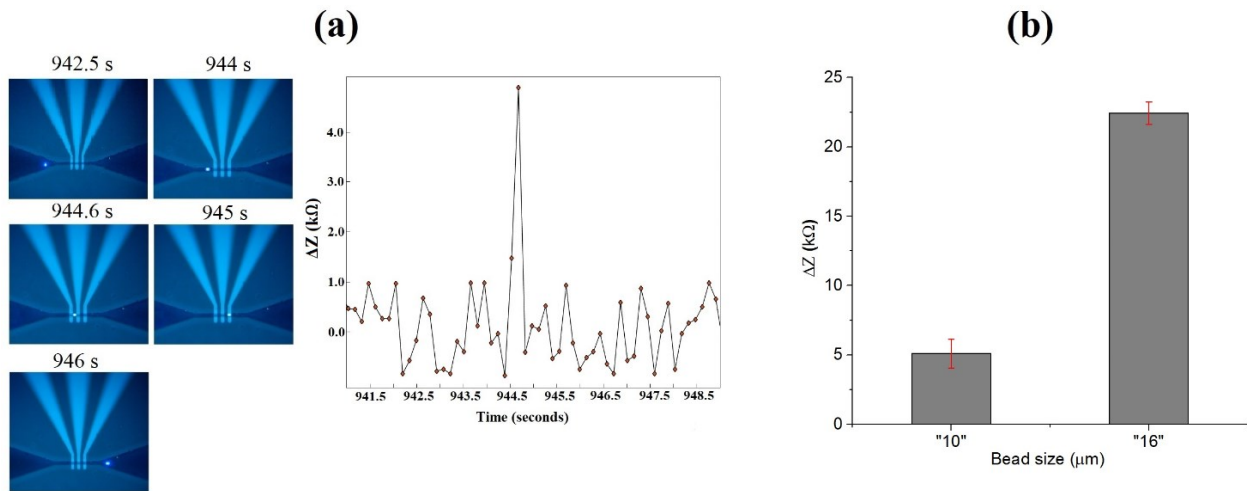
Figure 2.10: (a) Schematic representation of the measuring process: video data is recorded and matched with peaks in the impedance signal to avoid false positives; (b) Average change in the impedance for beads of 10 μm and 16 μm. Channel width and height are both 20 microns.

The applied flowrate in these experiments was 100 μL/h and the channel constriction size was 20 μm in width and height. In total, 52 beads of 10 μm and 46 beads of 16 μm were detected with an average peak of 5.10 ± 1.03 kΩ and 22.43 ± 0.81 kΩ, respectively. The volume ratio of beads assuming perfect spheres is 4.09, while the impedance change ratio when taking the mean of both signals is 4.40, which can be considered as a good approximation to validate the measuring system of our device.

31

The dispersion in peaks height can be explained by the height at which particles flow when passing through the detection area (microchannel constriction). When a voltage is applied to the microelectrodes, an electric field is generated, which decreases with the distance above the surface of the microelectrodes, therefore, particles flowing at different heights will have different contributions to the impedance. This vertical dependence of the impedance magnitude is a typical issue encountered in Coulter counters based on coplanar electrodes [82], [83].

Another factor that contributes to this wide dispersion is the variation in bead sizes. The manufacturer reported a coefficient of variation (CV) in size of 8% for particles of 10 μm and 7% for 16 μm beads. High-speed beads were not detected because the sampling rate of the SP-200 is around 200 μs, providing a maximum detectable speed of $1x10^5$ μm/s. Assuming a parabolic flow profile and that the average flow speed is two-thirds of the maximum speed, the maximum theoretical volumetric flowrate can be calculated to be 96 μL/h for a channel with a height and width of both 20 μm. Thus, to increase the detection rate, we set the pump to a flowrate of 50 μL/h.

To investigate how the channel constriction width affects the sensitivity, chips with 30, 40, 50, and 60 μm were also fabricated while keeping the height constant at 20 μm. Results showing the average change in impedance when beads of 10 μm are passing through the detection area are shown in Figure 2.11a.
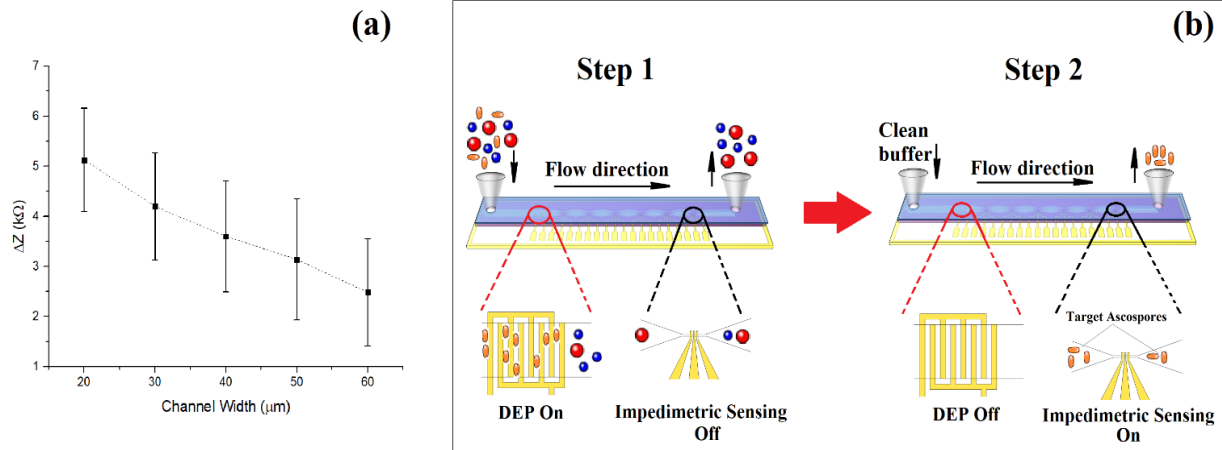
Figure 2.11. (a) Changes in the impedance at 100 kHz as a function of channel size (width), channel height is constant at 20 μm. Results were obtained with beads of 10 μm diameter, and the error bars represent the standard deviation; (b) Schematic representation of experiments performed with spores: In step 1 a mixed sample of spores is introduced into the chip, and target spores are subsequently selectively captured using DEP while contaminants are filtered out. In step 2, a PBS solution is introduced to the flow stream, the DEP signal is turned off, releasing target spores, and impedimetric sensing is turned on for the detection of target spores in real-time at 100 kHz.

The average values were calculated after 30 beads were detected per channel size, except for the channel of 20 μm where 52 beads were detected. As expected, changes in impedance, and therefore the sensitivity of the chip, decreases with the increase of channel width. Therefore, there is a trade-off between sensitivity and channel size, where small channels will provide a higher sensitivity at the expense of increasing the frequency of clogging. Since we aim to detect single ascospores of *S. sclerotiorum*, with ellipsoidal shape and size in the range of 2–5 μm × 8–15 μm, a chip with 20 μm width was selected.

After the validation experiments with beads, I continued with experiments to test the performance of the device for spore detection. In general, commercially available spore-trap samplers are not able to filter out all the debris and contaminants present in the field. Such

contaminants can be dust particles or other types of spores. Since our device is intended to be integrated with these tools, a filtering process is required to remove these particles before the impedimetric detection of target particles. Therefore, we employed a two-step process using a DEP filter before the impedimetric detection of *S. sclerotiorum* ascospores, as described schematically in Figure 2.11b.

First, a heterogeneous sample containing *S. sclerotiorum* and *F. graminearum* was prepared. We chose *F. graminearum* because it is one common type of spore present in the prairie regions of Canada, in which the majority of canola fields are located [84]. *F. graminearum* is also a pathogen for crops, especially wheat, causing the disease known as Fusarium head blight [84]. Both spores were first suspended separately in milli-Q water with a resistivity of 18.2 MΩ·cm^{-1} and at concentrations of about 7.8×10^3 spores/mL, measured using a standard hemocytometer, and then both samples were mixed in a final sample volume of 10 μL.

The mixed sample was then introduced through the chip's inlet at a flowrate of 50 μL/h. Subsequently, an AC excitation signal of 18 Vpp (peak to peak) at 60 kHz was applied to the IME structure to concentrate *S. sclerotiorum* ascospores at the electrode edges using pDEP, while other particles could flow freely to the outlet drain. Figure 2.12 shows a microscopic image of the heterogeneous spore sample, as well as the process of DEP filtering over time. *F. graminearum* spores have a banana shape, with an average size of around 40 μm long and 2-4 um wide.

Here is important to mention that the frequency of the DEP signal was determined empirically, by observing the motion of spores between 1 kHz and 10 MHz and under the same buffer solution. Ideally, the DEP response of the spores should be obtained by plotting the curves of the CM factor, as we showed in Figure 2.2, however, the dielectric properties of *S. sclerotiorum*

ascospores are unknown. Table 2.1 summarizes the DEP responses of *S. sclerotiorum* ascospores that were obtained by observing their motion between 1 kHz and 10 MHz.
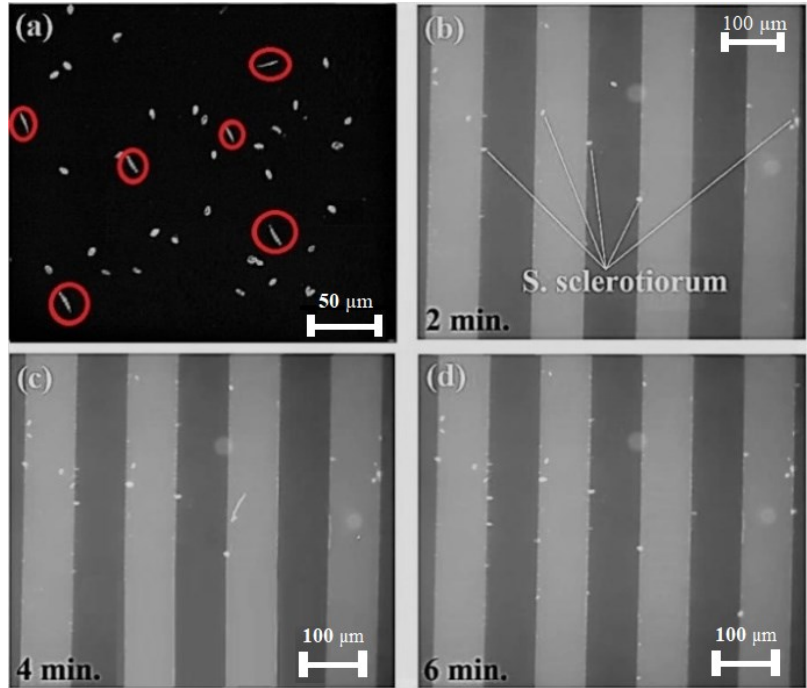
Figure 2.12: DEP filter: (a) Heterogeneous sample of spores, *F. graminearum* spores are shown in red circles; (b) 2 min. of DEP signal on; (c) 4 min. of DEP signal on; (d) 6 min. of DEP signal on. Flow is from left to right. The applied voltage is 18 Vpp. The longer the DEP signal is turned on, the more *S. sclerotiorum* ascospores accumulate at the electrode edges.

Frequency	Observed DEP response
1 kHz	Unstable
10 kHz	pDEP
100 kHz	pDEP
1 MHz	pDEP
10 MHz	pDEP

Table 2.1: Observed DEP responses of *S. sclerotiorum* ascospores in milli-Q water as the medium solution.

Under 10 kHz, the DEP response was difficult to determine. Initially, I observed a few ascospores to be trapped at the edges of the IME, but they were often released after a few seconds, even without turning the DEP signal off and with very low flow rates. From 10 kHz and above, a stable pDEP response was observed. With the obtained DEP responses and for the specific solution in which spores were suspended, 60 kHz at 18 Vpp and with a flowrate of 50 µL/h provided a selective capture of target spores while others were flushed away. We employed Milli-Q water due to its large resistivity and to minimize Joule heating. The capture efficiency was found to be close to 87% for a flowrate of 50 µL/h. This was calculated by comparing the input and output concentration of target spores during the first step.

Once all the contaminants were filtered out, a 0.01X PBS solution was introduced to the flow stream of the device, the DEP signal was turned off, and changes in the impedance magnitude were measured. Figure 2.13a shows the exact moment in which an *S. sclerotiorum* ascospore is passing through the microfluidic constriction while Figure 2.13b shows peaks in the impedance signal generated by a single ascospore and by a cluster of them.
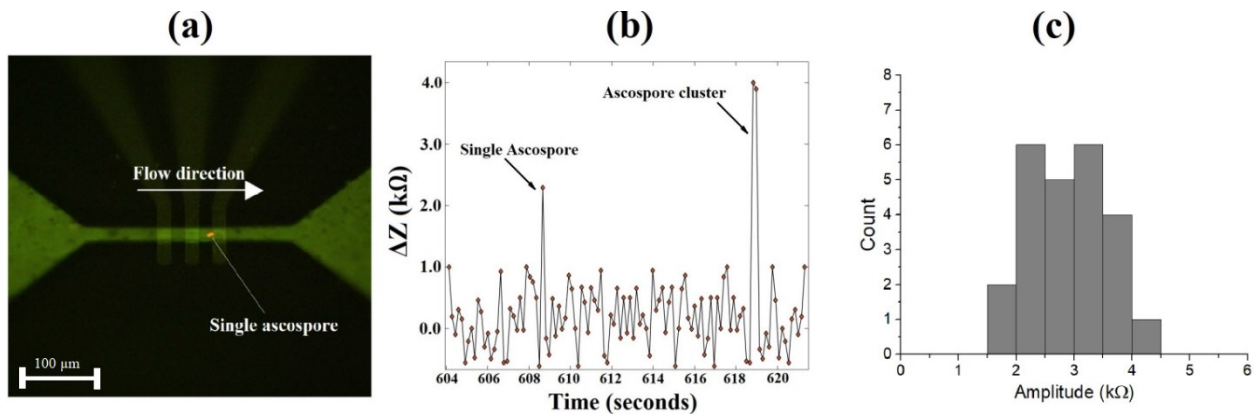
Figure 2.13: *S. sclerotiorum* detection: (a) Single *S. sclerotiorum* ascospore flowing in a 20 µm wide microfluidic constriction; (b) Real-time impedance measurement showing peaks produced by a single ascospore and an ascospore cluster. The impedance measurement was performed at

100 kHz; (c) Histogram of the impedance signal for single *S. sclerotiorum* ascospores. In total, 24 single ascospores were detected.

In total, 24 single ascospores were measured with an average impedance change of 3.00 ± 0.71 kΩ. The impedance histogram for ascospores is shown in Figure 2.13c. Although ascospores may have the same length as beads of 10 μm, their volume is smaller, which is why smaller changes were obtained. In these experiments, the average size of our ascospores was found to be 11 ± 2 μm x 3 ± 1 μm, determined using an optical microscope.

The detection of ascospores was more challenging than the detection of beads since the detection signal peaks are closer to the background noise of our equipment (Figure 2.13b). The root-mean-square (RMS) value of the noise was measured to be 0.3378 kΩ. Figure 2.13c shows that the peak amplitudes of detected ascospores are larger than three times the RMS noise value. The CV of impedance measurements for ascospores is 23.5%, larger than the ones obtained for beads, with 20% and 4% for particles of 10 μm and 16 μm, respectively. Although sparse, ascospore aggregation was also present during our experiments, producing higher peaks (Figure 2.13b) than the average for single ascospores. Aggregated ascospores were identified with video data, and their peaks were not included and considered as false positives. Although they can still germinate and therefore infect plants, the goal of these experiments was to test, as a proof of concept, the sensitivity to single ascospores. The dispersion in peaks amplitude, as in the case of beads, can be explained by the height at which ascospores flow as well as the variability in ascospore size.

As mentioned before, changes in the impedance were monitored between two of the microelectrodes in the microfluidic constriction. A three-electrode configuration allows differential measurements and can provide antisymmetric peaks per detection event, which helps

to detect real signals from noise. By aiming to demonstrate the effectiveness and feasibility of our method, we only used two microelectrodes, as video data was employed to match every peak. The three microelectrodes in our chip were designed and intended for future field testing in which video recording wouldn't have been possible.

During initial experiments with beads and ascospores, channels were occasionally blocked, as shown in Figures 2.14a and b. This problem was quickly solved by peeling off the tape, cleaning the chip, and applying a new piece of tape, which would not be possible if commonly used materials, such as PDMS were employed to create the microfluidic channels. Figure 2.14c shows a chip that was re-taped and cleared of any clogs.
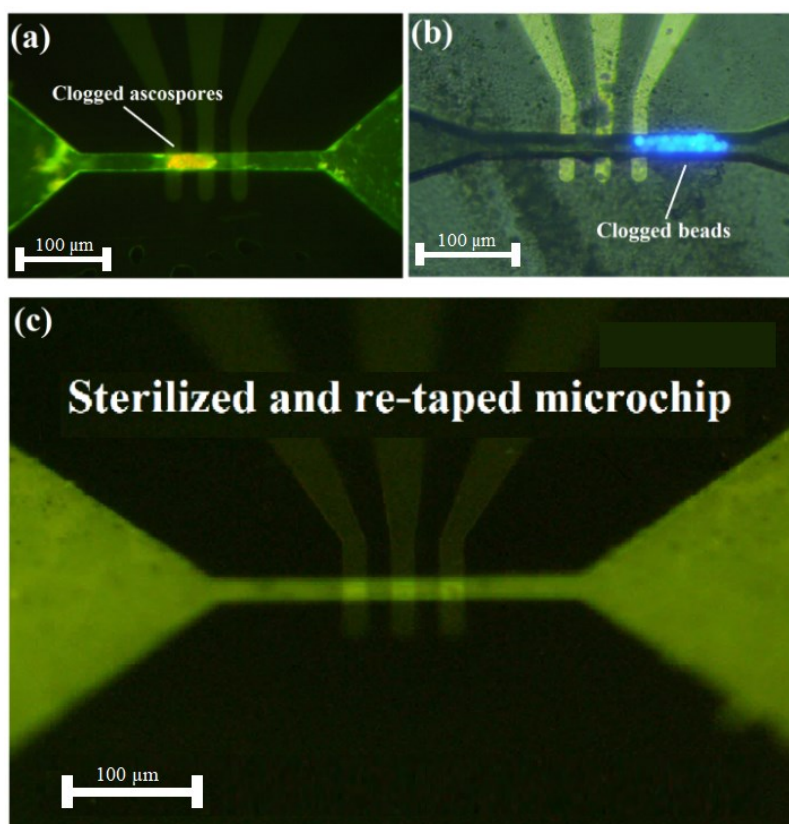
Figure 2.14: Microscopic images of clogged channels during initial experiments: (a) Ascospores blocking the channel constriction during an experiment; (b) Beads with 10 μm diameter blocking

the channel constriction during an experiment; (c) Sterilized and re-taped chip. Scale bars equal 100 μm.

Although in the previous approach [21], the same sensing mechanism based on impedance measurement was employed, the spore selectivity in our device is performed using DEP. DEP can filter out common contaminants present in samples provided by commercial spore-trap samplers, allowing single *S. sclerotiorum* ascospores (target spores) to be detected when they flow through the microfluidic constriction, thus satisfying the sensitivity requirements for an SSR early warning system. Furthermore, the footprint of the device was reduced by 50% compared to the previous design by incorporating a microfluidic platform that improves the device integration and compactness, facilitating its automation with commercial pumps. These features are essential when we think about designing a forecasting system consisting of a network of lab-on-a-chip platforms capable of monitoring large extensions of canola fields.

Commercial spore-trap samplers are capable of capturing airborne particles in a liquid collection media, such as the "*Biosampler*" by SKC Ltd. or "*Cyclone*" by Burkard Manufacturing Co Ltd. Thus, the concentration of particles captured by these samplers will depend on the number of particles present above the crop canopy, the sampler's collection volume, and the air passing through them. In the previous device, the minimum concentration required to produce a detectable signal was 7.8×10^4 ascospores/ mL, imposing this value as the minimum concentration of target ascospores that the traps should provide to the device. On the other hand, and based on the validation experiments presented here, our current microfluidic chip could provide no limitation on the concentration required from the traps, as single ascospores were detected.

2.5 Conclusions

In this chapter, we described the development of a proof of concept lab-on-a-chip device for the detection of *S. sclerotiorum* ascospores, aiming at smart-agriculture applications, and more specifically, canola crop protection. Our device is integrated with a dielectrophoretic filter, and an impedimetric measuring system based on the Coulter principle. Experimental results indicated an efficient dielectrophoretic separation between *S. sclerotiorum* ascospores and *F. graminearum* spores from a heterogenous sample. Furthermore, single *S. sclerotiorum* ascospores were detected using dynamic impedimetric sensing with a change in the impedance signal of around 0.3% per ascospore and using a benchtop potentiostat. To facilitate experimentation and reusability, a reversible and straightforward sealing mechanism using hydrophilic tape was implemented. To the best of our knowledge, the device we developed and described in this chapter represents the first report of single *S. sclerotiorum* ascospore detection employing a micromachined device.

Chapter 3

An Electroactive Microwell Array Design

3.1 Introduction

In this chapter, we describe the development of a new microfluidic device for the capture and quantification of *S. sclerotiorum* airborne inoculum. Although our previous device, described in Chapter 2, was able to successfully detect single ascospores, we identified a few aspects that could be improved when we consider the end goal of our devices. The sealing mechanism based on hydrophilic tape provided reusability of chips and a quick solution to clogging issues, which is certainly a useful feature during proof-of-concept experiments. However, a disposable device that can reduce the frequency of clogging and with permanently sealed channels is a more desirable feature, instead of having the final users (farmers) go through the cleaning and subsequent re-taping process. Another aspect that we seek to improve with the device we describe in this chapter is the sensitivity of impedance measurements. The Coulter counter uses dynamic impedance measurements, which require high-speed instruments to provide an output signal. On the other hand, static impedance measurements are known for providing higher sensitivity and can also reduce the large variability in the impedance signal due to the height at which ascospores flow in the microchannel. Here, is important to clarify that dynamic impedance measurement refers to cases in which the impedance signal changes rapidly over time, which was the case of our Coulter

device, producing impedance pulses due to ascospores that flow through the detection area. On the other hand, with static impedance measurements, we are referring to changes in the impedance due to ascospores that are static in the detection area of the device.

With these criteria in mind, we designed a microfluidic device based on an electrode-activated microwell array for the capture and quantification of *S. sclerotiorum* ascospores. Microwell arrays have been commonly used for high-throughput cell sequencing [85]–[89], cell pairing [90], [91] as well as for cancer cell identification and characterization [92]–[95]. These devices are normally designed with thousands of microwells and cells are generally detected and analyzed by imaging and microscopy. One common approach is to capture particles or cells into the microwells using gravity [88], [96]–[98]. To increase the capture efficiency, as well as to obtain selective capture, active trapping mechanisms, such as dielectrophoresis have been used [90], [99]–[102]. Recent reports of devices using microwell array and DEP include a microfluidic device composed of 3600 microwells for double-sub-Poisson single-cell RNA sequencing [85], an electroactive device with 300,000 microwells for the molecular analysis of tumor cells [94] and a microfluidic chip with more than 3000 microwells for the capture and subsequent analysis of cancer cells, including the characterization of cell apoptosis via immunostaining and fluorescent *in situ* hybridization (FISH) [92].

Here we developed an inexpensive and portable microfluidic device with a total of 190 picoliter wells, which were fabricated on top of coplanar nano-thick aluminum electrodes. These electrodes were employed for the dielectrophoresis-driven capture of *S. sclerotiorum* ascospores and subsequent on-chip detection using static impedimetric sensing. We extensively characterized our device and unambiguously demonstrated an ascospore trapping rate of more than 90%. The impedimetric quantification of single ascospores was also demonstrated, with a platform design

42

that allows us to address each column in the microwell array individually. The device presented here provides a unique approach for the capture and quantification of *S. sclerotiorum* airborne spores.

3.2 Materials and Methods

3.2.1 Design and operating principle

Our microfluidic device was designed and fabricated with a total of 20 aluminum microelectrodes (100 nm thick, 20 μm wide and 6 μm gap) and upon which an array of 190 microwells made of SU-8 resist was fabricated. Figure 3.1a shows the fabricated device while Figure 3.1b and 3.1c show a close-up of the microelectrodes and microwells, respectively.
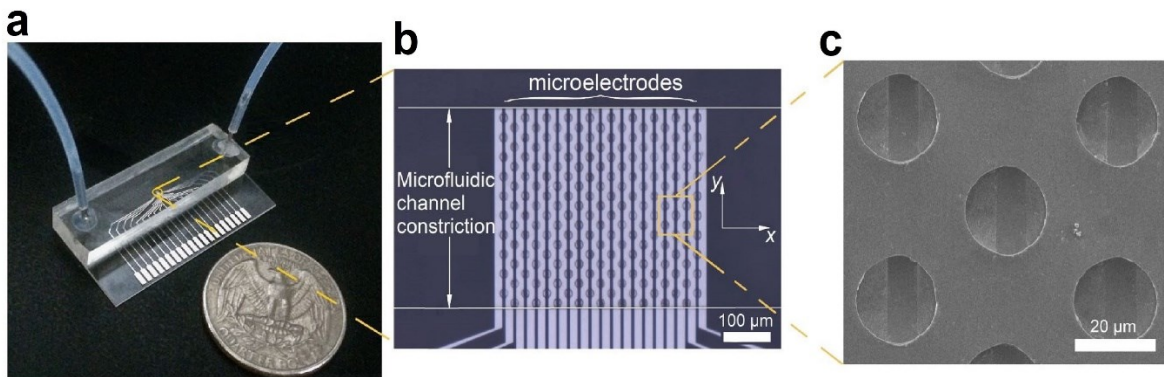
Figure 3.1: Microfluidic device based on an electroactive microwell array design. (a) Assembled microfluidic device. (b) Microscopic image of microelectrodes and microwells. The array has 190 microwells in total, 10 microwells per electrode pair (column) with 20 nano-thick aluminum electrodes in total. (c) Helium ion microscopy (HIM) image of microwells made of SU-8.

Each microelectrode can be addressed individually and between each pair, 10 microwells were placed. To focus the flow of ascospores towards the center of the device, in which the

microelectrodes were placed, the microfluidic channel was designed with a constriction, and each alternate column in the microwell array was shifted in the *y*-axis direction to ensure that a microwell is always under the path of a flowing ascospore (Figure 3.1b).

As mentioned in previous chapters, and according to previous reports [21], [42], the detection of approximately 10 ascospores/m^3 of air allows an 8-day advanced forecast of SSR outbreaks. This threshold expressed in, for example, ascospores per milliliters of solution will of course depend on the collecting volume of the air sampling system. In our device, we chose a low number of microwells based on this detection range. On the other hand, the diameter and depth of microwells were designed based on the average size of *S. sclerotiorum* ascospores. The schematic representation of the cross-sectional view of our device is shown in Figure 3.2a. The microfluidic channels in these devices are permanently sealed using PDMS (more details on fabrication aspects are given in the next section).

The operating principle to capture *S. sclerotiorum* ascospores into the microwells is based on the DEP-induced force. In the same manner as in the previous device, the non-uniform electric field for DEP capture is generated by applying a sinusoidal voltage to the microelectrodes, which can be configured as an interdigitated microelectrode (IME) structure during the process of trapping ascospores into the microwells. This configuration is schematically shown in Figure 3.2b. Once ascospores are captured, non-faradaic electrochemical impedance spectroscopy (nF-EIS) measurements can be performed to quantify ascospores column by column. nF-EIS is a label-free detection technique that measures the electrical current of an electrode-electrolyte system in response to an applied AC potential with no redox species in solution [103]–[105]. During the impedance measurements, microelectrodes can be operated individually, allowing the measurement of each column in the microwell array, and providing the ability to determine

ascospore occupancy per column. The configuration employed during impedance measurements is schematically shown in Figure 3.2c. The microelectrode configuration is externally controlled by switches in a custom-made chip-holder, shown in Figure 3.3.
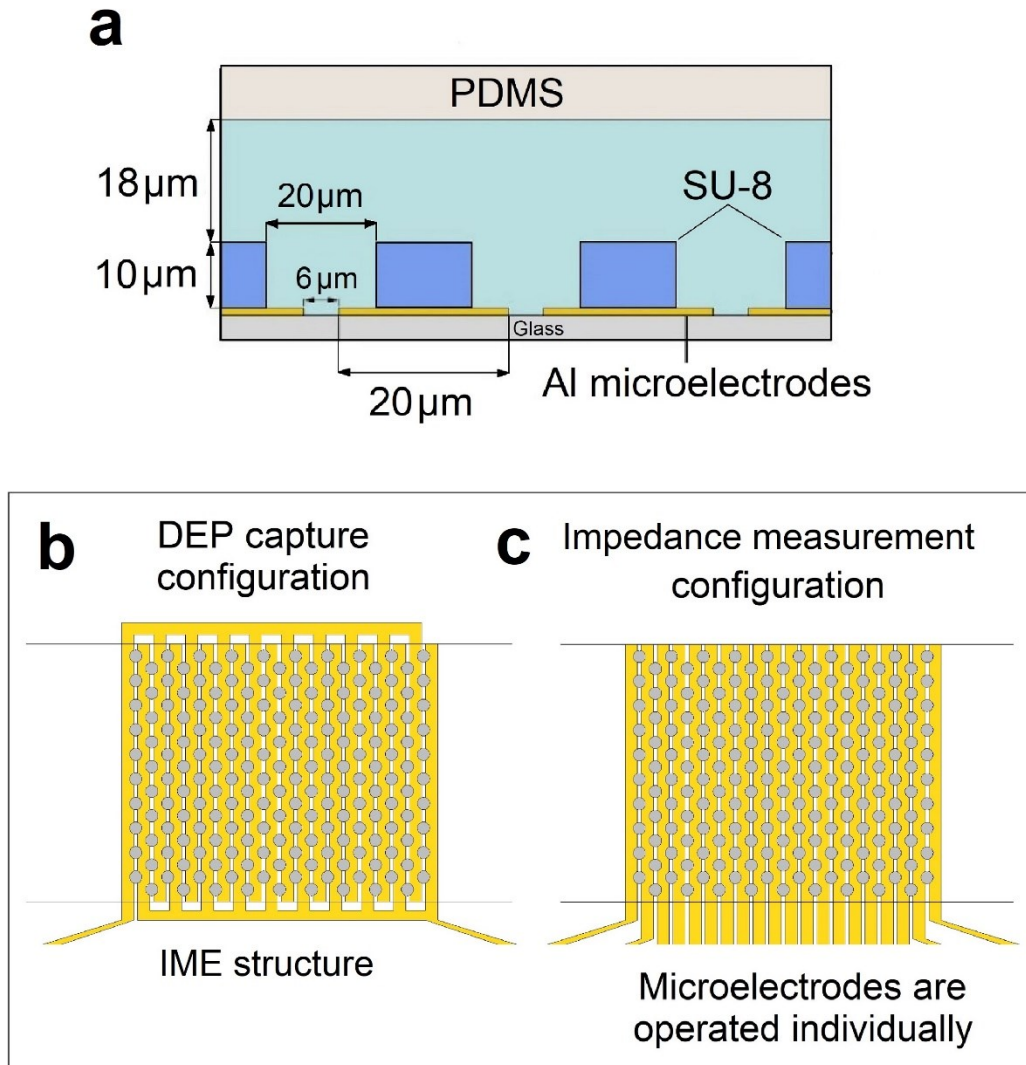
Figure 3.2: (a) Schematic representation of the cross-sectional view of the microfluidic device. (b) Microelectrodes can be combined into an interdigitated structure for ascospore capture in all the microwells of the device using DEP. (c) After DEP capture, microelectrodes are operated individually for impedance measurements column by column.
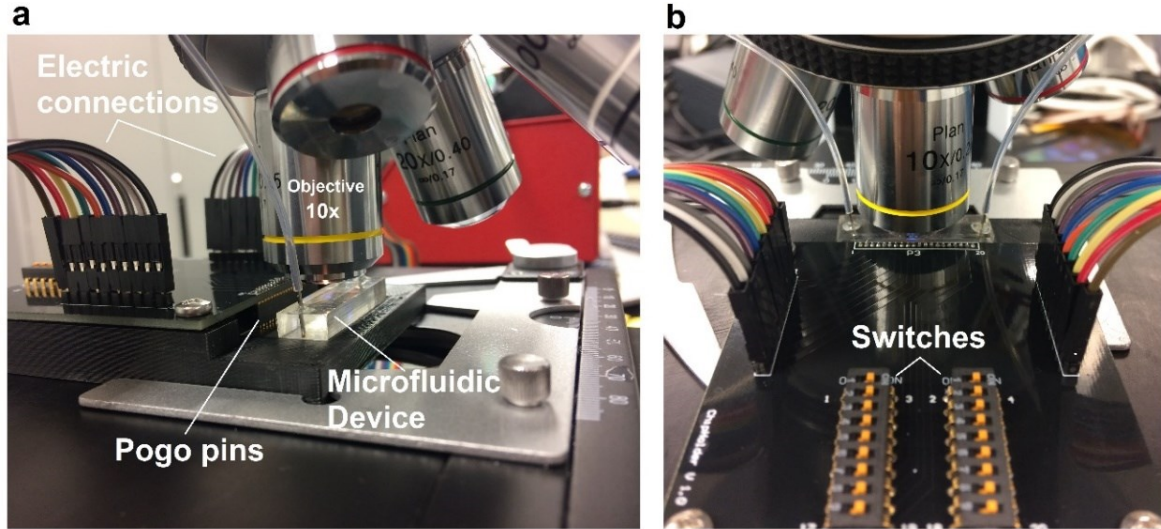
Figure 3.3: Custom-made chip holder. (a) Lateral view of the holder showing spring loaded pogo pins used to electrically connect the pads of the microfluidic device to external equipment. (b) Top view of chip holder showing the switches used to change the electrodes operation mode.

The final design of the microfluidic platform presented here, and shown in Figure 3.1a, was tailored based on a validation design that we first developed in our Lab.[9] Figure 3.4 shows the CAD design of a single die for the validation and final version of the microfluidic platform. The complete photolithography masks employed for the fabrication of both devices are provided in Appendix A (Figure A. 2 and A. 3).

The validation design helped us to develop a reliable fabrication protocol and allowed us to run initial tests. The main problems found with these devices were related to the alignment between the metal and SU-8 layers, as well as microwell distribution. These issues are shown in Figure 3.5. The misalignment of microwells to microelectrodes was due to insufficient alignment marks in the photomasks, which in turn enabled limited or no DEP capture when a signal was applied to the

---

[9] I would like to thank Lukas Menze for designing the validation photomask. I designed the final photomask, developed the fabrication process for both devices and performed tests of both devices.

microelectrodes, as these were covered by SU-8. The distribution of microwells was also problematic, as ascospores and other particles can flow through the channel constriction without even crossing any microwell, which also limited DEP capture.
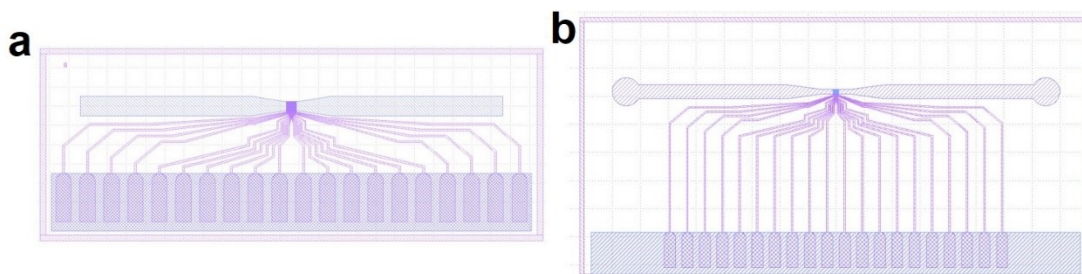
Figure 3.4: CAD files of a single die for (a) validation device developed for initial tests and fabrication process development. (b) The final version of our microfluidic platform design.
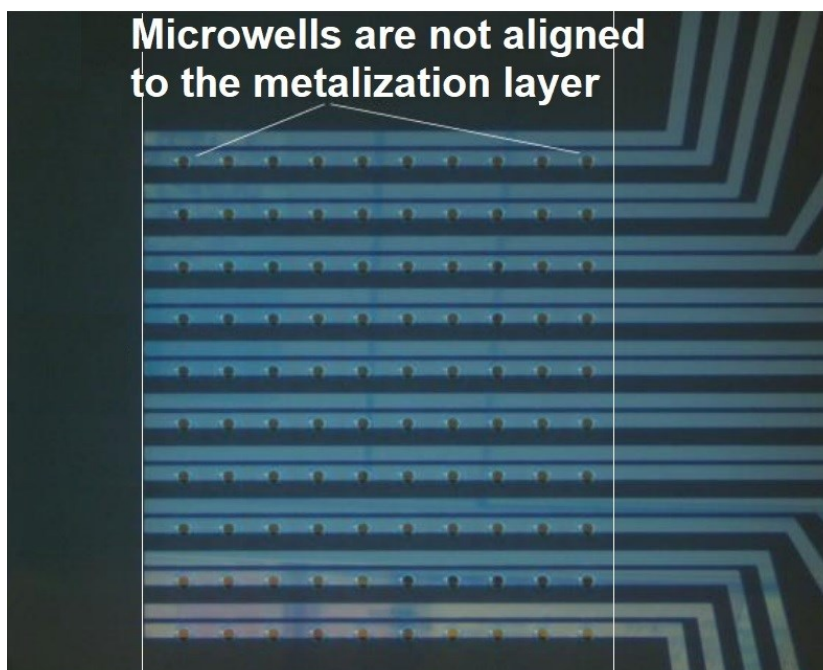
Figure 3.5: Microscopic image of microwells in the validation device. Microwells are not aligned to microelectrodes underneath and the distribution of wells is too scarce to obtain efficient DEP capture of particles.

3.2.2 Device fabrication

The microfluidic devices were fabricated on 500 µm thick glass substrates with 4-inch diameter. These substrates were first cleaned with piranha solution (3:1, H_2SO_4:H_2O_2) for 15 minutes. Immediately after this, 100 nm of aluminum was sputtered on top of the substrates. Electrodes were patterned using a positive photoresist AZ1512 (EMD Performance Materials Corp.), which was spread at 500 rpm for 10 s, then increased to 5000 rpm for 40 s, and finally baked at 100 °C for 60 s. Afterward, the photoresist was exposed under UV light at 100 mJ/cm^2 using a mask aligner (ABM-USA, Inc) and developed using AZ 400k 1:4 developer (EMD Performance Materials Corp.). The metal layer was subsequently etched using aluminum etchant type A (Transene Company Inc.). Electrodes were fabricated with a width of 20 µm and a gap between them of 6 µm. Using a second photomask, microwells were fabricated on top of the electrodes using the negative photoresist SU-8 (Kayaku Advanced Materials Inc.) with a thickness of 10 µm. Thicknesses of 5 µm and 20 µm were also fabricated. SU-8 2010 was spread on top of the substrates containing patterned electrodes at 500 rpm for 15 s and then increase to 3500 rpm for 30 s to form 10 µm thick layers. These substrates were soft baked at 65 °C for 2 min and then for 4 min at 95 °C. UV light exposure was done at 100 mJ/cm^2 and the substrate subsequently post-exposure baked at 65 °C for 2 min and then for 5 min at 95 °C. Finally, substrates were developed for 1 min using SU-8 developer (Kayaku Advanced Materials Inc.). The additional substrates with SU-8 layers of 5 µm and 20 µm thick were fabricated using SU-8 2005 and SU-8 2015, respectively. Each substrate provides 6 devices, 3 with microwells of 20 µm in diameter and 3 with 15 µm.

To obtain the microfluidic channels, a master mold for PDMS molding was fabricated on a prime silicon wafer of 4-inch diameter using SU-8 2015 with a thickness of 18 µm. A 10:1 mass

ratio of PDMS base and curing agent (Sylgard 184 silicone elastomer kit) was poured onto the master mold and cured in an oven at 100 °C for 1 hour. Afterward, the polymerized PDMS was peeled off and inlet/outlet holes were created on the channels using a disposable biopsy punch (Robbins Instruments Inc.) and subsequently cleaned with IPA and milli-Q water.

3.2.3   Bonding and assembly

Microfluidic channels on PDMS structures were irreversibly bonded to the fabricated glass devices containing SU-8 microwells by silanization, using APTES (3-Aminopropyl)triethoxysilane 99%. Traditionally, oxygen plasma is used to irreversibly bond PDMS to glass surfaces when prototyping microfluidic devices. However, our microfluidic device has a SU-8 layer on top of the glass, which does not result in the creation of -SiOH groups after the plasma treatment [106]. With the silanization process, APTES molecules (CH_3CH_2O- and NH_2) are bound to the plasma-treated PDMS surface. CH_3CH_2O will react in one end with the –SiOH group on the PDMS, while the other end (NH_2) will react with the epoxy group on the SU-8 surface forming strong covalent bonds [106]. The schematic representation of the bonding method is shown in Figure 3.6.

First, the channel side on the PDMS was exposed to oxygen plasma using a reactive-ion etching machine (Trion Technology, Inc.). After the surface activation, the channel side was immersed in a liquid solution containing 99% (3-aminopropyl)triethoxysilane(APTES) for 45 s. Afterward, the PDMS was washed with milli-Q water and dried using nitrogen gas. Immediately after this, the PDMS and our device (glass + SU-8) were carefully aligned and brought into contact. The structure was baked on a hot plate at 150 °C for 1 hour while a standard calibration weight of 200 grams was applied on top. Finally, 21G stainless steel connectors were inserted into the input and output holes in the PDMS and connected to PTFE tubing (Elveflow Microfluidics).

49
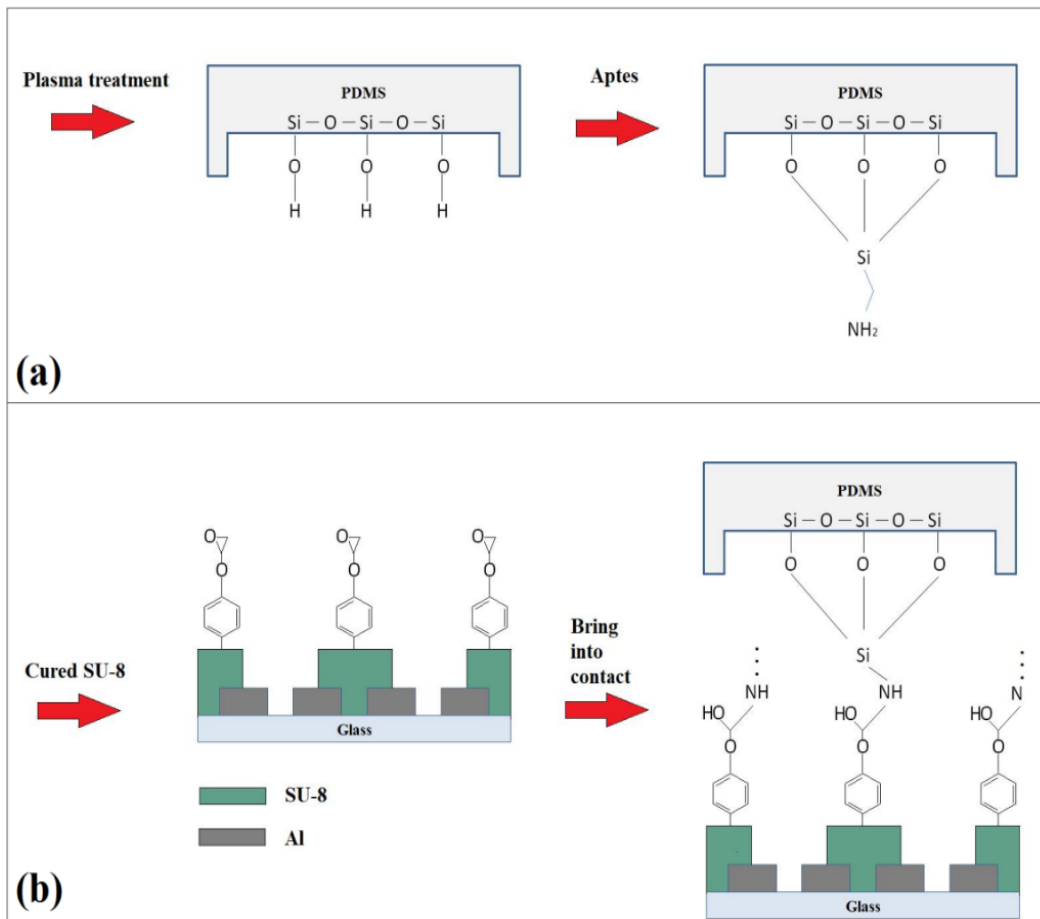
Figure 3.6: Bonding process: (a) Silanization of plasma-treated PDMS using APTES. (b) Epoxy-groups on the SU-8 surface react with NH_2 on the PDMS surface when bring into contact.

3.2.4   Instrumentation and experimental setup

The employed instrumentation is similar to what we employed with the Coulter counter device.

The custom-made chip-holder introduced in section 3.2.1 is based on spring-loaded pogo-pins

(Mill-Max Corp.) and was used to electrically connect our microfluidic device to all external

equipment. A set of switches in the holder allowed us to control the signal applied to each

microelectrode. The flow of ascospores in solution within the microfluidic channel was generated

and controlled using the same syringe pump (New Era Pump Systems Inc. NE-1000). During DEP

experiments, sinusoidal signals were applied to the microelectrodes via the chip-holder by using a function generator (Rigol DG822) through a bipolar 10X amplifier (Tabor Electronics 9250). An oscilloscope (Tektronix TDS 2012B) was also used to monitor the applied signal. nF-EIS measurements were performed using a high precision impedance analyzer (Zurich Instruments MFIA) controlled by the software LabOne.

3.2.5 Reagents and ascospore production

S. sclerotiorum ascospores were produced as described in Chapter 1. To prepare ascospores in solution, the filter paper discs were cut into small pieces (approximately 2 mm x 10mm) and inserted in a 2 mL centrifuge tube containing 1.5 mL of ultrapure Milli-Q water with a resistivity of 18.2 MΩ cm^{-1} (Sigma-Aldrich). Subsequently, the tube was shaken for 45 s at 1500 rpm using a digital vortex mixer (Fisher Scientific). The piece of paper was then removed from the tube and the solution was filtered using a cell strainer (PluriSelect) with a 20 µm mesh. During DEP experiments spores were resuspended in our DEP loading buffer, consisting of 1% w/v bovine serum albumin (BSA) in milli-Q water to avoid non-specific binding of spores.

3.3 Experimental Results and Discussion

3.3.1 DEP-assisted capture of ascospores

To evaluate the performance of our device for capturing *S. sclerotiorum* ascospores, I designed two sets of experiments. In the first set, the occupancy distribution of captured ascospores was examined as a function of the applied flowrate. Devices having microwells with diameters of 20 µm and 15 µm were tested. Prior to loading ascospores, ethanol was slowly injected into the device at a flowrate of 2 µL/min in order to remove air bubbles within the microwells. Afterward, our

DEP buffer was introduced into the channel at the same flowrate for 10 min. Subsequently, 10 µL

of stained *S. sclerotiorum* ascospores at a low concentration of approximately 4.4×10^4 spores/mL,

measured with a conventional hemocytometer, were pumped into the device at a fixed flowrate of

0.2 µL/min.

While the ascospore suspension was flowing, a sinusoidal signal of 20 Vpp and 300 kHz

was applied to the electrodes to enable positive DEP capture. Once the entire ascospore volume

(10 µL) was pumped, a washing step was implemented to remove remaining ascospores on the

SU-8 surface by increasing the flowrate to 15 µL/min for 2 minutes, while keeping the DEP signal

on. Flowrates of 0.4 and 0.8 µL/min were also examined, and three independent experiments were

performed for each flowrate. The obtained results are summarized in Figure 3.7.
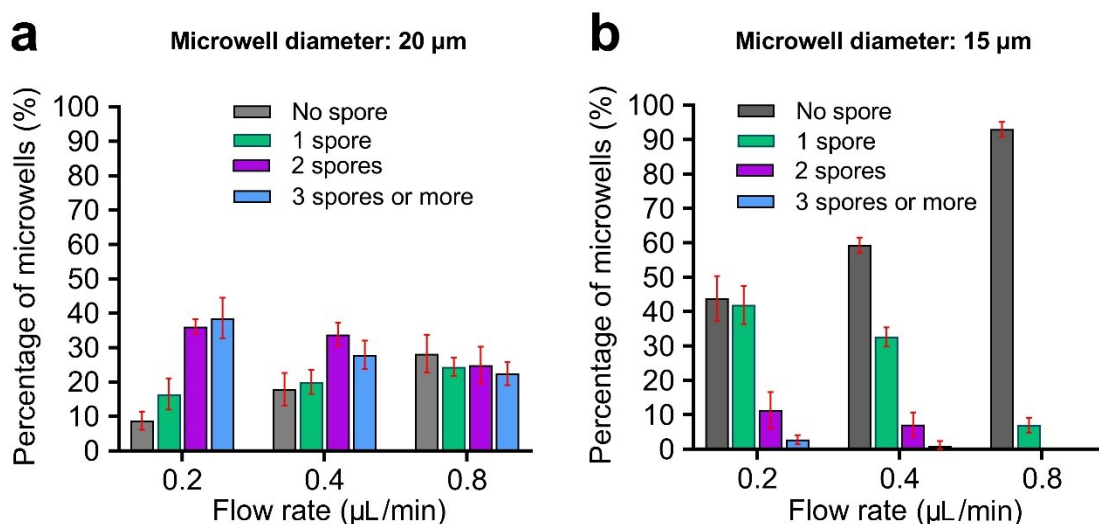
Figure 3.7: Ascospore occupancy employing DEP assisted loading. Each bar shows the mean value of three independent experiments and represents the number of microwells occupied by zero, one, two and three or more ascospores. The total number of microwells is 190. (a) Ascospore occupancy as a function of the applied flowrate for devices in which microwells have a 20 µm

diameter and employing a sinusoidal DEP signal of 20 Vpp at 300 kHz. (b) Same as (a) but with microwells of 15 μm diameter.

A high ascospore occupancy of 91.23% was achieved in devices with microwell diameters of 20 μm, subjected to a flowrate of 0.2 μL/min (Figure 3.7a) and with more than 70% of the microwells occupied by at least 2 ascospores. As expected, ascospore occupancy decreases as the flowrate increases, with an average occupancy of 83.11% and 71.86% for flowrates of 0.4 and 0.8 μL/min, respectively. It was also verified that the percentage of single ascospores increased from 16.49% to 24.38% when the flowrate increased from 0.2 to 0.8 μL/min. The average velocity of ascospores increases as the flowrate increases, and thus the drag force acting on them, decreasing the number of ascospores captured with the same DEP signal amplitude. The same trend was observed in devices with microwells of 15 μm diameter (Figure 3.7b) and almost no triplets were present after the washing step.

The difference in occupancy levels between the two devices can be attributed to two main reasons: a reduction in the cross-sectional area of the channel due to a smaller constriction and a larger attenuation of the electric field due to smaller microwells. The microfluidic channel constriction (Figure 3.1b) is 420 μm and 320 μm for devices with microwells of 20 μm and 15 μm diameter, respectively. By the continuity equation, we know that as the cross-sectional area of our microchannel is reduced, the mean velocity of ascospores increases for a constant flowrate [107]. Therefore, for the same flowrate, ascospores are flowing around 32% faster in devices with microwells of 15 μm diameter. Furthermore, SU-8 is an insulator and as the diameter of the microwells is reduced, a larger attenuation of the electric field and thus the DEP effect is obtained. Figure 3.8 shows fluorescence microscopy images of ascospores captured at different flowrates.
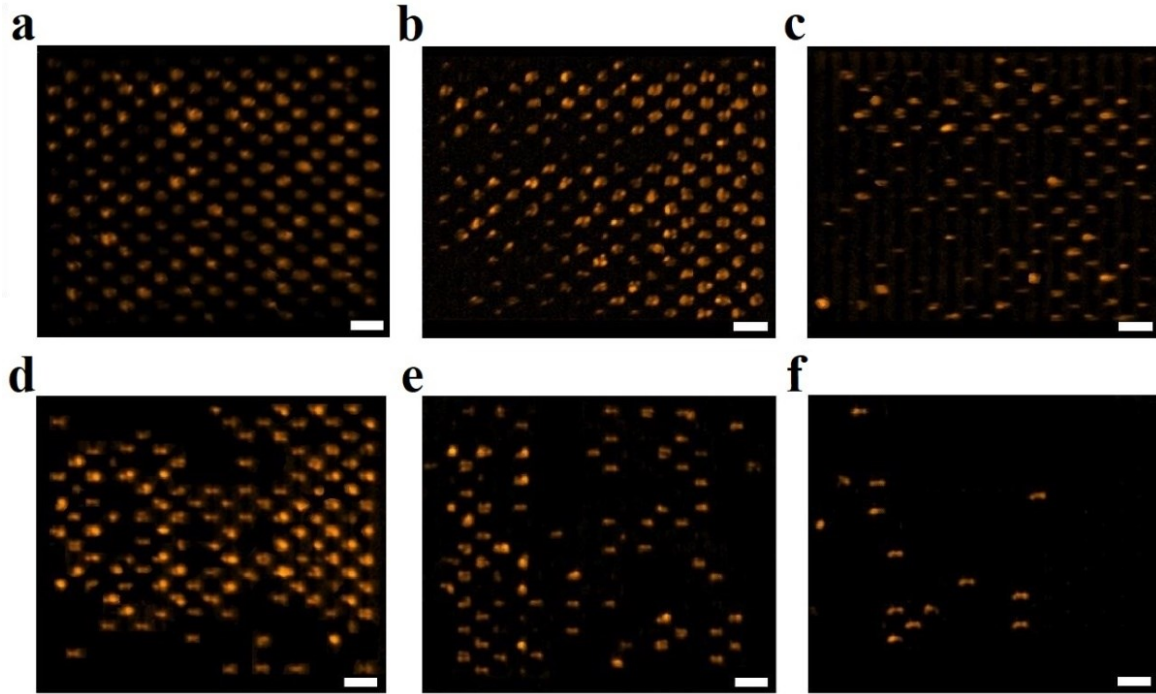
Figure 3.8: Ascospore occupancy as a function of flowrate. The applied DEP signal was 20 Vpp at 300 kHz and the pumped volume was 10 µL. Devices with microwells of 20 µm diameter and applied flowrate of: (a) 0.2 µL/min (b) 0.4 µL/min and (c) 0.8 µL/min. Devices with microwells of 15 µm diameter and applied flowrate of: (d) 0.2 µL/min (e) 0.4 µL/min and (f) 0.8 µL/min. Scale bars are 40 µm.

In the second set of experiments, the influence of microwell depth with regards to occupancy distribution of captured ascospores was evaluated at a constant flowrate of 0.2 µL/min. In addition to the previously described chips showcasing a microwell depth of 10 µm, devices with microwell depths of 5 µm and 20 µm were also fabricated. The DEP signal amplitude and frequency, the concentration of ascospores, and the injected volume were kept the same as in the previous experiment. The results obtained during these experiments are summarized in Figure 3.9. As expected, high spore occupancy (92.35%) was observed in devices with microwells of 20 µm diameter and 5 µm depth (Figure 3.9a). On the other hand, the occupancy in devices with

microwells of 15 μm diameter and 5 μm depth was on average 79% with more than 45% of the microwells occupied by doublets (Figure 3.9b).
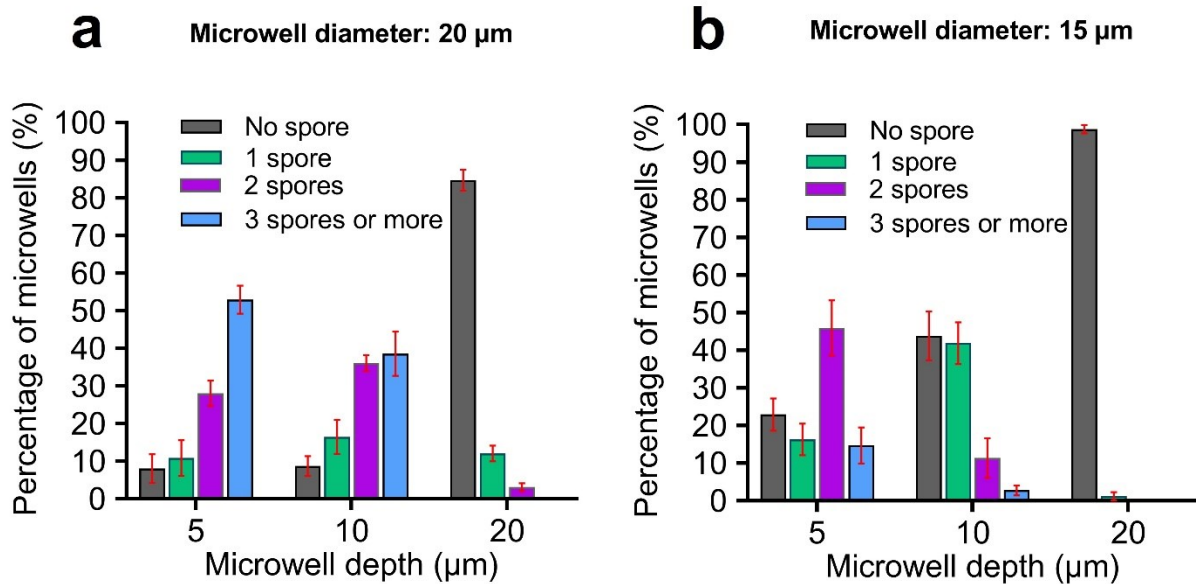
Figure 3.9: Ascospore occupancy employing DEP assisted loading. Each bar shows the mean value of three independent experiments and represents the number of microwells occupied by zero, one, two and three or more spores. The total number of microwells is 190. (a) Ascospore occupancy as a function of microwell depth: the diameter of the microwells is 20 μm and the applied DEP signal is 20 Vpp at 300 kHz. (b) Same as (a) but with microwells of 15 μm diameter. Error bars represent the standard deviation.

During the washing step of devices with 5 μm depth, a few ascospores were observed escaping the microwells, particularly those in which there were two or more ascospores already. This issue was solved by increasing the voltage to 22 Vpp during the washing step. Notably, the ascospore capture efficiency decreased drastically for both microwell diameters when the depth of microwells was 20 μm (Figures 3.9a and 3.9b). This can be attributed to the decrease in the intensity of the electric field gradient with the increasing distance from the electrodes surface. We

carried out numerical simulations using commercially available software (COMSOL Multiphysics) to investigate this effect. The simulation domain and the electric field generated by the microelectrodes are shown in Figure 3.10, where the electric field intensity $|E|$ is represented with a color map.
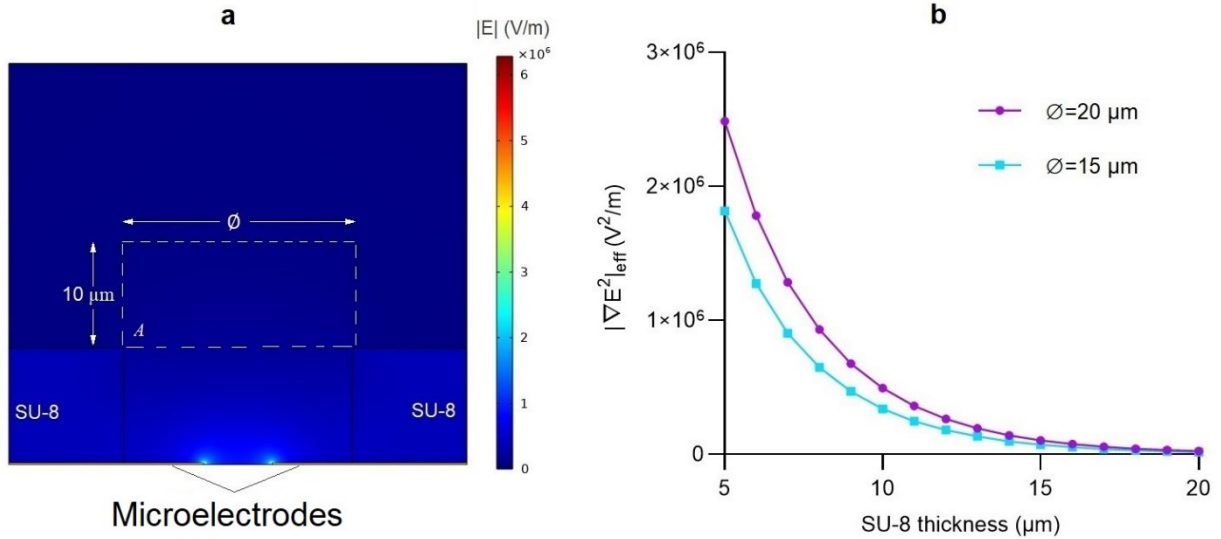
Figure 3.10: COMSOL simulations: (a) Simulation domain and color map of electric field intensity generated by microelectrodes. The white dashed rectangle A represents the integration boundaries of the electric field gradient ($\nabla|E|^2$) with a fixed height of 10 μm and width equal to the microwell diameter Ø. (b) Simulation of the effective electric field gradient $\nabla|E|^2_{eff}$ as a function of SU-8 thickness. The effective gradient is proportional to the DEP force acting on ascospores and decreases exponentially with the increase of SU-8 thickness. The voltage used in these simulations and applied to the microelectrodes was the same as the experimental voltage (20 Vpp).

As per equation (2.4), the gradient of the squared electric field $\nabla|E|^2$ is directly proportional to the DEP force acting on the ascospores, therefore, we defined the effective gradient as: $\nabla|E|^2_{eff} = \int \nabla|E|^2 dA$, which represents the magnitude of the electric field gradient ($\nabla|E|^2$)

integrated over the white dashed rectangle of area A above the microwells, shown in Figure 3.10a, with a fixed height of 10 µm and width given by the microwell diameter. The simulation of the effective gradient as a function of SU-8 thickness is shown in Figure 3.10b. We can see that as the thickness of the SU-8 layer increases, the effective gradient decreases exponentially and therefore the DEP force also decreases.

This means that as the microwell depth increases, the DEP capture efficiency will decrease exponentially, which was clearly observed in our experiments. It is also important to point out that we also tested ascospore loading in all our devices using nothing but gravity. However, in all cases, all the microwells were empty, which indicates that the DEP force was the dominant force in capturing ascospores into microwells. Figure 3.11 shows HIM images of ascospores captured inside microwells using DEP.
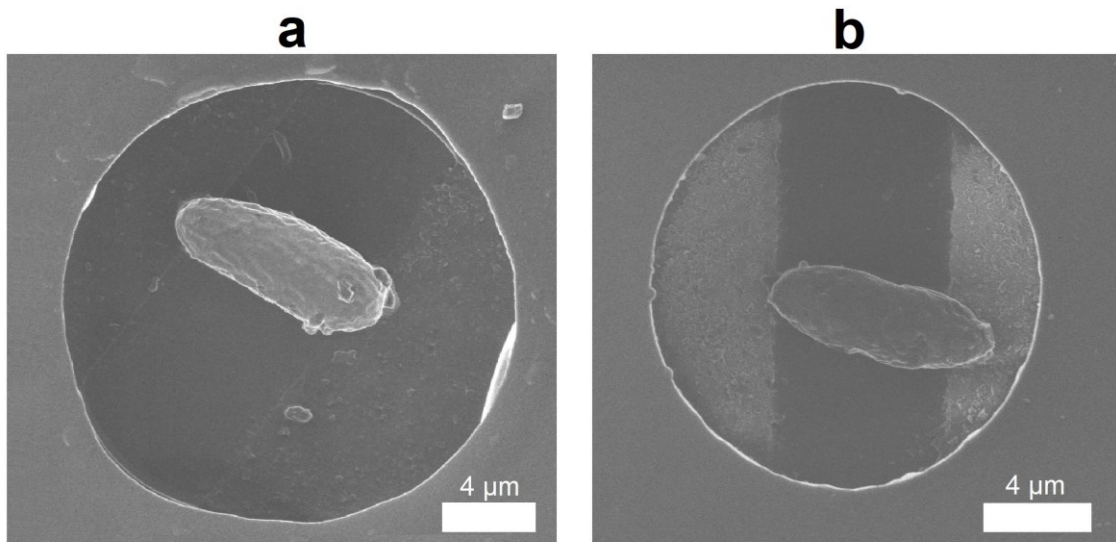
Figure 3.11: HIM image of *S. sclerotiorum* ascospores inside microwells captured by dielectrophoresis force. (a) Single ascospore in a microwell of 20 µm diameter; (b) Single ascospore in a single microwell of 15 µm diameter. The applied DEP signal was 20 V_{pp} at 300 kHz.

Ascospores were fixed for HIM imaging using 4% paraformaldehyde in PBS with 0.1% Triton X-100.[10] First, ascospores were introduced into the device and captured using DEP. After this, 1 mL of the paraformaldehyde solution was pumped into the device manually and left to rest for 15 min. Secondly, PBS 1X was introduced for 10 minutes to rinse the microwells. Lastly, captured ascospores were dehydrated by introducing ethanol of graded concentrations, which were 20% for 5 min, 40% for 5 min, 60% for 5 min and 80% for 5 min. Images were taken employing the HIM microscope at the facilities of nanoFab.

Based on the results presented above, it is evident that our devices can effectively capture ascospores into the microwells using DEP. The frequency was chosen by observing the DEP response of ascospores in our DEP buffer, in the same way that it was done in the previous chapter. At 300 kHz, a stronger pDEP response was observed. Devices with 20 μm diameter and 5 μm depth provided higher capture efficiency and flexibility to account for the ascospore size variability. Devices with 15 μm diameter and 5 μm depth provided a lower number of ascospores per microwell when compared to devices with microwells of 20 μm diameter, and the overall capture efficiency could be increased by, for instance, reducing the flowrate, at the expense of an increase in capture time.

3.3.2   Impedimetric quantification of *S. sclerotiorum* ascospores

After capturing ascospores into the microwells, we employed nF-EIS to quantify them. During this process, microelectrodes are operated individually (Figure 3.2c), allowing for impedance measurements of each column in the microwell array by applying an AC potential from the

---

impedance analyzer to the respective pair of microelectrodes located beneath each microwell (Figure 3.1b). To test the performance of our quantification method, we first pumped a solution with a low concentration of ascospores (~2x10^4 spores/mL) at a flowrate of 0.2 μL/min into the device. Subsequently, we used DEP to capture single ascospores into a fixed column of the microwell array. Every time a single ascospore was captured in a microwell of the respective fixed column, the DEP signal was turned off, and the impedance spectrum was recorded from 5 kHz to 1 MHz. This process of capturing ascospores in a fixed column is shown in Figure 3.12.
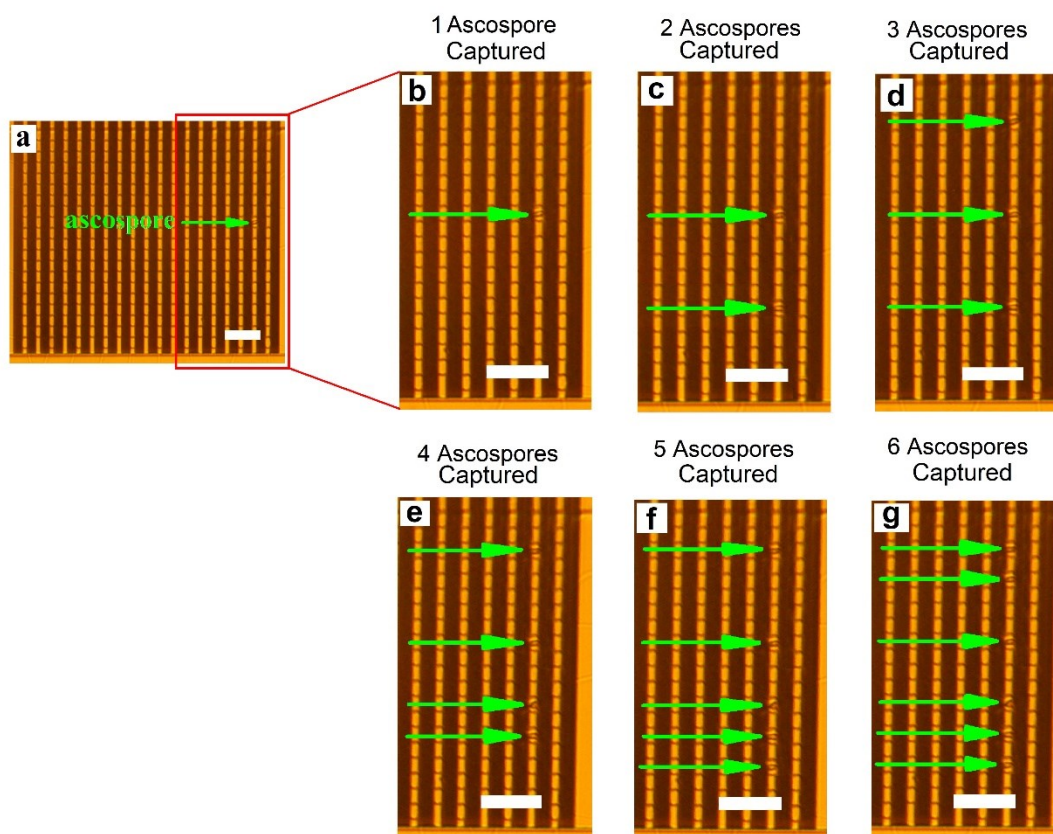
Figure 3.12: Ascospore capture in a single column using DEP. The flowrate was 0.2 μL/min from left to right and the applied DEP signal was 20 Vpp at 300 kHz. After every single ascospore was captured, the DEP signal was turned off and impedance measurements were recorded in the frequency range of 5kHz-1MHz. The DEP signal was turned back on after the impedance

measurements were completed and only when a flowing ascospore was in the trajectory of an empty microwell of the same column. Flowing ascospores were monitored through the microscope camera. (a) Entire microwell array showing a single ascospore captured at a fixed column. The number of captured ascospores in a fixed column increases from (b) to (g). Scale bars are 50 µm.

Flowing ascospores were monitored using the microscope camera to ensure that no ascospore was captured in a microwell that was already occupied. Thus, the DEP signal was turned back on only when an ascospore was flowing in the direction of an empty microwell of the same column. During the impedance spectrum measurement, which takes approximately 20 s, none of the captured ascospores escaped from the microwells, even when the DEP signal remained off for a longer time. The typical magnitude response of a single column in the microwell array as a function of the number of captured ascospores and for devices with microwells of 20 µm diameter is shown in Figure 3.13.
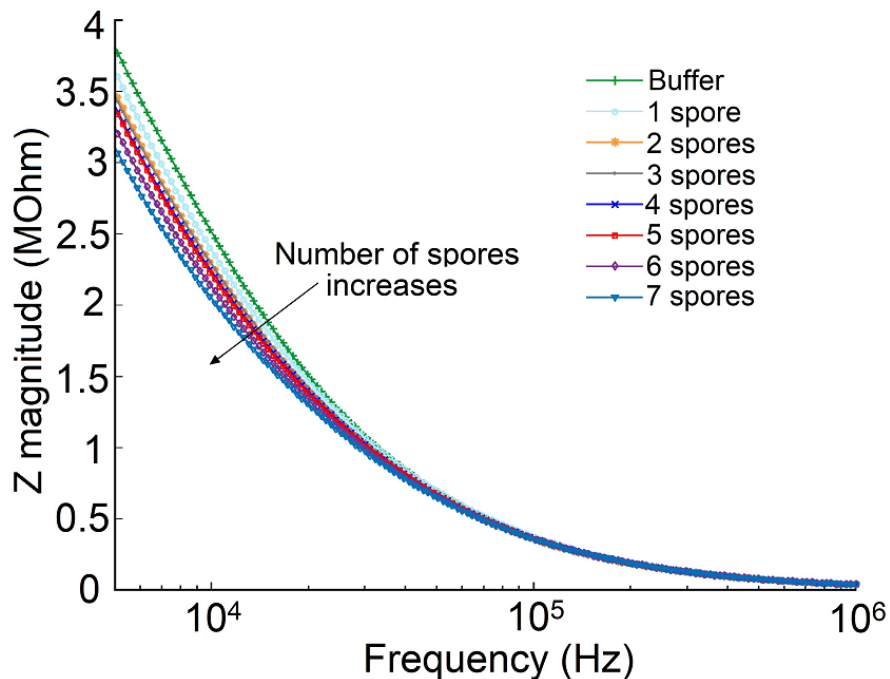
Figure 3.13: Magnitude of the impedance versus frequency as a function of the number of single *S. sclerotiorum* ascospores captured in a column of the microwell array. Diameter of microwells is 20 μm.

On the other hand, the typical phase response of a single column in the microwell array as a function of the number of captured ascospores and for devices with microwells of 20 μm diameter is shown in Figure 3.14.
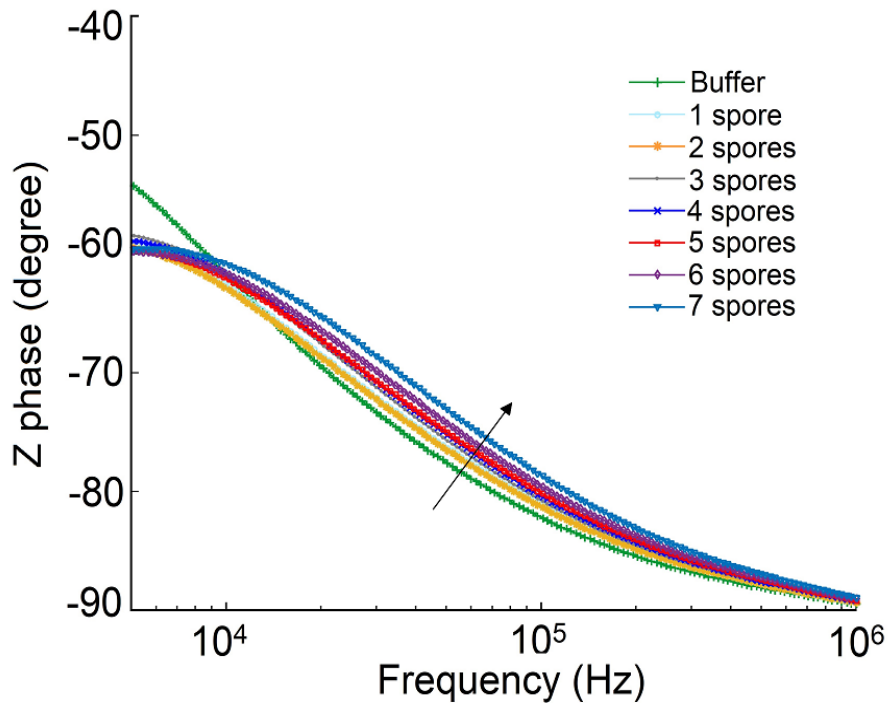
Figure 3.14: Phase of the impedance versus frequency as a function of the number of single *S. sclerotiorum* ascospores captured in a column of the microwell array. Diameter of microwells is 20 μm.

As expected in a capacitive-based sensor, magnitude curves decrease (Figure 3.13) and phase curves tend to -90° (Figure 3.14) as the frequency increases. The experimental Nyquist plot and

the equivalent circuit model with such responses is shown in Figure 3.15. R_m models the solution resistance which is in parallel with the solution capacitance C_s. The constant phase element (CPE) models the electrical double-layer at the electrodes, all in parallel with a parasitic capacitance C_p, which, as explained in the previous chapter, accounts for parasitic effects introduced by the connection cables, chip-holder and substrate. This is a simplified equivalent circuit, commonly used to describe the electrode-electrolyte interface in interdigitated electrode sensors [108].
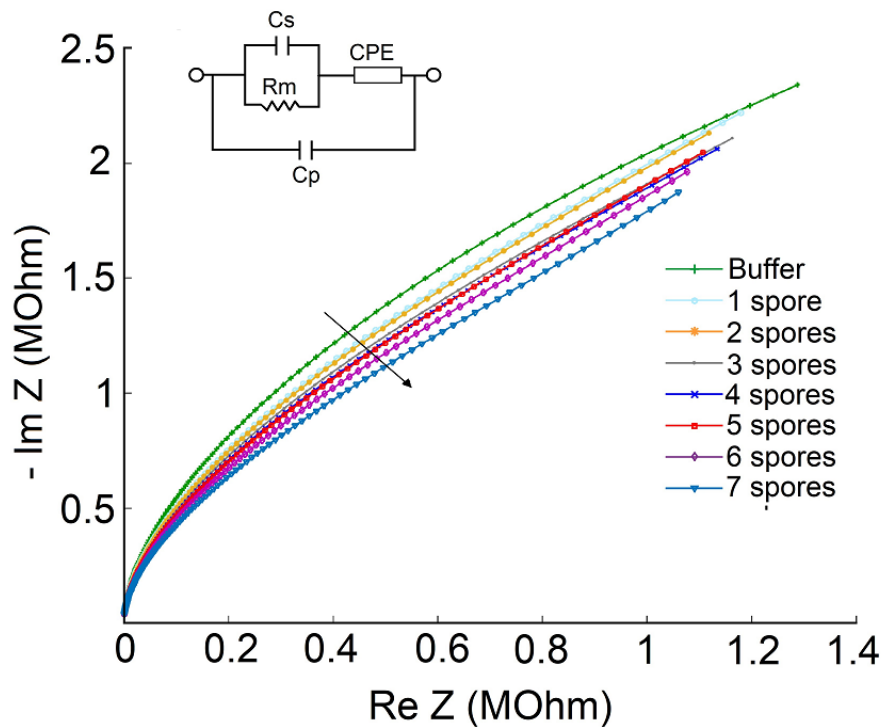
Figure 3.15: Nyquist plot with equivalent circuit model as a function of the number of single *S. sclerotiorum* ascospores captured in a column of the microwell array. Diameter of microwells is 20 μm.

By fitting the experimental data to the equivalent circuit, we verified that captured ascospores will mainly induce changes in R_m, C_s and CPE, contributing to the total impedance

change of the system. Fitting results had chi-square values less than 0.023. and are shown in Figure 3.16.

The impedance measurements curves clearly show that changes in the number of captured ascospores can effectively modulate the impedance response of our device. It is important to mention that in these experiments, seven ascospores per column were captured since as the microwells of a single column were filled, it became more difficult to prevent two ascospores from occupying the same microwell.
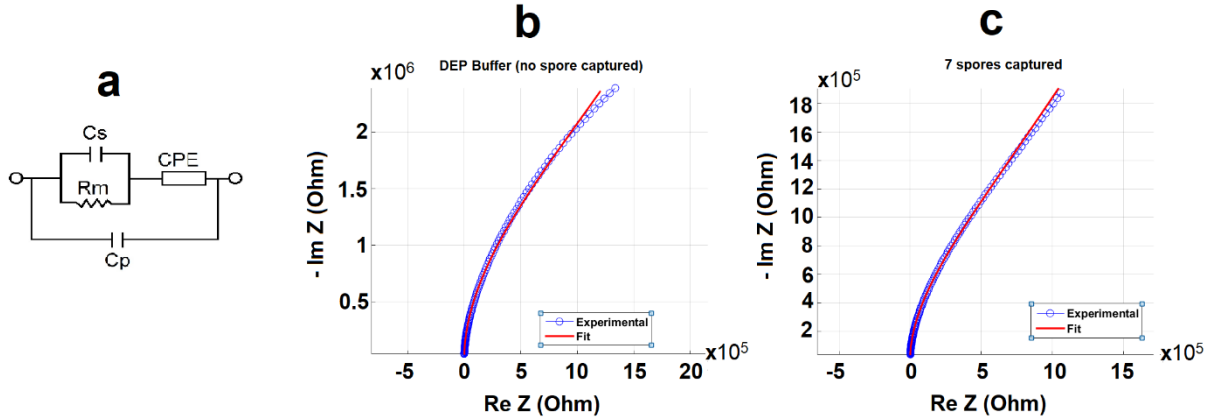
Figure 3.16: Fitting by equivalent circuit. (a) Equivalent circuit employed to fit experimental data. R_m models the solution resistance, in parallel with the solution capacitance (C_s), which are in series with a constant phase element (CPE) that models the electrical double-layer at the electrodes, all in parallel with a parasitic capacitance (C_p), which accounts for parasitic effects coming from the connection cables, connector and substrate. (b) Fitting by equivalent circuit when no spores were captured and the microwells are only filled with buffer. (c) Fitting by equivalent circuit when 7 spores were captured in a column of the microwell array. By fitting each experimental data, we verified that as the number of captured spores increases, R_m decreases while C_s and CPE increases, contributing to the total impedance change of the system.

In order to account for variations in the impedance response of each column in the microwell array, we defined the normalized impedance as,

$$|Z_{norm}| = \left| \frac{Z_{spore} - Z_{buffer}}{Z_{buffer}} \right| \qquad (3.1)$$

where Z_{spore} is the impedance response due to captured ascospores in microwells, and Z_{buffer} is the impedance response given by the buffer. Thus, the calibration curve for the normalized impedance magnitude at frequencies of 5 kHz and 20 kHz is shown in Figure 3.17, in which each point represents the average value of three independent experiments (N=3) performed in different columns of the microwell array.
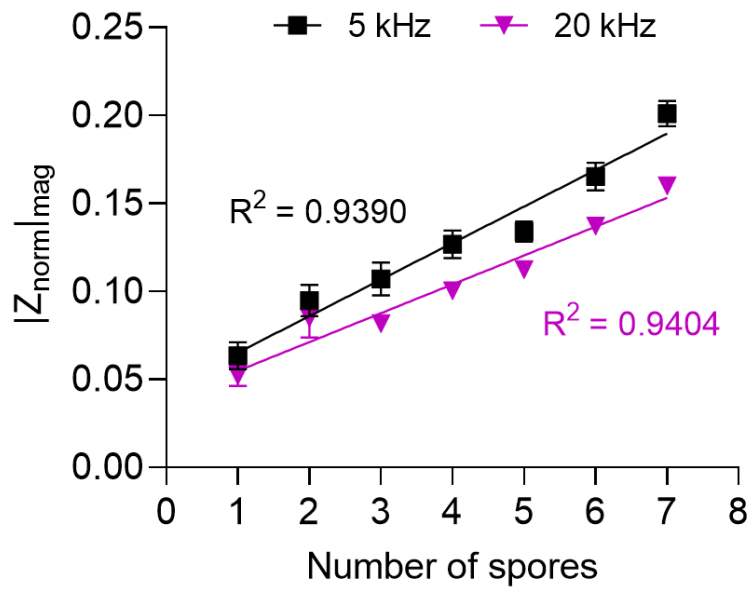
Figure 3.17: Calibration curve of the normalized impedance magnitude at 5 kHz and 20 kHz (N=3) in devices with microwells of 20 μm diameter.

By fitting the experimental data with a linear regression, an R^2 value of 0.9390 with a slope of 0.020 was obtained for 5kHz. Whereas for 20 kHz the R^2 value was 0.9404, with a slope of 0.016. We can express the sensitivity as the percentage of impedance change per captured ascospore by simply multiplying the slopes by 100, yielding a sensitivity of 2%/spore at 5 kHz and 1.6%/spore at 20 kHz. These curves clearly indicate that it is possible to quantify ascospores with our device and that the sensitivity decreases with frequency, which was expected by the spectra obtained in Figure 3.13. The linearity, on the other hand, was very similar for both frequencies.

As described in the previous section, depending on conditions of flowrate and device geometry, more than one ascospore could get captured in a single microwell using DEP. Thus, I carried out an experiment to determine the impedance change due to ascospores in a single microwell. The calibration curve (N=3) for the normalized impedance magnitude is shown in Figure 3.18. No more than 4 ascospores could be captured in the same microwell and the R^2 and slope values obtained for 5 kHz were 0.8061 and 0.017, respectively, while the values for 20 kHz were 0.7869 and 0.007.
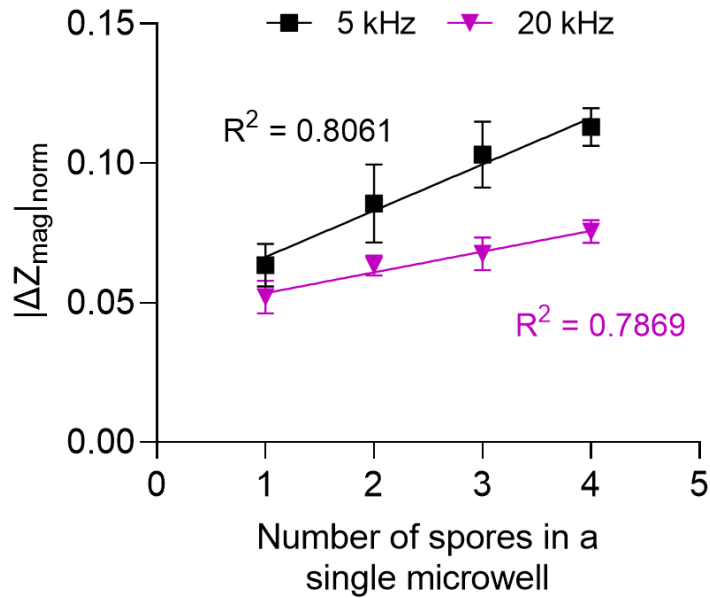
Figure 3.18: Calibration curve of the normalized impedance magnitude at 5 kHz and 20 kHz when ascospores are captured in a single microwell with 20 μm diameter (N=3).

This experiment was very challenging as it was critical to capture ascospores in a single microwell of a column. However, on many occasions, ascospores were captured in different microwells of the same column, and the experiment had to restart. As expected, the microwell dimensions limited the number of ascospores that can be captured and, as the number of ascospores increased, the area of exposed microelectrodes was reduced. We also noticed that ascospores tend to stack on top of each other partially, and sometimes completely, as the number of ascospores increases, thus reducing the electric field perturbation, which lead to a reduction in the total impedance change as the microwell was filled. These factors can potentially explain the low values for the coefficient of determination that were obtained for these curves, which implies a deviation from a simple linear correlation.

Lastly, we also calculated the calibration curve based on the phase of impedance. The calibration curve (N=3) for the normalized impedance phase is shown in Figure 3.19.
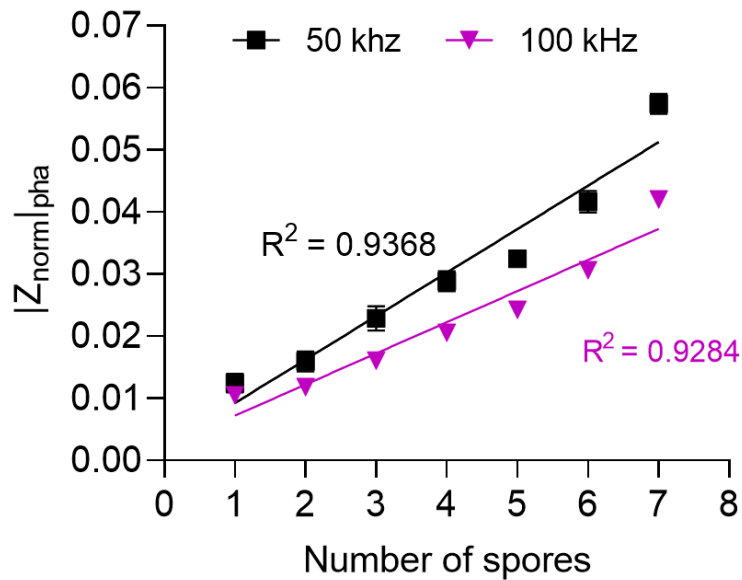
Figure 3.19: Calibration curve of the normalized impedance phase at 5 kHz and 20 kHz (N=3) in devices with microwells of 20 μm diameter.

At 50 kHz, an R^2 value of 0.9368 was obtained with a slope of 0.007, while for 100 kHz, the R^2 was 0.9284 with a slope of 0.005. Although the impedance phase is less sensitive than magnitude, it could still be employed as an alternative or complementary parameter to quantify ascospores.

We repeated the same experiments for chips with microwells of 15 μm diameter. The typical magnitude response of a single column in the microwell array as a function of the number of captured ascospores and for devices with microwells of 15 μm diameter is shown in Figure 3.20.
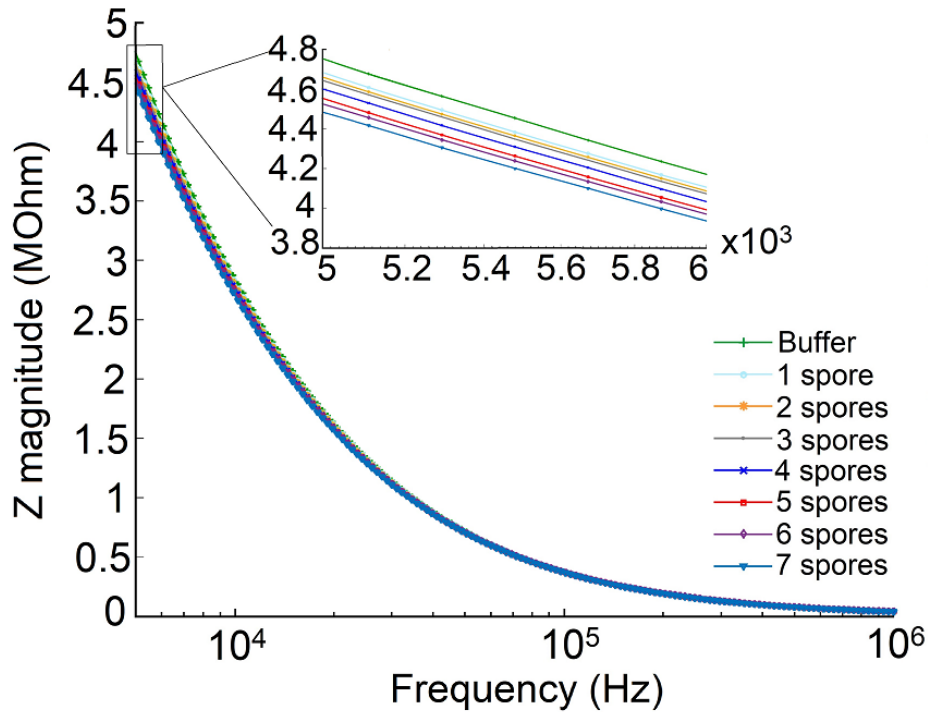
Figure 3.20: Magnitude of the impedance versus frequency as a function of the number of single *S. sclerotiorum* ascospores captured in a column of the microwell array. Diameter of microwells is 15 μm.

With a smaller diameter, a smaller portion of the electrodes surface area is in contact with solution, yielding considerably larger magnitude values when compared to those with microwells of 20 μm diameter. Figures 3.21 and 3.22 show the typical phase response and Nyquist plot for devices with microwells of 15 μm diameter, respectively. As expected, the same trend was obtained for both plots when compared to those obtained for devices having microwells of 20 μm in diameter. To compare the sensitivities, the calibration curves were calculated at the same frequencies.

The calibration curve for the normalized impedance magnitude (N=3) at frequencies of 5 kHz and 20 kHz is shown in Figure 3.23.
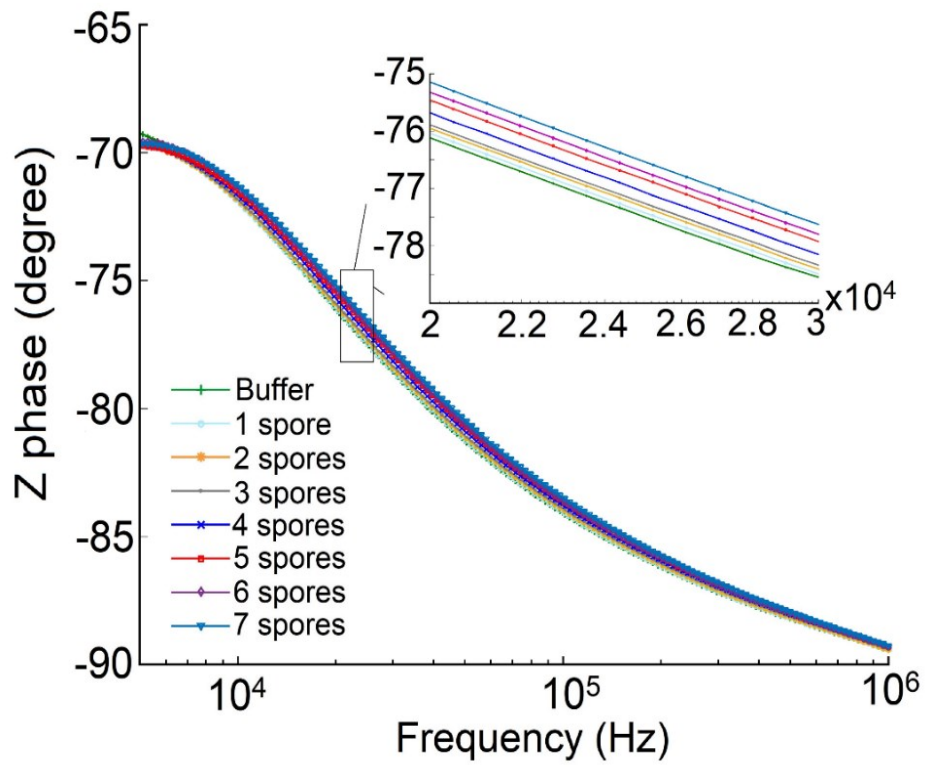
Figure 3.21: Phase of the impedance versus frequency as a function of the number of single *S. sclerotiorum* ascospores captured in a column of the microwell array. Diameter of microwells is 15 μm.
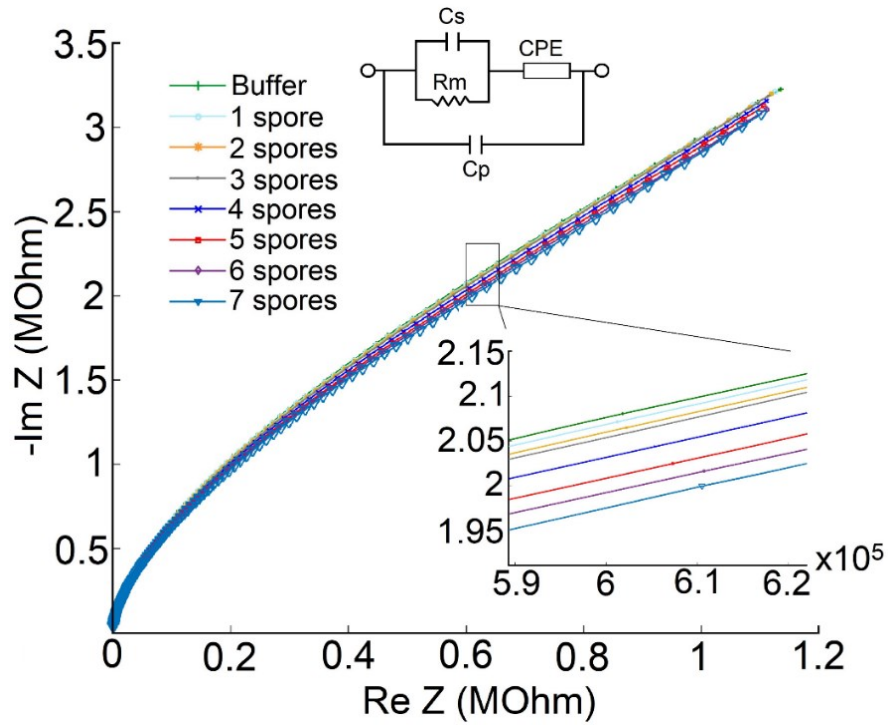
Figure 3.22: Nyquist plot with equivalent circuit model as a function of the number of single *S. sclerotiorum* ascospores captured in a column of the microwell array. Diameter of microwells is 15 μm.
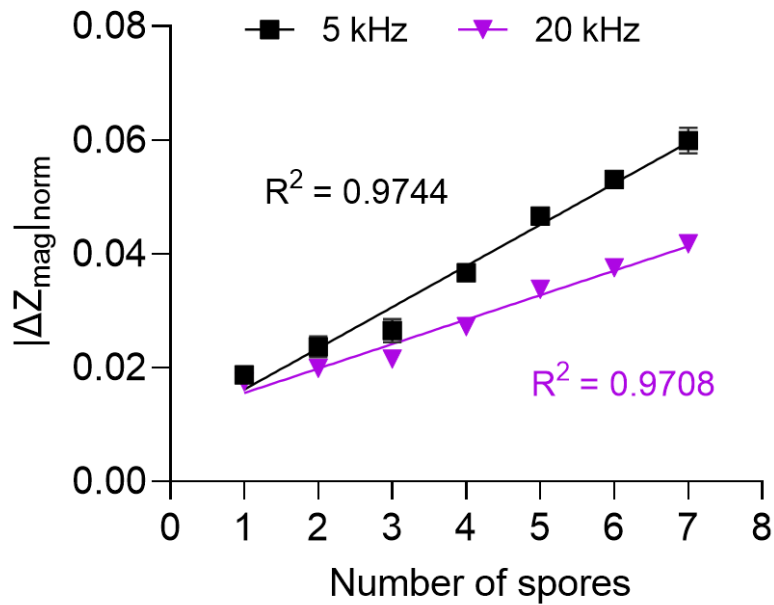
Figure 3.23: Calibration curve of the normalized impedance magnitude at 5 kHz and 20 kHz (N=3) in devices with microwells of 15 μm diameter.

A sensitivity of 0.7%/spore at 5 kHz and 0.4%/spore at 20 kHz was obtained. When capturing ascospores in a single microwell, no more than 3 ascospores could be captured, obtaining a calibration curve with a slope of 0.003 at 5 kHz and 0.001 at 20 kHz, as shown in Figure 3.24.
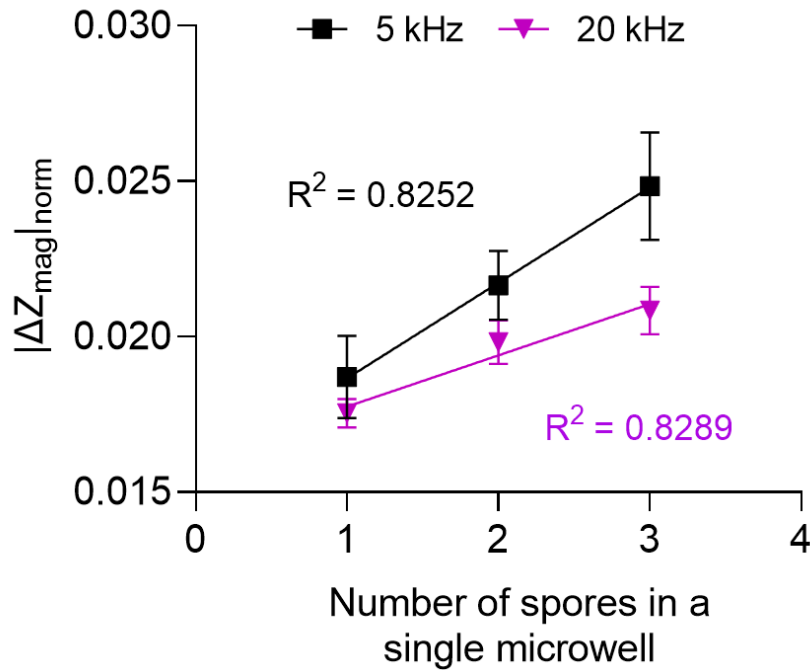
Figure 3.24: Calibration curve of the normalized impedance magnitude at 5 kHz and 20 kHz when ascospores are captured in a single microwell with 15 μm diameter (N=3).

Lastly, the calibration curve (N=3) for the normalized impedance phase is shown in Figure 3.25. At 50 kHz, an R^2 value of 0.9736 was obtained with a slope of 0.002, while for 100 kHz, the R^2 was 0.9750 with a slope of 0.001. The sensitivities achieved are larger than the basic accuracy of our measurement instrument (0.05%) for both microwell diameters, validating the reliability of our results.

The lower sensitivity presented by devices with microwells of 15 µm diameter can be mainly attributed to the reduction of the exposed surface area of the measuring microelectrodes, which naturally increases the double-layer impedance or equivalently, reduces the double-layer capacitance of the measuring system. This is a well-known effect for reducing the sensitivity in impedance measurements [109]. Based on these experiments and the results obtained, devices with 20 µm diameter microwells are more sensitive for ascospore quantification.
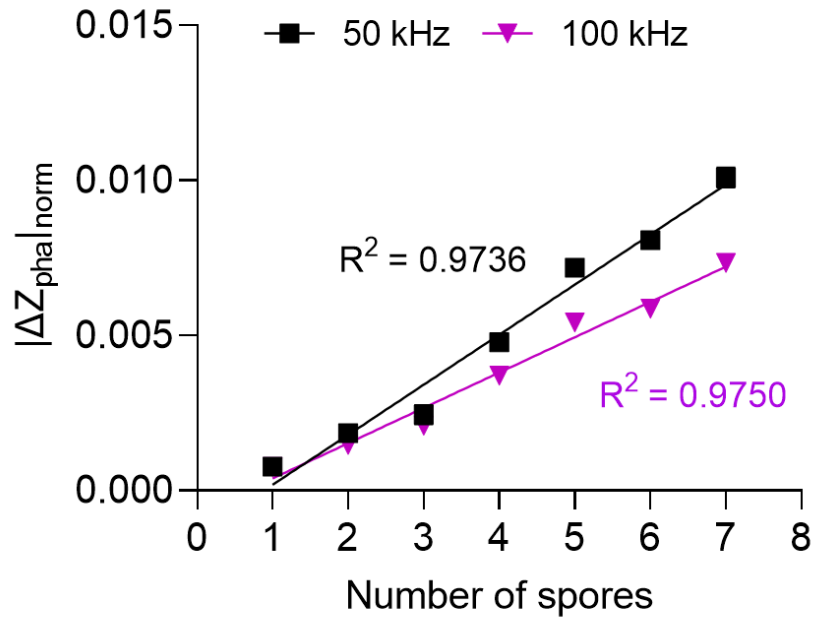
Figure 3.25: Calibration curve of the normalized impedance phase at 5 kHz and 20 kHz (N=3) in devices with microwells of 15 µm diameter.

Lastly, a mixed solution of *S. Sclerotiorum* ascospores and *F. graminearum* spores was prepared, as shown in Figure 3.26. The mixed solution was resuspended in our DEP buffer at a concentration of approximately (2.4×10^4 spores/mL) and pumped into our device for the DEP testing. At 60 kHz, only target ascospores were captured into the microwells, which was expected

based on the results obtained in the previous chapter. At 300 kHz, target ascospores were again captured into the microwells and *F. graminearum* spores were slowed down while flowing through the microwells region, indicating a weak pDEP force, but they were not captured or stopped. Figure 3.27 shows two instances, in which a *F. graminearum* spore enters the microwell region and leaves to the outlet drain. When compared with our previous design, the microwell device provides additional selectivity, given by the physical limitations imposed by the microwell's dimensions. The DEP testing was performed with devices having a 20 µm diameter.
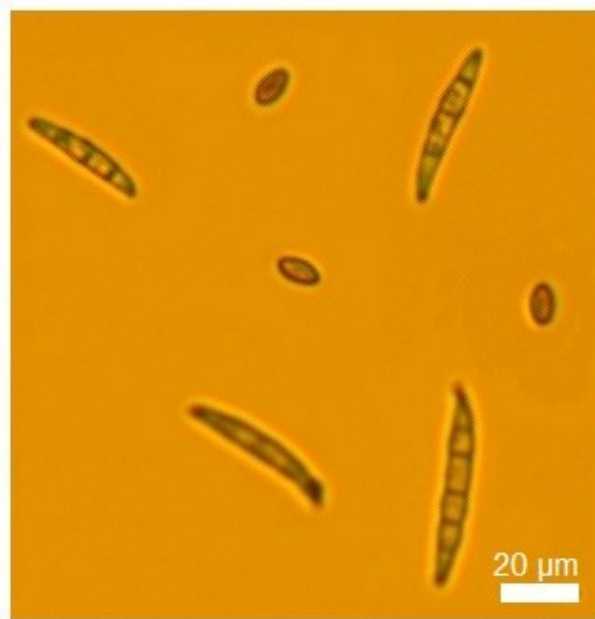
Figure 3.26: Microscopic image of a mixed solution containing *S. sclerotiorum* and *F. graminearum* (macroconidia) spores. *F. graminearum* spores are banana-shaped while *S. sclerotiorum* have ellipsoidal shape.
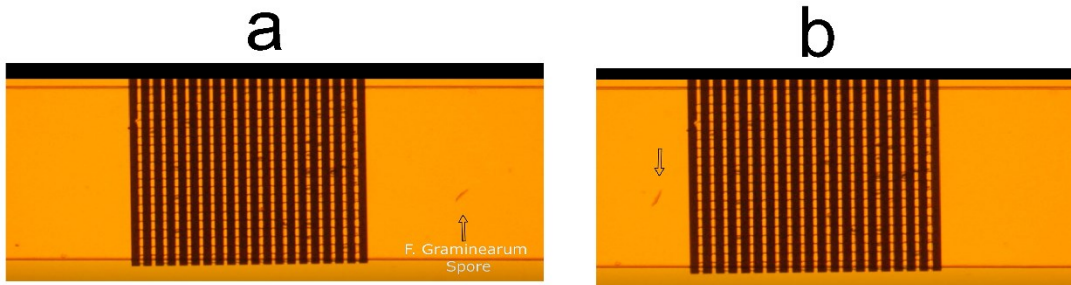
Figure 3.27: *F. graminearum* spore flows through the device without being captured. The frequency of the DEP signal is 300 kHz, which only captured target ascospores. Flowrate was 0.2 µL/min from right to left. (a) Spore enters the microwell region. (b) Spore leaves the microwell region without being captured by DEP.

Through extensive experimentation and characterization, we have demonstrated the feasibility of our new design for the capture and accurate quantification of *S. sclerotiorum* ascospores, well within the sensitivity requirements needed for SSR forecasting applications. When compared to the device presented in Chapter 3, some key issues have been improved. Our current quantification method is based on static rather than dynamic impedance measurements, which increases the sensitivity and reduces the need for instruments with an ultra-fast response time. Moreover, the DEP signal is applied with the same microelectrodes that are employed for impedimetric sensing, avoiding the need for a dedicated structure for DEP trapping and another one for sensing. Lastly, we eradicated clogging issues by increasing our microchannel size but without losing the sensitivity to single ascospores.

Furthermore, and to the best of our knowledge, only a few microfluidic platforms employing microwell arrays and impedimetric sensing have been reported, [102], [110] which are primarily restricted to medical applications. These devices are fabricated with two electrode planes, one under the microwells and the other one on top, reducing the impedance measurement to the whole array, limiting the device sensitivity, and making it immune to changes that occur in single

microwells. In contrast, with our approach, each column in the array can be measured individually, which allows the detection of single particles in a single microwell.

3.3.3 A cell sorting application

Here, I will briefly describe a cell-sorting application employing an electroactive microwell array device that I helped to develop and that had its origin on the chips I designed for the capture and quantification of *S. sclerotiorum* ascospores. The cell sorting project was born as a collaboration between our research group and Dr. Michael Chu from the Alberta's Cross Cancer Institute.[11]

For the cell-sorting application, we increased the number of microwells to 10,000, and instead of having addressable individual microelectrodes, we designed a device with ten independent and addressable interdigitated microelectrodes (IME) structures, named sectors, which allows the DEP-driven capture of cells. Figure 3.28a shows the fabricated device and Figure 3.28b and 3.28c show a close-up of the sectors and microwells, respectively.

---

[11] As mentioned in the preface, the cell-sorting project was led by Lukas Menze. We both extensively collaborate on each other's project.
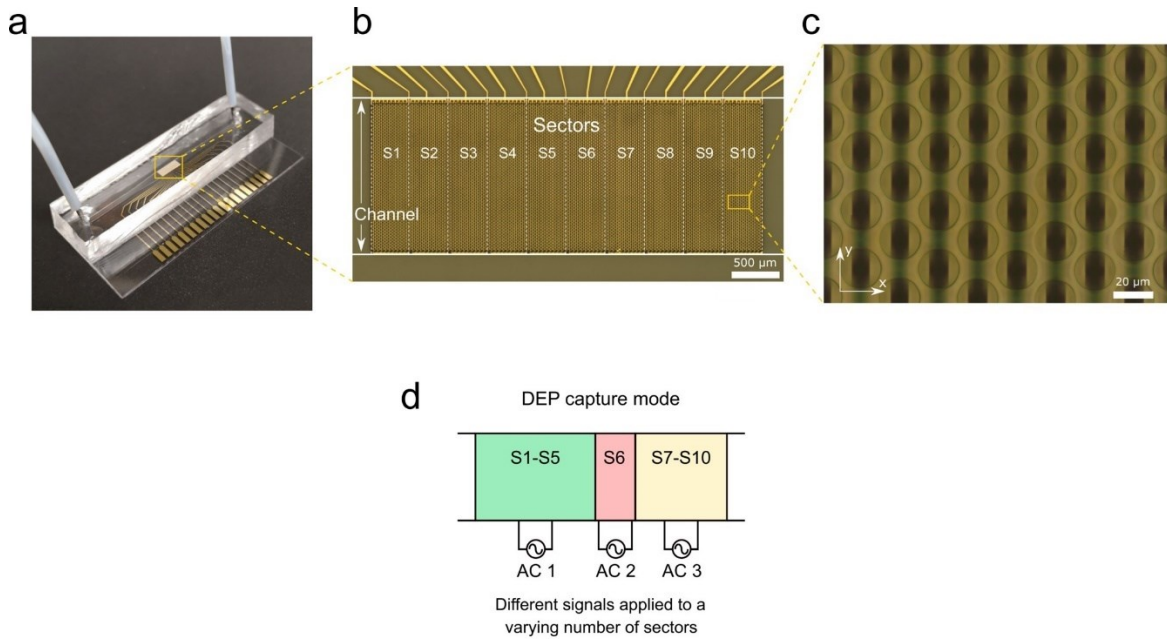
Figure 3.28: A cell sorting application (a) Assembled microfluidic platform. (b) Microscopic image of microwells and sectors. Each of the 10 individually addressable sectors contains 1000 microwells (c) Close-up of the microwells fabricated on top of gold microelectrodes. (d) Each sector can operate individually or combined with adjacent sectors to capture a specific cell type employing DEP force. Figures are courtesy of Lukas Menze.

Each sector contains 1000 microwells and can be operated individually, allowing the application of different DEP signals on each sector, and thus providing the capability of capturing (sorting) different types of cells in different sectors. This operating principle is schematically illustrated in Figure 3.28d.

We tested this device employing a clinically relevant mixed sample composed of benign (MCF-10A) and cancerous (MDA-MB-231) breast cells. The experimental results indicated a benign to cancerous cell capture accuracy of over 95% using a DEP signal of 15 Vpp at 250 kHz, which demonstrated the viability of the platform as a reliable cell sorting device. Typically, the number of cell types that can be sorted by current DEP based cell sorters depends on the number

of output channels. With our design, we remedy this limitation by using the multi-sectorial approach as different cell types can be captured in different sectors.

The process flow and characterization of the device were performed in the same way as the chip for ascospore detection. The complete description of these aspects, as well as details on the experiments performed, can be found in the recent Master's thesis of Lukas Menze [111].

3.4   Conclusions

The primary goal of any SSR forecasting system is to reduce the unnecessary application of fungicides. For this, the effective and rapid quantification of *S. sclerotiorum* airborne inoculum is essential. However, the current lack of simple, cost-effective, and portable platforms that can capture and quantify *S. sclerotiorum* airborne spores has hindered the development of an efficient early warning system.

The device presented here can remedy these limitations through the unique integration of a microfluidic platform and a label-free quantification method that uses dielectrophoresis to reliably capture *S. sclerotiorum* ascospores in solution and into a picoliter well array. Ascospores in the microwells are subsequently quantified using non-faradaic electrochemical impedance spectroscopy employing coplanar nano-thick aluminum electrodes.

Microwell arrays with different diameters and depths were fabricated and extensively tested to determine the optimal conditions for ascospore capture and quantification. We demonstrated a highly efficient ascospore trapping rate of more than 90% and the detection of single ascospores, satisfying the sensitivity requirements to provide an early warning of SSR outbreaks. Due to characteristics like simplicity, and portability, we believe that the future integration of our device

with high throughput spore-trap samplers has great potential for crop protection applications, such as the on-site forecasting of SSR.

Chapter 4

Dielectric Analysis of Ascospores

4.1 Introduction

The dielectric parameters of biological cells are intrinsic properties that are often employed as biomarkers for the label-free separation and differentiation of cells [112]–[114]. These dielectric properties are typically described in terms of the cell's relative permittivity and electrical conductivity, which when combined, give a frequency-dependent dielectric spectrum known as complex permittivity, a concept already introduced in chapter 2 [115], [116]. As most cells have complex heterogeneous structures, the multi-shell theory is commonly used to model them as particles composed of concentric shells, typically in spherical or ellipsoidal format. The dielectric properties of each shell are assumed to be different from each other and homogeneous within each shell [117]. For mammalian cells, the single-shell model is generally used, in which the cell interior (cytoplasm) and the plasma membrane that surrounds it has different relative permittivity and conductivity [112], [115], [116]. For plant cells, fungi, and bacteria, the double-shell model has typically been employed by researchers to account for the dielectric properties of the extra layer (cell wall) that surrounds the membrane [118]–[120].

One of the most common techniques for the dielectric characterization of cells is dielectric impedance spectroscopy, which measures the impedance of a dilute suspension of cells over a

wide range of frequencies [116], [121]. These measurements are then used to extract the dielectric properties employing electrical models that relate the cell's complex structure to passive electrical components, from which the dielectric properties can be determined [110], [117]. The main drawback associated with dielectric spectroscopy is that is limited to cell suspensions [121], [122]. AC electrokinetics techniques, such as dielectrophoresis (DEP) and electrorotation (ROT) have also been extensively used for the dielectric characterization of cells [123], [124]. DEP employs non-uniform electric fields to induce cell movement in a medium of known conductivity, while ROT uses rotating electric fields. By characterizing the motion of cells under these AC fields via the measurement of different parameters such as velocity spectrum [125], induced force [126] rotation rate [127], [128], and cross-over frequency [129], the dielectric properties of different types of biological cells has been determined [114]. One of the main advantages of DEP and ROT is that they can be easily integrated with microfluidic platforms and contrary to dielectric spectroscopy, they can be employed for the measurement of single cells. Moreover, they can also be employed for the manipulation and label-free separation of mammalian cells, plastic beads, and DNA [75], [112], [130].

In this chapter, the dielectric properties of *S. sclerotiorum* ascospores are determined experimentally, employing a dielectrophoretic method. As previously described, when performing the experiments presented in chapters 2 and 3, a lot of time was invested in finding the DEP response of ascospores, which of course changed depending on the conductivity of the employed buffer solution. Although this process was cumbersome and time-consuming, it was necessary because the dielectric properties of *S. sclerotiorum* ascospores are unknown. Finding the DEP response by looking at the movement of ascospores and by iteratively testing different combinations of voltage amplitudes and frequencies of the AC signal used to generate the required

non-uniform electric field allowed us to tunned the DEP filter on both, the Coulter and microwell devices.

To remedy this limitation, we employed a dielectrophoretic method to experimentally determine the dielectric properties of *S. sclerotiorum* ascospores in media of different electric conductivities and using a microfluidic platform. For this, ascospores were modeled using a realistic ellipsoidal double-shell model, from which the dielectric properties were estimated by finding the minimum voltage that balances the DEP and Stoke's drag force acting on ascospores flowing in the microchannel of our device and over a wide range of frequencies (10 kHz to 20 MHz). Prior to performing experiments with ascospores, and in order to verify the validity of the methodology and analysis as well as device validation, the dielectric properties of human embryonic kidney (HEK)-293 cells were estimated and compared with published results.

4.2 Materials and Methods

4.2.1 Operating principle and theory

The experimental determination of the dielectric properties of *S. sclerotiorum* ascospores is based on the measurement of the minimum trapping voltage that balances the DEP and Stoke drag force acting on ascospores flowing in a microfluidic channel [131], [132]. These measurements are performed over a wide range of frequencies (10 kHz to 20 MHz).

The microfluidic device employed in this chapter was fabricated with interdigitated microelectrodes (IME), which, as in our previous devices, enables the generation of a non-uniform electric field for DEP by applying sinusoidal voltages to the IME. Figure 4.1a shows the fabricated device while Figure 4.1b shows a close-up to the IME. Particles flowing through our microfluidic

channel can be trapped at the IME edges with positive DEP (pDEP) or at the top of the microchannel with negative DEP (nDEP), as shown schematically in Figure 4.1c. As described previously, the DEP force acting on a particle can be either positive or negative, depending on whether the particle is attracted towards the region of maximum electric field gradient or repelled from it [102], [133], [134]. The sinusoidal voltages are applied to the IME through a custom-made chip-holder, which is the same as the one employed with the devices described in chapter 3 and is shown in Figure 4.1d.
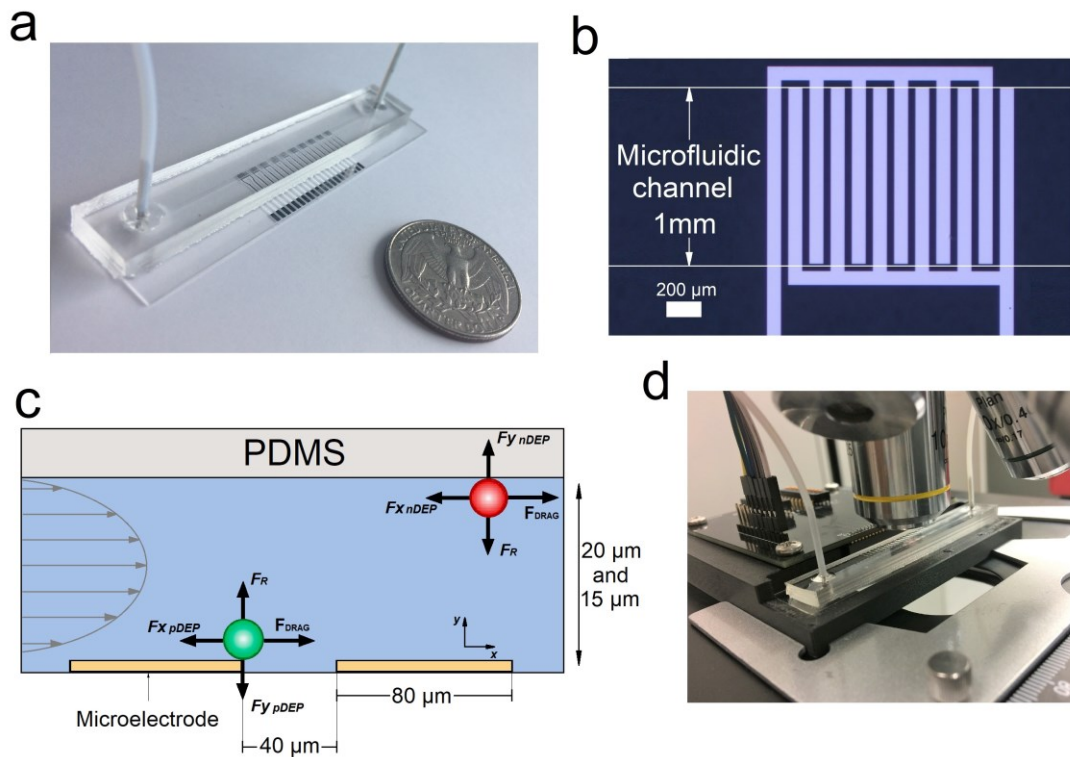
Figure 4.1: (a) Assembled microfluidic device for dielectric characterization. (b) Microscopic image of interdigitated microelectrodes in the microchannel. Microelectrodes employed in experiments have a width and spacing of 80 µm and 40 µm, respectively. Microchannel width is 1mm (c) Schematic representation of the cross-sectional view of the assembled device showing pDEP trapping at the edges of microelectrodes and nDEP trapping at the top of the microchannel. Experiments with cells were performed with a channel height of 20 µm while experiments with

ascospores were performed with a channel height of 15 μm (d) Custom-made chip holder to connect the microfluidic device with external equipment and to facilitate imaging.

Employing the expression for the DEP force F_{DEP}, given in equation 2.7, we can re-write the F_{DEP} in the x-direction for a particle trapped by pDEP as,

$$F_{X\,pDEP} = \pi\varepsilon_m r^3 Re\left\{\frac{\varepsilon_p^* - \varepsilon_m^*}{\varepsilon_p^* + 2\varepsilon_m^*}\right\}\frac{\partial|E|^2}{\partial x} \tag{4.1}$$

For the sake of simplicity, we are omitting the "$< >$" and "$(\;)$"symbols, and $|E|$ is the magnitude of the electric field. We can further simplify equation (4.1) by using the relationship between the electric field and electric potential (Poisson's equation), as demonstrated elsewhere [131], [132],

$$F_{X\,pDEP} = \pi\varepsilon_m r^3 Re\left\{\frac{\varepsilon_p^* - \varepsilon_m^*}{\varepsilon_p^* + 2\varepsilon_m^*}\right\}\frac{\partial|E|^2}{\partial x}\bigg|_{V=1} V^2 \tag{4.2}$$

where V is the amplitude of the sinusoidal voltage applied to the IME. Naturally, under nDEP, the F_{DEP} in the x-direction has the same form as equation (4.2), with the difference that the value of the gradient term will be smaller and the voltage amplitude larger. This component of the DEP force balances the Stoke drag force acting on the particle, which in turn stops the particle from moving in the x-direction. The horizontal Stoke drag force is given by [135],

$$F_{\text{DRAG}} = 6\pi\eta r k(v_f - v_p) \tag{4.3}$$

where η is the fluid viscosity, v_f is the local flow velocity at the center of the particle, v_p is the velocity of the particle, which is zero when the particle is trapped, and k is a nondimensional factor accounting for the wall effect.

Under pDEP, the F_{DEP} in the y-direction pushes the particle to the IME edges and is balanced by the reaction force F_R, preventing the particle to move in this direction. Under nDEP, the F_{DEP} in the y-direction pushes the particle away from the IME and towards the top of the microchannel. It is important to note that the forces of gravity and buoyancy (sedimentation) in the y-direction are also present, but they were omitted to simplify the force diagram and since their difference is typically much smaller compared to the magnitude of the DEP force in this direction.

Under the conditions of fixed flowrate and frequency of the electric field, the minimum DEP trapping voltage that balances the DEP and drag force can be measured to estimate the real part of the CM factor [132]. Thus, equating (4.2) and (4.3), we can isolate the real part of the CM factor:

$$Re\left\{\frac{\varepsilon_p^* - \varepsilon_m^*}{\varepsilon_p^* + 2\varepsilon_m^*}\right\} = \frac{6k\eta v_f}{\varepsilon_m r^2 \left.\frac{\partial |E|^2}{\partial x}\right|_{V=1} V^2} \tag{4.4}$$

By measuring this minimum trapping voltage V at different frequencies, the spectrum of the real part of the CM factor can be obtained, from which the dielectric properties can be later estimated. To validate the methodology, we first performed experiments with HEK-293 cells, as the dielectric properties of this cell line are well known in the literature. Subsequently, experiments with *S. sclerotiorum* ascospores were performed. The values of the wall correction factor, the local

flow velocity, and the spatial gradient of the electric field were simply obtained through numerical simulations using commercially available software (COMSOL Multiphysics 5.6).[12]

4.2.2   Device fabrication

The microfluidic devices employed in this chapter were fabricated using standard photolithography processes on 500 μm thick fused silica substrates with 4-inch diameter. Substrates were first immersed in piranha solution (3:1, H_2SO_4:H_2O_2) for 15 minutes. Subsequently, 100 nm of aluminum was sputtered on top of the substrates. Microelectrodes were patterned using a positive PR AZ1512 (EMD Performance Materials Corp.), which was spread at 500 rpm for 10 s, then increased to 5000 rpm for 40 s, and baked at 100 °C for 60 s. The PR was exposed under 405 nm light at 120 mJ/cm^2 using a high-speed direct-write photolithography tool (MLA150 Heidelberg Instruments) and developed using AZ 400k 1:4 developer (EMD Performance Materials Corp.). The aluminum layer was subsequently etched by wet etching using aluminum etchant type A (Transene Company Inc.). Microelectrodes with different widths and gaps were fabricated. In the experiments described here, microelectrodes with 80 μm width and 40 μm gap were employed. The photomask employed to fabricate these devices are provided in Appendix A (Figure A. 4). Aluminum was selected due to its low cost compared to gold as well as the ease of fabrication with wet etching.

To fabricate the microfluidic channels, a master mold was fabricated on a prime silicon wafer of 4-inch diameter using the negative PR SU-8 2015 (Kayaku Advanced Materials Inc.). SU-8 2015 was spread on the silicon wafer at 500 rpm for 15 s and then increase to 2200 rpm for 30 s to form 20 μm thick layers. These substrates were soft baked at 65 °C for 2 min and then for 4 min

---

at 95 °C. UV light exposure was performed at 150 mJ/cm2 and the substrate was subsequently post-exposure baked at 65 °C for 2 min and then for 5 min at 95 °C. Finally, substrates were developed for 1 min using SU-8 developer (Kayaku Advanced Materials Inc.).

After the master mold was finished, a 10:1 mass ratio of PDMS base and curing agent (Sylgard 184 silicone elastomer kit) was poured onto it and cured in an oven at 100 °C for 1 hour. The polymerized PDMS was then peeled off, and inlet/outlet ports were created using a disposable biopsy punch (Robbins Instruments Inc.). To bind the PDMS with the devices containing the microelectrodes, both were exposed to oxygen plasma for around 45 s using a reactive-ion etching machine (Trion Technology, Inc.) Subsequently, the PDMS and the glass devices were carefully aligned, brought into contact, and baked on a hotplate at 150 °C for 1 hour while a standard calibration weight of 1 kg was applied uniformly on top. Finally, 21G stainless steel connectors were inserted into the inlet/outlet ports in the PDMS and connected to PTFE tubing (Elveflow Microfluidics).

4.2.3 Cell and spore production

S. sclerotiorum ascospores were produced as described in Chapter 1. HEK-293 cells were cultured from frozen stock at 37°C in high glucose Dulbecco's Modified Eagle Medium with L-glutamine and Phenol indicator (DMEM, high glucose; Gibco) supplemented with 10%(v/v) fetal bovine serum (FBS; SIGMA).[13] The cell line was split once its confluency on a 10 cm culture dish reached ~90 %, routinely twice a week. Before each experiment, cells were detached from the culture dish by incubation in 0.05% trypsin-EDTA at 37°C for 5 min and then resuspended in 5 mL culture

---

[13] I would like to thank Zuyuan Tian for culturing HEK cells that were employed in experiments. He was always available to provide me with cells, whenever I need them.

media. Subsequently, 1 mL of cell suspension was transferred to a centrifuge tube and centrifugated at 1000 rpm for 5 min, followed by the replacement of culture media with our low conductivity DEP buffers.

4.2.4   DEP buffer

Cells and ascospores were resuspended in a DEP buffer, with two different conductivities. DEPB1 (10 mM HEPES, 3 mM NaOH, 285 mM sucrose, and 1.5 mM $MgCl_2$) with a measured conductivity of 370 µS/cm. DEPB2 was obtained by diluting DEPB1 (1:8) with DI water and with a measured conductivity of 50 uS/cm. The conductivity of our buffers was measured with a conductivity meter (Oakton CON 6+) before each experiment. Low conductivity buffers reduce Joule heating and facilitates DEP trapping of ascospores and cells.

4.2.5   Instrumentation and experimental setup

The employed instrumentation and experimental setup are the same as described in chapter 3. The chip-holder presented in chapter 3 was slightly modified to fit the microfluidic device described in this chapter.

4.2.6   TEM methods

To obtain TEM images, ascospores were first chemically fixated with 2.5% glutaraldehyde and 2% paraformaldehyde in 0.1 M phosphate buffer (pH 7.2 – 7.4) and left overnight. Subsequently, spores were dehydrated with graded concentrations of ethanol (50%, 70%, 90%, 100%) in 15 min intervals for each concentration. After this, ascospores were washed with propylene oxide for 20 min and then infiltrated and embedded in pure spurr resin overnight and cured at 70 °C. Sections

of 70 nm to 90 nm thickness were obtained using an ultramicrotome Reichert-Jung Ultracut E. The sections were then stained with uranyl acetate and lead citrate stain. Images were acquired with a transmission electron microscope Morgagni 268 (Philips / FEI).[14]

4.3   Experimental Results and Discussion

4.3.1   Dielectric properties of HEK-293 cells

I first performed experiments with HEK-293 cells in order to validate the methodology. The reason for this is that the dielectric properties of this cell line are well know in the literature. Prior to loading cells into the device, and to remove air bubbles from the microchannel, our device was primed using ethanol, which was injected at a flowrate of 5 μL/min for 10 min. Subsequently, our buffer DEPB1 was slowly pumped into the microchannel at a flowrate of 0.3 μL/min for another 10 min. After this, HEK-293 cells resuspended in DEPB1 at a concentration of about 6.1×10^4 cells/mL were introduced into the microchannel at the same flowrate. To determine the minimum DEP trapping voltages, a high amplitude signal was initially applied to capture flowing cells. Once a cell was captured, the amplitude of the signal was slowly and carefully decreased in steps of 1V until the cell was released. Thus, the minimum DEP trapping voltage was recorded as the voltage 1 V above the signal that released the cell. For the voltage levels used during trapping, no observable morphological changes were detected in cells.

The minimum DEP trapping voltages were recorded over a wide range of frequencies, from 10 kHz to 20 MHz, and five measurements per frequency were performed to account for cell size variability. The same process was also repeated for cells resuspended in our buffer DEPB2 with a

---

[14] I would like to thank Dr. Oleksandra Savchenko and Dr. Kacie Norton for preparing ascospores for TEM imaging. Without their help, TEM imaging wouldn't have been possible. Dr. Kacie Norton also operated the TEM microscope.

measured concentration of around 6.2×10^4 cells/mL. Three independent experiments were performed for each buffer. Figure 4.2a shows the curves obtained during one experiment.

The lower boundary of the frequency range was chosen to avoid interference from electrode polarization effects while the upper boundary was limited by our signal generator. With the measured voltages, and using equation (4.4), the spectrum of the real part of the CM factor for each buffer can be calculated. Figure 4.2b shows the experimental spectrum of the CM factor obtained for each buffer using the measured voltages and equation (4.4). The parameters used in the calculations are shown in Table 4.1.
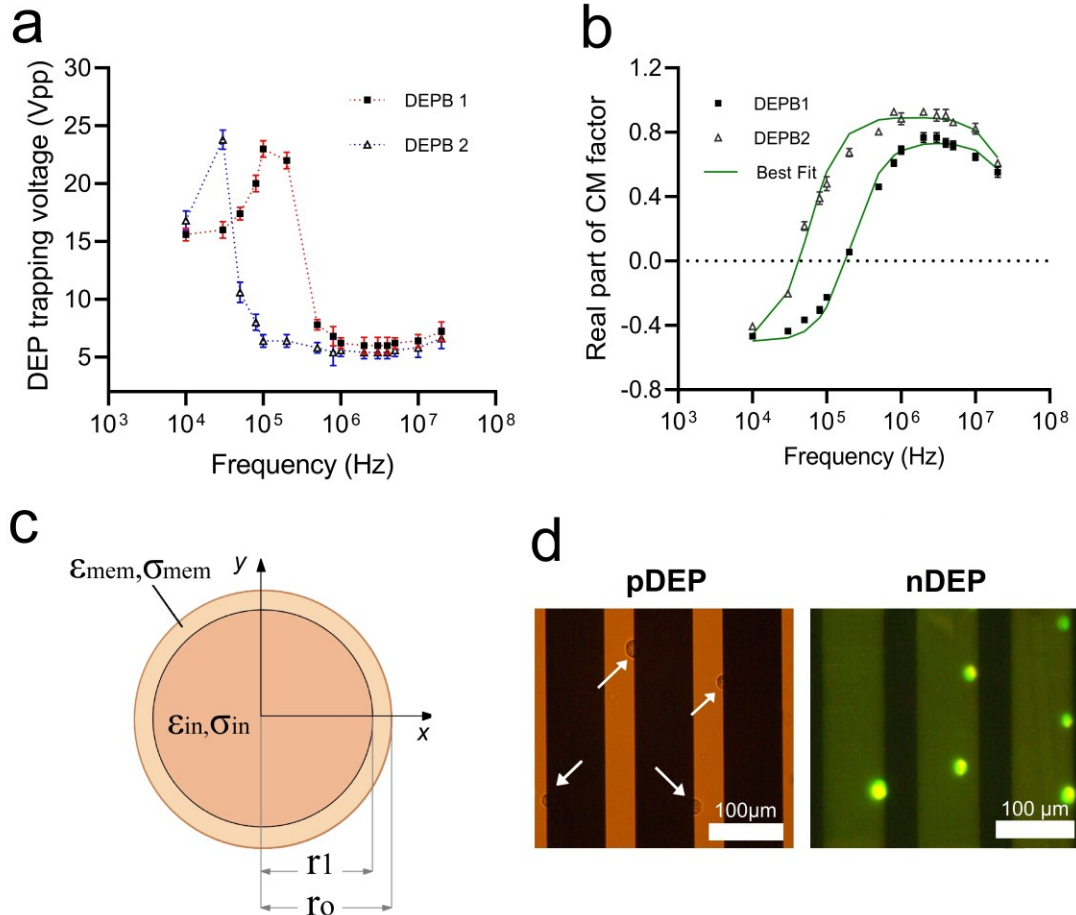
Figure 4.2: Dielectric characterization of HEK-293 cells. (a) Minimum DEP trapping voltages (peak-to-peak) from 10 kHz to 20 MHz for cells resuspended in two different medium conductivities, DEPB1 ($\sim$ 370 μS·cm^{-1}) and DEPB2 ($\sim$ 50 μS·cm^{-1}). Each point represents the average of five measurements (N=5). Error bars represent the standard deviation. (b) Experimental spectrum of the real part of the Clausius-Mossotti factor for HEK-293 cells (N=3). Error bars represent the standard deviation. (c) Single-shell model used. The radius of HEK-293 cells was measured to be 7 μm on average and the membrane thickness was set to 7 nm. (d) Microscopic images of HEK-293 cells captured under pDEP and nDEP. Under pDEP cells were captured at the edges of microelectrodes and under nDEP cells were captured at the top of the microchannel. Cells were stained to facilitate imaging of nDEP capture.

Parameter	Description	Value
k	Wall correction factor	2.0
η	Fluid viscosity	1×10^{-3} Pa $\cdot$ s
v_f	Local flow velocity	3.79×10^{-4} m/s
ε_m	Relative medium permittivity	78
ε_o	Vacuum permittivity	8.85×10^{-12} F/m
r_o	Cell's radius	7 μm
$\left.\dfrac{\partial \lvert E\rvert^2_{V=1}}{\partial x}\right\rvert_{y=7\mu m}$	Gradient of electric field	2.0×10^{13} V^2/m^3
$\left.\dfrac{\partial \lvert E\rvert^2_{V=1}}{\partial x}\right\rvert_{y=13\mu m}$	Gradient of electric field	4.8×10^{12} V^2/m^3

Table 4.1: Parameters employed for calculations of the real part of the CM factor for HEK-293 cells. The wall correction factor, flow velocity and gradient values were obtained from COMSOL. Fluid was assumed to be mainly water with a permittivity of 78 and viscosity value was obtained from [136].

In order to obtain the dielectric properties from the CM spectrum, cells were modeled using a spherical single-shell model, which is shown in Figure 4.2c, which has an effective complex permittivity given by [114], [115],

$$\varepsilon^*_{eff} = \varepsilon^*_{mem} \left[\frac{\left(\dfrac{r_o}{r_1}\right)^3 + 2\dfrac{\varepsilon^*_{cyt} - \varepsilon^*_{mem}}{\varepsilon^*_{cyt} + 2\varepsilon^*_{mem}}}{\left(\dfrac{r_o}{r_1}\right)^3 - \dfrac{\varepsilon^*_{cyt} - \varepsilon^*_{mem}}{\varepsilon^*_{cyt} + 2\varepsilon^*_{mem}}} \right] \tag{4.5}$$

where r_o is the radius of the cell, $r_1 = r_o - t$, where t is the thickness of the cell's membrane, and ε^*_{cyt} and ε^*_{mem} are the complex permittivities of the cell interior and membrane, respectively. The cell radius of our HEK-293 cell population was determined microscopically while the value of the membrane thickness, equal to 7 nm, was obtained from published reports [121]. By replacing ε^*_p in equation (4.4) with the effective permittivity ε^*_{eff} from equation (4.5), the dielectric properties

of HEK-293 cells can be estimated by fitting the experimental CM factor spectrum, shown in Figure 4.2b. Data fitting was performed using the nonlinear least square method, implemented with built-in Matlab 2015b functions (MathWorks). As the conductivity of the medium increases, the value of the first cross-over frequency (transition from nDEP to pDEP) is shifted to the right (Figure 4.2b), from 39.1 kHz to 174.4 kHz, based on the best fit analysis. Cells normally present two cross-over frequencies, however the second one (transition from pDEP to nDEP) falls outside of the range of our signal generator. Figure 4.2b also indicates that the values for the real part of the CM factor decrease as the conductivity of the buffer increases, requiring higher voltage amplitudes to trap cells (Figure 4.2a). Microscopic images of HEK-293 cells trapped by pDEP at the edges of the IME and by nDEP at the top of the microchannel are shown in Figure 4.2d. Cells were stained to facilitate imaging under nDEP.

The values of the four dielectric properties obtained experimentally with each buffer, DEPB1 and DEPB2, are shown in Table 4.2. These results agree well with those reported by other researchers [137], [138].

Reference	Buffer	ε_{cyt}	σ_{cyt} (S/m)	ε_{mem}	σ_{mem} (µS/m)
This thesis	DEPB1	89.98 ± 0.57	$0.40 \pm 1.95 \times 10^{-10}$	5.04 ± 0.03	$0.99 \pm 1.0 \times 10^{-5}$
This thesis	DEPB2	88.38 ± 1.06	$0.41 \pm 3.74 \times 10^{-10}$	2.90 ± 0.11	$0.58 \pm 4.1 \times 10^{-2}$
[138]	-	85 ± 4	$0.47 \pm 19 \times 10^{-3}$	6.28 ± 0.3	~ 0
[137]	-	60	0.5	9.5	~ 0

Table 4.2: Dielectric properties of HEK-293 cells obtained experimentally. Values represent the average of three independent experiments.

As expected, the permittivity (ε_{cyt}) and conductivity (σ_{cyt}) of the cell's interior remain unchanged regardless of the conductivity of the buffer, since there is no ion exchange between the interior of the cell and the buffer. These parameters influence the CM spectrum at higher

frequencies, whereas the lower frequency range of the CM spectrum is mainly affected by the dielectric properties of the plasma membrane, a lipid bilayer with low ionic permeability regarded as an insulator. As such, the conductivity values (σ_{mem}) obtained for both buffers were very low, as expected. Both, the permittivity (ε_{mem}) and conductivity (σ_{mem}) of the membrane increased slightly with the increase of buffer conductivity. A higher ionic strength induces an increase in the surface charge at the cell's membrane, which increases the surface capacitance and conductance. This effect can explain the variation in the permittivity and conductivity, which was also observed by other groups [139], [140]. These results validate the analysis and methodology as the estimated dielectric properties lie within values previously reported in the literature.

4.3.2   Dielectric properties of ascospores

After validating the device and methodology with HEK-293 cells, I proceeded to perform experiments with *S. sclerotiorum* ascospores. The process of ascospore loading into the microfluidic device was performed in the same manner as in the experiments with cells.

The measured trapping voltages for ascospores re-suspended in both buffers, DEPB1 and DEPB2, are shown in Figure 4.3a. The ascospore concentration on both buffers was measured to be around 7.2×10^4 ascospores/mL. Different from the previous experiment, the flowrate for ascospores in DEPB1 was set to 0.2 µL/min and 0.5 µL/min for DEPB2. The flow rate was reduced to 0.2 µL/min with DEPB1 to limit the amplitude of the applied voltage, as higher voltages (~ 40 Vpp) damaged the IME at low frequencies.
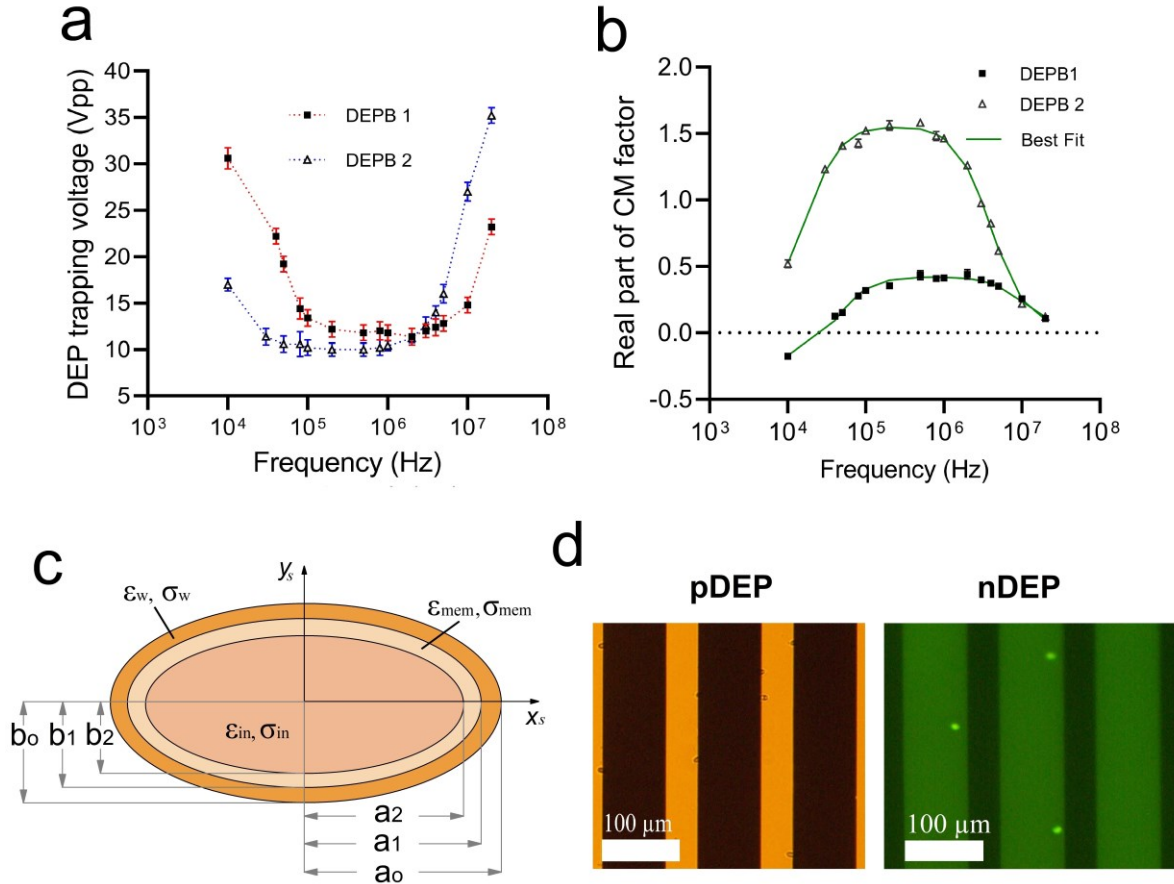
Figure 4.3: Dielectric characterization of *S. sclerotiorum* ascospores. (a) Minimum DEP trapping voltages (peak-to-peak) from 10 kHz to 20 MHz for ascospores resuspended in two different medium conductivities, DPB1 ($\sim$ 370 μS·cm^{-1}) and DPB2 ($\sim$ 50 μS·cm^{-1}). Each point represents the average of five measurements (N=5). Error bars represent the standard deviation. (b) Experimental spectrum of the real part of the Clausius-Mossotti factor for ascospores (N=3). Error bars represent the standard deviation. (c) Ellipsoidal double-shell model used. Semi-axes a_o and b_o=c_o were measured to be on average, 7 μm and 3 μm, respectively. (d) Microscopic images of ascospores captured under pDEP at the edges of microelectrodes and by nDEP at the top of the microchannel. Ascospores were stained to facilitate imaging of nDEP trapping.

An ellipsoidal double-shell model [118], as shown in Figure 4.3c, was employed to analyze the dielectric properties of *S. sclerotiorum* ascospores, as this model more accurately represents

their real shape [10], [21]. The ascospore is assumed to be an ellipsoid, with two concentric shells referred to as the membrane and the ascospore wall. Therefore, there are in total 6 dielectric parameters to be determined, as shown in Figure 4.3c. The semi-axes, a_o and b_o are 7 μm and 3 μm, respectively. These are the average values obtained by observations under the microscope of our spore population. The third semi-axes, c_o was set to be equal to b_o (prolate spheroid). As there are no published reports with values for the membrane and the ascospore wall thickness, TEM images were performed to estimate these values. The average thickness for the ascospore wall was found to be 150 nm, while the membrane thickness was measured to be around 8 nm on average. Figure 4.4 shows TEM images of a sectioned ascospore. TEM images were performed only to obtain an estimation of the thickness of the two outermost layers surrounding ascospores and not to study their internal composition or their physiology.
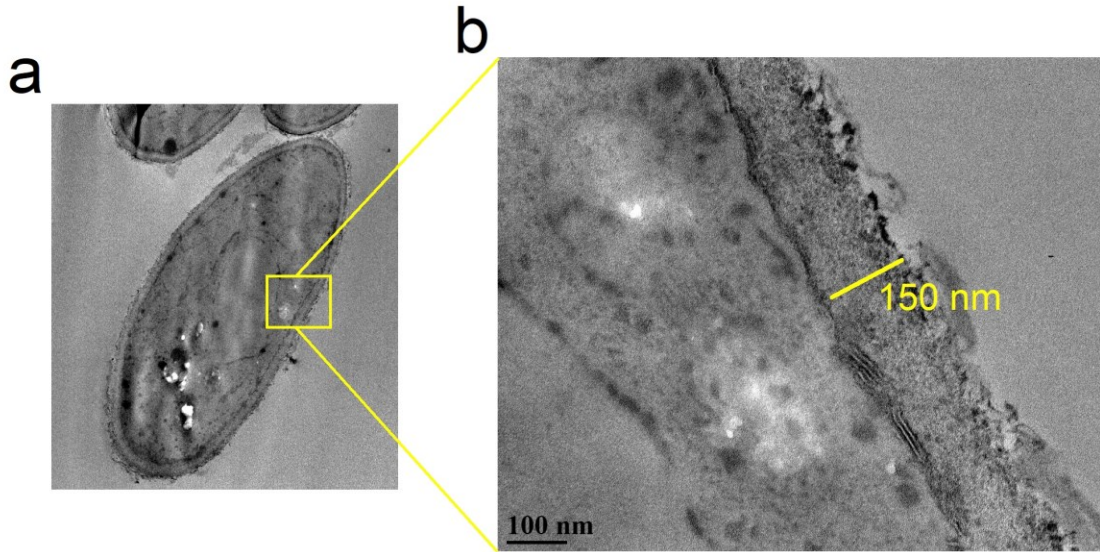
Figure 4.4: TEM images of sectioned spores. Sample thickness were between 80nm and 90 nm. A spore wall was identified during TEM imaging with an average value of 150nm. A second layer was observed (spore membrane) with a much smaller thickness value and equal to 8 nm.

The CM factor equation for an ellipsoid is also different from that of spheres, and is given by [118], [141],

$$CM = \frac{1}{3} \frac{\varepsilon_p^* - \varepsilon_m^*}{\varepsilon_m^* + A_0(\varepsilon_p^* - \varepsilon_m^*)} \tag{4.6}$$

and according to the concentric multi-shell theory, the effective complex permittivity for the ellipsoidal double-shell model is [118],

$$\varepsilon_{eff}^* = \varepsilon_w^* \left[\frac{\varepsilon_w^* + (\varepsilon_2^* - \varepsilon_w^*)A_1 + \alpha(\varepsilon_2^* - \varepsilon_w^*)(1 - A_0)}{\varepsilon_w^* + (\varepsilon_2^* - \varepsilon_w^*)A_1 - \alpha(\varepsilon_2^* - \varepsilon_w^*)A_0} \right] \tag{4.7}$$

with ε_2^* is given by,

$$\varepsilon_2^* = \varepsilon_{mem}^* \left[\frac{\varepsilon_{mem}^* + (\varepsilon_{in}^* - \varepsilon_{mem}^*)A_2 + \beta(\varepsilon_{in}^* - \varepsilon_{mem}^*)(1 - A_1)}{\varepsilon_{mem}^* + (\varepsilon_{in}^* - \varepsilon_{mem}^*)A_2 - \beta(\varepsilon_{in}^* - \varepsilon_{mem}^*)A_1} \right] \qquad (4.8)$$

with,

$$\alpha = \frac{a_1 b_1 c_1}{a_0 b_0 c_0} \; ; \; \beta = \frac{a_2 b_2 c_2}{a_1 b_1 c_1} \qquad (4.9)$$

ε_w^*, ε_{mem}^*, and ε_{in}^* are the complex permittivities of the ascospore wall, membrane, and ascospore interior, respectively. $A_{0,1,2}$ are the depolarization factors along the horizontal direction and are defined by,

$$A_i = \frac{a_i b_i c_i}{2} \int_0^\infty \frac{ds}{(s + a_i)\sqrt{(s + a_i^2)(s + b_i^2)(s + c_i^2)}} \; ; \quad i = 0,1,2 \qquad (4.10)$$

where s is an arbitrary distance for integration. The depolarization factor has not got any direct physical meaning and depends mainly on the geometrical shape, reason for which is also typically known as geometrical factor [142]. With the equations defined above, the same process of numerical calculations employed in the experiments with cells can be used with ascospores. Thus, with the measured voltages shown in Figure 4.3a, and using equation (4.4), the spectrum of the real part of the CM factor for each buffer can be calculated. The CM spectrum for ascospores is shown in Figure 4.3b.

The parameters used in the calculations are shown in Table 4.3. For the sake of simplification, the value of the radius r, used in equation (4.4) is the radius of a sphere with an equivalent volume to that of an ellipsoidal ascospore. The height of the channel was also reduced to 15 μm for experiments with ascospores. We observed that for the applied frequencies of the electric field, ascospores are polarized and oriented horizontally, along the x-direction of the channel, in other words, the x_s and y_s axes (Figure 4.3c) of the ascospores are parallel to the x and y axes of the system (Figure 4.1c). Therefore, we reduced the channel height to limit the voltage required for trapping ascospores under n-DEP (top of the channel).

Parameter	Description	Value
k	Wall correction factor	1.9
η	Fluid viscosity	1×10^{-3} Pa· s
v_{f1}	Local flow velocity DEPB1	2.80×10^{-4} m/s
v_{f2}	Local flow velocity DEPB2	7.02×10^{-4} m/s
ε_m	Relative medium permittivity	78
ε_o	Vacuum permittivity	8.85×10^{-12} F/m
r	Equivalent radius	3.9 μm
$\left.\dfrac{\partial |E|^2_{V=1}}{\partial x}\right|_{y=3\mu m}$	Gradient of electric field	2.7×10^{13} V^2/m^3
$\left.\dfrac{\partial |E|^2_{V=1}}{\partial x}\right|_{y=12\mu m}$	Gradient of electric field	9.0×10^{12} V^2/m^3

Table 4.3: Parameters employed for calculations of the real part of the CM factor for *S. sclerotiorum* ascospores. The wall correction factor, flow velocity and gradient values were obtained from COMSOL. Fluid was assumed to be mainly water with a permittivity of 78 and viscosity value was obtained from [136].

As expected, the spectrum of the real part of the CM factor indicates an observable conductivity dependence on the DEP response of ascospores. When employing DEPB2, no nDEP response within the applied frequency range was observed, although the trend of the best fit curve seems to indicate a cross-over frequency way below 10 kHz (Figure 4.3b). Trapping at frequencies

lower than 10 kHz was found to be unstable, reason for which we did not consider this region in our calculations. At a higher buffer conductivity (DEPB1), nDEP response of ascospores was observed and the cross-over frequency was found to be at 28.4 kHz based on the best fit curve. Microscopic images of ascospores captured with nDEP and pDEP are shown in Figure 4.3d. The DEP response of ascospores agrees well with the empirical results obtained in previous chapters.

To estimate the dielectric properties, the experimental CM factor was fit to equation (4.6), in which ε_p^* was replaced by the effective permittivity ε_{eff}^* from equation (4.7). The dielectric properties are summarized in Table 4.4.

Buffer	ε_{cyt}	σ_{cyt} (S/m)	ε_{mem}	σ_{mem}(μS/m)	ε_w	σ_w (S/m)
DEPB1	85.96 ± 0.64	0.0990 ± 0.0022	31.86 ± 1.10	7.13 ± 1.60	99.99 ± 1.38	0.080 ± 0.019
DEPB2	86.19 ± 0.52	0.0970 ± 0.0003	31.79 ± 1.00	7.50 ± 2.30	99.99 ± 8.66	0.010 ± 0.003

Table 4.4: Dielectric properties of *S. sclerotiorum* ascospores obtained experimentally. Values represent the average of three independent experiments.

The conductivity and permittivity of the ascospore interior was found to be insensitive to the conductivity of the external buffer, similar to what we obtained for HEK-293 cells. The same was obtained for the membrane, as this is surrounded by the ascospore wall. On the other hand, the conductivity of the ascospore wall increased slightly with the increase in medium conductivity, which can be attributed to the increase in the surface charge at the ascospore wall. This parameter mainly influences the CM spectrum at low frequencies. The same trend was obtained by Asami et al., in which they analyzed the dielectric properties of *E. coli* bacteria using an ellipsoidal double-shell model [119]. On the other hand, the permittivity of the ascospore wall mainly influences the

CM factor spectrum at very high frequencies. Einolf et al. and Asami et al. suggested that the permittivity of the wall has no influence on the CM factor spectrum within the frequency range employed in our experiments [143], [119]. This suggest that to obtain a more accurate estimation of the wall permittivity, higher frequencies should be considered (> 50 MHz).

It is also important to point out that by employing the multi-shell theory, we are assuming homogeneous structures for both cells and ascospores. However, these structures are in reality, complex heterogeneous structures composed of proteins, organelles, and nuclei. Within the frequency range employed in our experiments, the multi-shell theory is a simplified approximation that explains the dielectric dispersion of biological cells due to interfacial polarization. This is the major polarization mechanism usually observed in biological cells and tissues at the examined frequencies [115].

As mentioned earlier, our primary goal is to determine or approximate the dielectric properties of ascospores so that their dielectrophoretic response for a medium of known conductivity can be estimated a priori, without having to run long iterative experiments. This can considerably accelerate the design of dielectrophoretic filters, especially when multiple species are to be filtered. In our experiments, we chose media of low conductivity as this is the standard in DEP filters. This is mainly due to the fact that media of low conductivity improves the dielectric contrast of the cells, spores, or any polarizable microparticles, with respect to the manipulation media [144]. As the conductivity of the medium increases, the CM spectrum decreases, and it becomes harder to capture particles.

4.4   Conclusions

In this chapter, we have experimentally estimated the dielectric properties of *Sclerotinia sclerotiorum* airborne ascospores. These parameters are of major importance for the development of SSR forecasting systems based on dielectrophoretic filters.

We have employed a standard AC electrokinetic method within a microfluidic platform to determine the dielectric parameters of these ascospores and at two different medium conductivities. Our microfluidic device was fabricated with interdigitated microelectrodes for the generation of non-uniform electric fields, which induced a dielectrophoretic force on ascospores flowing within our microchannels and under laminar flow. By measuring the minimum trapping voltages over a wide frequency range, the DEP response, and dielectric properties of *S. sclerotiorum* ascospores were determined. In addition, ascospores were modeled using a realistic double-shell model based on the multi-shell theory. We believe that our results can accelerate the design of DEP filters for SSR forecasting applications. Furthermore, and to the best of our knowledge, this is the first report on the analysis of the dielectric properties of *Sclerotinia sclerotium* airborne inoculum.

Chapter 5

Summary and Future Outlook

In this thesis, we explored the development of micromachined devices for the detection of *S. sclerotium* ascospores. As previously described, these devices are intended to be integrated with spore-trap samplers in the future, aiming at the development of an SSR forecasting system.

5.1   Accomplishment and contributions

One of the main objectives, as outlined in Chapter 1, was the development of a microdevice capable of detecting single *S. sclerotium* ascospores. In Chapter 2 we described the development of a proof-of-concept device based on the Coulter principle that was able to achieve the impedimetric quantification of single *S. sclerotium* ascospores. This chip required only two photomasks to be fabricated and it was integrated with a DEP filter implemented through interdigitated microelectrodes. The DEP filter allowed us to selectively separate target ascospores from *F. graminearum* spores*,* a fungal pathogen typically encountered in the prairie regions of Canada. The main accomplishment of the work described in Chapter 2 is related to the single-spore sensitivity that was achieved, for the first time, using well established label-free techniques.

Although proof-of-concept, we demonstrated the great potential of lab-on-chips for the development of an SSR forecasting system.

In Chapter 3 we tackled issues and drawbacks encountered with the Coulter counter design, such as clogged channels, low sensitivity, and a sealing mechanism that was not suitable for field operations. For this, a new chip based on an electroactive microwell array design was developed. Wider microchannels eliminated clogging events, while a static impedimetric sensing increased the sensitivity to single ascospores. Furthermore, the DEP filter was implemented with the same microelectrodes used for impedimetric sensing, and the mode of operation between impedance measurement and DEP was controlled using switches in a custom-made chip-holder. Although the same principles were employed (DEP and impedimetric sensing), the devices described in Chapter 3 are six times more sensitive and have a more robust design compared to the Coulter approach, which are desired characteristics for field applications. In addition, we developed an enlarged version of this device (from 190 to 10000 microwells) for an application in cell sorting. The efficiency of this platform was demonstrated with a clinically relevant sample of cancer cells.

In Chapter 4 we described experiments for the dielectric characterization of S. *sclerotium* ascospores in the frequency range of 10 kHz to 20 MHz. The main goal of these experiments was not to study the interaction of AC electric fields and ascospores at a molecular level, but rather to obtain an estimation of the dielectric properties of the ascospores. Knowledge about the dielectric properties of target ascospores can accelerate the tunning process of DEP filters by simply plotting curves of the CM factor and for any given medium, without having to perform lengthy iterative experiments to determine the DEP response. The obtained dielectric properties yielded a DEP response (based on CM factor curves) that are in good agreement with previously observed

behavior. To the best of our knowledge, this represents the first report on the dielectric properties of this spore species.

5.2 Considerations on selectivity

F. graminearum spores (macroconidia) were employed as contaminants in all the experiments described in this thesis, and the effective dielectrophoretic separation between this species and the target ascospores (*S. sclerotiorum*) was demonstrated during experiments. Under field operation, spore-trap samplers are likely to collect different types of particles such as pollen grains, dust particles and other species of spores. Large particles, say greater than 20 μm, can be filtered out with conventional membrane filters before the sample (from the trap) is pumped to our microfluidic devices. In this case, the remaining particles will be closer in size to the target ascospores.

The selectivity on a dielectrophoretic filter arises primarily from the dielectric properties of the particles one wish to separate. This is because the DEP force depends on the dielectric properties of the particle on which the force is induced. Different species of cells or spores have different dielectric properties, which provide the basis for selective discrimination. In practical terms, the difference in dielectric properties will be translated into the frequency of the applied electric field that yields different DEP responses for different particles in the sample. In simpler words, it is necessary to find the frequency at which two or more species in the sample present different types of DEP force (pDEP and nDEP) or different levels of the same DEP force. When there is not a single frequency that can separate more than two different particles (at the same time), our DEP filters can be cascaded as shown schematically in Figure 5.1. This allows the application of different frequencies for each DEP filter, allowing the discrimination of a desired

type of particle. Future field testing will provide valuable information about common particles that are sampled by commercial traps, which will further improve our DEP filtering strategy within microfluidic devices.
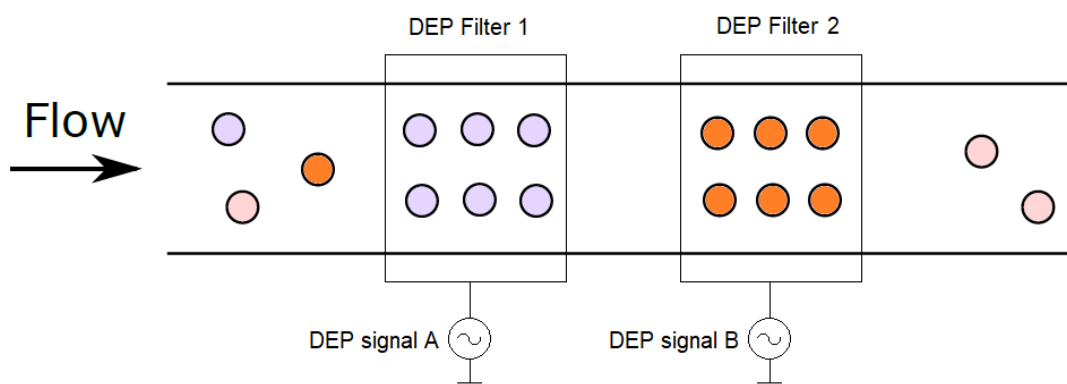
Figure 5.1. Schematic representation. DEP filters can be cascaded to allow the separation of more than two particles.

5.3 Future work

Future work in our Lab will focus on two main aspects: Device integration and hardware development. Although there are a variety of spore-trap samplers commercially available, work in our Lab will focus on the sampler marketed as *cyclone,* by Burkard Manufacturing. Figure 5.2a shows this sampler installed in the field by collaborators from the Lethbridge Research and Development Centre, while Figure 5.2b shows the *cyclone* sampler installed in our Lab for integration tests with our chips. The sampler has an air throughput of 16.5 L/min and can collect

airborne particles directly into a 1.5 mL Eppendorf vial. Our goal is to pump the collection solution from the vial, in a controlled manner, to our microfluidic devices.[15]
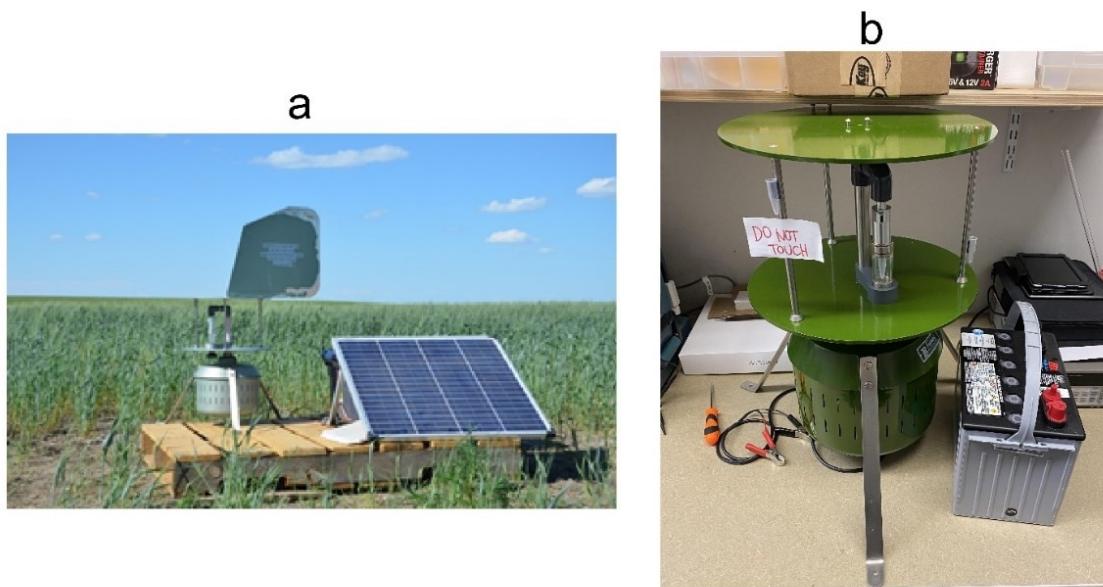
Figure 5.2: (a) Spore-trap sampler "cyclone" installed in the field by collaborators. Photograph courtesy of Dr. André Laroche from the Lethbridge Research and Development Centre. (b) Spore-trap sampler in the Binary Lab for integration testing with our microfluidic devices.

All the experiments described in previous chapters were performed with the help of benchtop equipment (signal generator, impedance analyzer, amplifiers). However, it is desirable to develop portable equipment that can facilitate future field or greenhouse testing. Thus, three main hardware components are needed, a DEP board for the generation of the DEP signal, an impedance board for impedimetric measurements, and finally a switching board, which will switch between modes of operation, that is, between measuring the impedance and applying the DEP signal. Ultimately, these three components can be combined in a unique PCB. The development of these portable equipment has already started. The first generation of the DEP board that is being developed in

---

[15] I would like to thank Meng Xiao and Yiwei Feng who are currently working and testing the integration between the microfluidic devices I developed and the spore-trap sampler.

our lab is shown in Figure 5.3. The board was designed to provide sinusoidal voltages of up to 32

Vpp with a frequency range between 1kHz and 1MHz. The output signal is simply generated using

a DDS (Direct Digital Synthesizer) generator, controlled by a microcontroller (ATmega328). The

DDS output is then amplified employing a two-stage amplifier implemented through op-amps.[16]
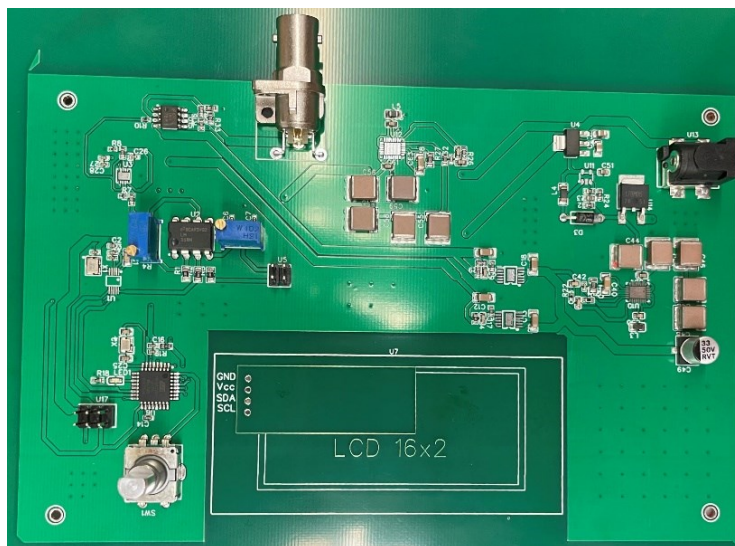
Figure 5.3: DEP board in construction. Photograph courtesy of Tianxiang Jiang.

Work on the switching board has also started. Figure 5.4 shows the first generation of the

switching board. The circuit design employs five 8-bit shift registers than can control 40 analog

outputs, 20 for the DEP signal and 20 for impedance measurements (there are 20 pads in our

microfluidic device). Switches were implemented with common SPST integrated circuits, and the

logic was controlled with the ATmega328 microcontroller.[17]

---

[16] I would like to thank Tianxiang Jiang who is currently working with the development of the DEP board. While the initial design specifications and amplification strategy were mine, Tianxiang has perfected them, handling the PCB layout, component selection, simulation and soldering.
[17] I would like to thank Riley Stuermer for developing the switching board. We worked together to design the circuitry and specifications, but was Riley who handled the PCB layout, component selection, simulation, and soldering.
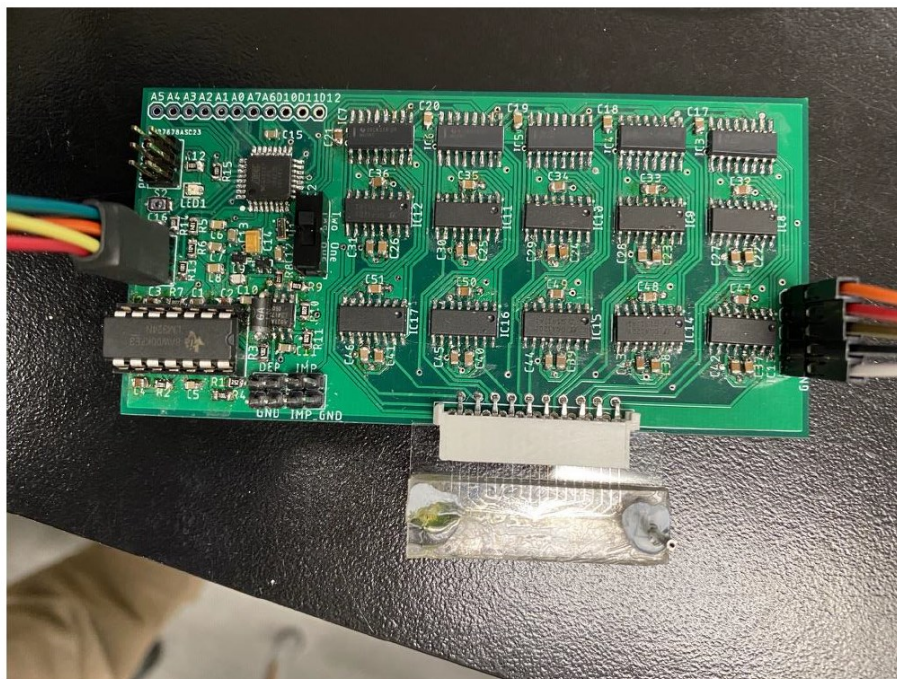
Figure 5.4: Switching board in construction for future field testing.

An impedance board is also being developed by the "circuit design" team of our research group, which will not only support this project but many others within our Lab. Future work will focus on testing and validating the three electronic boards and finally combining them into one. Naturally, field testing with the whole system is also part of the future work. This step will require the help of collaborators with expertise in crop protection as well as plant pathologists. Field testing will provide valuable feedback to further improve the design of our microfluidic devices as well as the design of the PCBs.

References

[1]   L. H. Purdy, "*Sclerotinia sclerotiorum*: History, Diseases and Symptomatology, Host Range, Geographic Distribution, and Impact," *Phytopathology*, vol. 69, no. 8, pp. 875–880, 1979.

[2]   E. Twengström, R. Sigvald, C. Svensson, and J. Yuen, "Forecasting *Sclerotinia* stem rot in spring sown oilseed rape," *Crop Protection*, vol. 17, no. 5, pp. 405–411, 1998, doi: 10.1016/S0261-2194(98)00035-0.

[3]   R. N. Attanayake, P. A. Carter, D. Jiang, L. Del Río-Mendoza, and W. Chen, "*Sclerotinia sclerotiorum* populations infecting canola from China and the United States are genetically and phenotypically distinct," *Phytopathology*, vol. 103, no. 7, pp. 750–761, 2013, doi: 10.1094/PHYTO-07-12-0159-R.

[4]   Food and Agriculture Organization of the United Nations, "Production of Rapeseed: top 10 producers," 2018. http://www.fao.org/faostat/en/#data/QC/visualize

[5]   LMC International, "The Economic Impact of Canola on the Canadian Economy," 2016. https://www.canolacouncil.org/media/584356/lmc_canola_10-year_impact_study_-_canada_final_dec_2016.pdf

[6]   "Canola Council of Canada," 2018. https://www.canolacouncil.org/markets-stats/statistics/tonnes/

[7]   L. E. del Rio *et al.*, "Impact of *Sclerotinia* Stem Rot on Yield of Canola.," *Plant Disease*, vol. 91, no. 2, pp. 191–194, Feb. 2007.

[8]   G. J. Boland and R. Hall, "Index of plant hosts of *Sclerotinia sclerotiorum*," *Canadian Journal of Plant Pathology*, vol. 16, no. 2, pp. 93–100, 1994.

[9]   A A Bell and M. H. Wheeler, "Biosynthesis and Functions of Fungal Melanins," *Annual Review of Phytopathology*, vol. 24, no. 1, pp. 411–451, Nov. 1986, doi: 10.1146/ANNUREV.PY.24.090186.002211.

[10]   M. D. Bolton, B. P. H. J. Thomma, and B. D. Nelson, "*Sclerotinia sclerotiorum* (Lib .) de Bary : biology and molecular traits," *Molecular Plant Pathology*, vol. 7, no. 1, pp. 1–16, 2006, doi: 10.1111/J.1364-3703.2005.00316.X.

[11]   G. S. Abawi and R. G. Grogan, "Source of primary inoculum and effects of temperature and moisture on infection of beans by *Whetzelinia sclerotiorum*.," *Phytopathology*, vol. 65, pp. 300–309, 1975.

[12]   P. B. Adams and W. A. Ayers, "Ecology of *Sclerotinia* Species," *Phytopathology*, vol. 69, pp. 896–899, 1979, doi: 10.1094/phyto-69-896.

[13]   H. F. Schwartz, "Factors Affecting Sclerotium Populations of, and Apothecium Production by, *Sclerotinia sclerotiorum*," *Phytopathology*, vol. 68, no. 3, p. 383, 1978, doi: 10.1094/phyto-68-383.

[14]   J. R., Williams and Stelfox. D., "Dispersal of ascospores of *Sclerotinia sclerotiorum* in relation to Sclerotinia stem rot of rapeseed.," *Plant Dis. Rep.*, vol. 3, pp. 395–399, 1979.

[15]   D. Stelfox, J. R. Williams, U. Soehngen, and R. C. Topping, "Transport of *Sclerotinia sclerotiorum* ascospores by rapeseed pollen in Alberta.," *Plant Dis. Rep*, vol. 62, no. 7, pp. 576–579, 1978.

[16] G.S. Abawi and R.G. Grogan, "Epidemiology of diseases caused by *Sclerotinia* species," *Phytopathology*, vol. 69, pp. 899–904, 1979.

[17] Canola council of Canada, "Canola Encyclopedia." https://www.canolacouncil.org/canola-encyclopedia/diseases/sclerotinia-stem-rot/ (accessed May 17, 2022).

[18] R. K. Gugel, "Inoculum-disease relationships in *sclerotinia* stem rot of rapeseed in Saskatchewan," *Canadian Journal of Plant Pathology*, vol. 8, no. 1, pp. 89–96, 1986, doi: 10.1080/07060668609501848.

[19] J. R. Williams and D. Stelfox, "Influence of farming practices in Alberta on germination and apothecium production of sclerotia of *sclerotinia sclerotiorum*," *Canadian Journal of Plant Pathology*, vol. 2, no. 3, pp. 169–172, 1980, doi: 10.1080/07060668009501435.

[20] B. R. Ziesman, "Development and validation of a *sclerotinia sclerotiorum*-specific quantitative PCR assay to assess risk of *sclerotinia* Stem Rot of Canola (*Brassica napus*)," PhD Thesis, University of Alberta, Edmonton, 2016.

[21] L. C. T. Shoute *et al.*, "Immuno-impedimetric Biosensor for Onsite Monitoring of Ascospores and Forecasting of *Sclerotinia* Stem Rot of Canola," *Scientific Reports*, vol. 8, no. 1, pp. 1–9, 2018, doi: 10.1038/s41598-018-30167-5.

[22] H. R. Kutcher and T. M. Wolf, "Low-drift fungicide application technology for *sclerotinia* stem rot control in canola," *Crop Protection*, vol. 25, no. 7, pp. 640–646, Jul. 2006, doi: 10.1016/J.CROPRO.2005.09.003.

[23] B. D. Gossen, S. R. Rimmer, and J. D. Holley, "First Report of Resistance to Benomyl Fungicide in *Sclerotinia sclerotiorum*," *Plant Disease*, vol. 85, no. 11, pp. 1206–1206, 2001.

[24]   D. L. McLaren, R. L. Conner, H. R. Kutcher, R. G. Platford, J. L. Lamb, and H. A. Lamey, "Predicting diseases caused by *Sclerotinia sclerotiorum* on canola and bean — a western Canadian perspective," *Canadian Journal of Plant Pathology*, vol. 26, no. 4, pp. 489–497, 2004, doi: 10.1080/07060660409507169.

[25]   T. K. Turkington, H. R. Kutcher, D. Mclaren, and K. Y. Rashid, "Managing *Sclerotinia* in oilseed and pulse crops," *Prairie Soils & Crops Journal,* vol. 4, pp. 105–113, 2011.

[26]   M. Bom and G. J. Boland, "Evaluation of disease forecasting variables for *sclerotinia* stem rot (*Sclerotinia sclerotiorum*) of canola," *Canadian Journal of Plant Science*, vol. 80, no. 4, pp. 889–898, 2000, doi: 10.4141/P99-071.

[27]   P. Thomas, "*Sclerotinia* stem rot checklist," in *Canola growers manual. Winnipeg: Canola Council of Canada*, 1984, pp. 1053–1055.

[28]   D. Ahlers, "Integrated plant protection for fungus diseases in winter oilseed rape," *Gesunde Pflanzen,* vol - *41*, no. 9, p. 306, 1989.

[29]   J. P. Clarkson, L. Fawcett, S. G. Anthony, and C. Young, "A model for *sclerotinia sclerotiorum* infection and disease development in lettuce, based on the effects of temperature, relative humidity and ascospore density," *PLoS One*, vol. 9, no. 4, pp. 15–25, 2014, doi: 10.1371/journal.pone.0094049.

[30]   P. Sharma, P. D. Meena, A. Kumar, V. Kumar, and D. Singh, "Forewarning models for *Sclerotinia* rot (*Sclerotinia sclerotiorum*) in Indian mustard (*Brassica juncea* L.)," *Phytoparasitica*, vol. 43, no. 4, pp. 509–516, 2015, doi: 10.1007/s12600-015-0463-4.

[31]   North Dakota State University, "Estimated risk of *Sclerotinia* stem rot development." www.ag.ndsu.edu/sclerotinia/riskmap.html

[32]   R. Harikrishnan and L. E. del Río, "Influence of temperature, relative humidity, ascospore concentration, and length of drying of colonized dry bean flowers on white mold development," *Plant Disease*, vol. 90, no. 7, pp. 946–950, 2006, doi: 10.1094/PD-90-0946.

[33]   D. Bečka *et al.*, "Use of petal test in early-flowering varieties of oilseed rape (*Brassica napus* L.) for predicting the infection pressure of *Sclerotinia sclerotiorum* (Lib.) de Bary," *Crop Protection*, vol. 80, pp. 127–131, 2016, doi: 10.1016/j.cropro.2015.11.006.

[34]   T. K. Turkington, R. A. A. Morrall, and S. V. Rude, "Use of petal infestation to forecast *sclerotinia* stem rot of canola: The impact of diurnal and weather-related inoculum fluctuations," *Canadian Journal of Plant Pathology*, vol. 13, no. 4, pp. 347–355, 1991, doi: 10.1080/07060669109500920.

[35]   J. Dueck and R. Morrall, "Epidemiology of *sclerotinia* stem rot of rapeseed in Saskatchewan," *Canadian Journal of Plant Pathology*, vol. 4, pp. 161–168, 1982.

[36]   R. A. A. Morrall and J. Dueck, "*Sclerotinia* stem rot of spring rapeseed in Western Canada [*Sclerotinia sclerotiorum*]," in *Proc. 6th Int. Rapeseed Conf*, 1983, pp. 957–962.

[37]   M. Bom and G. J. Boland, "Evaluation of polyclonal-antibody-based immunoassays for detection of *Sclerotinia sclerotiorum* on canola petals, and prediction of stem rot," *Canadian Journal of Microbiology*, vol. 46, no. 8, pp. 723–729, 2000, doi: 10.1139/w00-054.

[38]   C. Almquist and A. C. Wallenhammar, "Monitoring of plant and airborne inoculum of *Sclerotinia sclerotiorum* in spring oilseed rape using real-time PCR," *Plant Pathology*, vol. 64, no. 1, pp. 109–118, 2015, doi: 10.1111/ppa.12230.

[39]   B. R. Ziesman, T. K. Turkington, and S. E. Strelkov, "A Quantitative PCR System for Measuring *Sclerotinia sclerotiorum* in Canola (*Brassica napus*)," *Plant Disease*, vol. 100, no. 5, pp. 984–990, 2016.

[40]   Y. Yanni, D. Laisong, L. Xin, Y. Jinghui, and M. Zhonghua, "Detection of *Sclerotinia sclerotiorum* in Planta by a Real-time PCR Assay," *Journal of Phytopathology*, vol. 469, pp. 465–469, 2009, doi: 10.1111/j.1439-0434.2009.01543.x.

[41]   B. S. Park *et al.*, "Continuous separation of fungal spores in a microfluidic flow focusing device," *Analyst*, vol. 144, no. 16, pp. 4962–4971, 2019, doi: 10.1039/c9an00905a.

[42]   M. L. Parker, M. R. McDonald, and G. J. Boland, "Evaluation of air sampling and detection methods to quantify airborne ascospores of *Sclerotinia sclerotiorum*," *Plant Disease*, vol. 98, no. 1, pp. 32–42, 2014, doi: 10.1094/PDIS-02-13-0163-RE.

[43]   M. Khater, A. de Escosura-muñiz, and A. Merkoçi, "Biosensors for plant pathogen detection," *Biosensors and Bioelectronics*, vol. 93, no. September 2016, pp. 72–86, 2017, doi: 10.1016/j.bios.2016.09.091.

[44]   U. Jarocka, M. Wąsowicz, H. Radecka, T. Malinowski, L. Michalczuk, and J. Radecki, "Impedimetric Immunosensor for Detection of *Plum Pox* Virus in Plant Extracts," *Electroanalysis*, vol. 23, no. 9, pp. 2197–2204, 2011, doi: 10.1002/elan.201100152.

114

[45]   A. Eun, Huang L, Chew FT, Li SF, and Wong SM, "Detection of two orchid viruses using quartz crystal microbalance (QCM) immunosensors," *J Virol Methods*, vol. 99, no. 1–2, pp. 71–79, 2002, doi: 10.1016/s0166-0934(01)00382-2.

[46]   A. S. Nezhad, "Future of portable devices for plant pathogen diagnosis," *Lab on a Chip*, vol. 14, no. 16, pp. 2887–2904, 2014, doi: 10.1039/c4lc00487f.

[47]   G. Papadakis, N. Skandalis, A. Dimopoulou, and P. Glynos, "Bacteria Murmur: Application of an Acoustic Biosensor for Plant Pathogen Detection," *PLoS ONE*, vol. 10, no. 7, p. e0132773, 2015, doi: 10.1371/journal.pone.0132773.

[48]   M. Regiart *et al.*, "Development of a nanostructured immunosensor for early and in situ detection of *Xanthomonas arboricola* in agricultural food production," *Talanta*, vol. 175, pp. 535–541, Dec. 2017, doi: 10.1016/J.TALANTA.2017.07.086.

[49]   Z. Cebula *et al.*, "Detection of the Plant Pathogen Pseudomonas *Syringae pv. Lachrymans* on Antibody-Modified Gold Electrodes by Electrochemical Impedance Spectroscopy," *Sensors 2019, Vol. 19, Page 5411*, vol. 19, no. 24, p. 5411, Dec. 2019, doi: 10.3390/S19245411.

[50]   M. K. Prasannakumar, P. B. Parivallal, D. Pramesh, H. B. Mahesh, and E. Raj, "LAMP-based foldable microdevice platform for the rapid detection of *Magnaporthe oryzae* and *Sarocladium oryzae* in rice seed," *Scientific Reports 2021 11:1*, vol. 11, no. 1, pp. 1–10, Jan. 2021, doi: 10.1038/s41598-020-80644-z.

[51]   D. Natsuhara *et al.*, "A Microfluidic Diagnostic Device Capable of Autonomous Sample Mixing and Dispensing for the Simultaneous Genetic Detection of Multiple Plant Viruses,"

Micromachines 2020, Vol. 11, Page 540, vol. 11, no. 6, p. 540, May 2020, doi: 10.3390/MI11060540.

[52]   H. Zhang and J. Wang, "Detection of age and insect damage incurred by wheat, with an electronic nose," *Journal of Stored Products Research*, vol. 43, no. 4, pp. 489–495, Jan. 2007, doi: 10.1016/J.JSPR.2007.01.004.

[53]   J. Laothawornkitkul *et al.*, "Discrimination of plant volatile signatures by an electronic nose: A potential technology for plant pest and disease monitoring," *Environmental Science and Technology*, vol. 42, no. 22, pp. 8433–8439, Nov. 2008, doi: 10.1021/ES801738S/SUPPL_FILE/ES801738S_SI_001.PDF.

[54]   J. Belasque, M. C. G. Gasparoto, and L. G. Marcassa, "Detection of mechanical and disease stresses in citrus plants by fluorescence spectroscopy," *Appl Opt*, vol. 47, no. 11, pp. 1922–1926, Apr. 2008, doi: 10.1364/AO.47.001922.

[55]   S. Lenk *et al.*, "Multispectral fluorescence and reflectance imaging at the leaf level and its possible applications," *Journal of Experimental Botany*, vol. 58, no. 4, pp. 807–814, Mar. 2007, doi: 10.1093/JXB/ERL207.

[56]   H. Zulhaidi, M. Shafri, M. Shafri, and N. Hamdan, "Hyperspectral Imagery for Mapping Disease Infection in Oil Palm Plantation Using Vegetation Indices and Red Edge Techniques," *American Journal of Applied Sciences*, vol. 6, no. 6, pp. 1031–1035, Jun. 2009, doi: 10.3844/AJASSP.2009.1031.1035.

[57]   B. Chen *et al.*, "Spectrum Characteristics of Cotton Canopy Infected with *Verticillium Wilt* and Inversion of Severity Level," *IFIP International Federation for Information Processing*, vol. 259, no. 2, pp. 1169–1180, 2008, doi: 10.1007/978-0-387-77253-0_51.

[58] W. Kong, C. Zhang, W. Huang, F. Liu, and Y. He, "Application of Hyperspectral Imaging to Detect *Sclerotinia sclerotiorum* on Oilseed Rape Stems," *Sensors 2018, Vol. 18, Page 123*, vol. 18, no. 1, p. 123, Jan. 2018, doi: 10.3390/S18010123.

[59] R. W. DeBlois and C. P. Bean, "Counting and sizing of submicron particles by the resistive pulse technique," *Review of Scientific Instruments*, vol. 41, no. 7, pp. 909–916, 1970, doi: 10.1063/1.1684724.

[60] W. Coulter, "High speed automatic blood cell counter and cell size analyzer," in *Proceedings of the National Electronics Conference*, 1956, pp. 1034–1042.

[61] K. Cheung, S. Gawad, and P. Renaud, "Impedance spectroscopy flow cytometry: On-chip label-free cell differentiation," *Cytometry Part A*, vol. 65, no. 2, pp. 124–132, 2005, doi: 10.1002/cyto.a.20141.

[62] S. Gawad, L. Schild, and P. Renaud, "Micromachined impedance spectroscopy flow cytometer for cell analysis and particle sizing," *Lab on a Chip*, vol. 1, no. 1, pp. 76–82, 2001, doi: 10.1039/b103933b.

[63] S. Gawad, K. Cheung, U. Seger, A. Bertsch, and P. Renaud, "Dielectric spectroscopy in a micromachined flow cytometer: Theoretical and practical considerations," *Lab on a Chip*, vol. 4, no. 3, pp. 241–251, 2004, doi: 10.1039/b313761a.

[64] C. Bernabini, D. Holmes, and H. Morgan, "Micro-impedance cytometry for detection and analysis of micron-sized particles and bacteria.," *Lab on a Chip - Miniaturisation for Chemistry & Biology*, vol. 11, no. 3, pp. 407–412, Feb. 2011.

[65] H. Choi *et al.*, "A flow cytometry-based submicron-sized bacterial detection system using a movable virtual wall.," *Lab on a Chip*, vol. 14, no. 13, pp. 2327–2333, Jul. 2014, doi: 10.1039/c4lc00238e.

[66] J. Chen *et al.*, "Classification of cell types using a microfluidic device for mechanical and electrical measurement on single cells.," *Lab on a Chip*, vol. 11, no. 18, pp. 3174–3181, Sep. 2011, doi: 10.1039/c1lc20473d.

[67] Y. Zheng, E. Shojaei-Baghini, A. Azad, C. Wang, and Y. Sun, "High-throughput biophysical measurement of human red blood cells.," *Lab on a Chip*, vol. 12, no. 14, pp. 2560–2567, Jul. 2012, doi: 10.1039/c2lc21210b.

[68] D. Holmes *et al.*, "Leukocyte analysis and differentiation using high speed microfluidic single cell impedance cytometry.," *Lab on a Chip*, vol. 9, no. 20, pp. 2881–2889, Oct. 2009, doi: 10.1039/b910053a.

[69] D. Holmos and H. Morgan, "Single Cell Impedance Cytometry for Identification and Counting of CD4 T-Cells in Human Blood Using Impedance Labels," *Analytical chemistry (Washington) vol. 82*, no. 4, p. 1455, 2010.

[70] H. A. Pohl and I. Hawk, "Separation of Living and Dead Cells by Dielectrophoresis," *Science (1979)*, vol. 152, no. 3722, pp. 647–649, 1966.

[71] M. Sun, P. Durkin, J. Li, T. L. Toth, and X. He, "Label-Free On-Chip Selective Extraction of Cell-Aggregate-Laden Microcapsules from Oil into Aqueous Solution with Optical Sensor and Dielectrophoresis," *ACS Sensors*, vol. 3, no. 2, pp. 410–417, 2018, doi: 10.1021/acssensors.7b00834.

[72] H. A. Pohl, "Some Effects of Nonuniform Fields on Dielectrics," *Journal of Applied Physics*, vol. 29, no. 8, pp. 1182–1188, Aug. 1958, doi: 10.1063/1.1723398.

[73] J. Voldman, "Electrical forces for microscale cell manipulation," *Annual Review of Biomedical Engineering*, vol. 8, pp. 425–454, 2006, doi: 10.1146/annurev.bioeng.8.061505.095739.

[74] R. Pethig., "Dielectrophoresis: Status of the theory, technology, and applications," *Biomicrofluidics*, vol. 4, no. 2, pp. 1–35, 2010, doi: 10.1063/1.3456626.

[75] M. Viefhues and R. Eichhorn, "DNA dielectrophoresis: Theory and applications a review," *Electrophoresis*, vol. 38, no. 11, pp. 1483–1506, 2017, doi: 10.1002/elps.201600482.

[76] T. B. Jones, *Electromechanics of Particles*. Cambridge: Cambridge University Press, 1995. doi: DOI: 10.1017/CBO9780511574498.

[77] Jones TB., "Basic theory of dielectrophoresis and electrorotation," *IEEE Eng Med Biol Mag*, vol. 22, no. 6, pp. 33–42, 2003.

[78] P. Gascoyne, J. Satayavivad, and M. Ruchirawat, "Microfluidic approaches to malaria detection," *Acta Tropica*, vol. 89, no. 3, pp. 357–369, 2004, doi: 10.1016/j.actatropica.2003.11.009.

[79] D. T. Bacheschi *et al.*, "Overcoming the sensitivity vs. throughput tradeoff in Coulter counters: A novel side counter design," *Biosensors and Bioelectronics*, vol. 168, Nov. 2020, doi: 10.1016/j.bios.2020.112507.

[80] P. ben Ishai, M. S. Talary, A. Caduff, E. Levy, and Y. Feldman, "Electrode polarization in dielectric measurements: A review," *Measurement Science and Technology*, vol. 24, no. 10, 2013, doi: 10.1088/0957-0233/24/10/102001.

[81] P. Dak and M. A. Alam, "Non-Faradaic Impedance Model of a Biochemical Sensor," pp. 1–14, 2015, doi: 10.4231/D3PR7MV7M.

[82] B. Brazey, J. Cottet, A. Bolopion, H. van Lintel, P. Renaud, and M. Gauthier, "Impedance-based real-time position sensor for lab-on-a-chip devices," *Lab on a Chip*, vol. 18, p. 818, 2018, doi: 10.1039/c7lc01344b.

[83] J. Cottet, A. Kehren, V. L. Harald, B. François, M. Frénéa-Robin, and P. Renaud, "How to improve the sensitivity of coplanar electrodes and micro channel design in electrical impedance flow cytometry: a study," *Microfuidics and Nanofluidics*, vol. 23, p. 11, 2019, doi: 10.1007/s10404-018-2178-6.

[84] M. D. Keller, G. C. Bergstrom, and E. J. Shields, "The aerobiology of *Fusarium graminearum*," *Aerobiologia (Bologna)*, vol. 30, no. 2, pp. 123–136, 2014, doi: 10.1007/s10453-013-9321-3.

[85] Z. Bai, Y. Deng, D. Kim, Z. Chen, Y. Xiao, and R. Fan, "An Integrated Dielectrophoresis-Trapping and Nanowell Transfer Approach to Enable Double-Sub-Poisson Single-Cell RNA Sequencing," *ACS Nano*, vol. 14, no. 6, pp. 7412–7424, 2020, doi: 10.1021/acsnano.0c02953.

[86] T. Man *et al.*, "Intracellular Photothermal Delivery for Suspension Cells Using Sharp Nanoscale Tips in Microwells," *ACS Nano*, vol. 13, no. 9, pp. 10835–10844, 2019, doi: 10.1021/acsnano.9b06025.

[87]   S. Bose *et al.*, "Scalable microfluidics for single-cell RNA printing and sequencing," *Genome Biology*, vol. 16, no. 1, pp. 1–16, 2015, doi: 10.1186/s13059-015-0684-3.

[88]   B. Dura *et al.*, "scFTD-seq: freeze-thaw lysis based, portable approach toward highly distributed single-cell 3' mRNA profiling," *Nucleic Acids Res*, vol. 47, no. 3, p. e16, 2019, doi: 10.1093/nar/gky1173.

[89]   N. J. Wittenberg *et al.*, "Facile assembly of micro- and nanoarrays for sensing with natural cell membranes," *ACS Nano*, vol. 5, no. 9, pp. 7555–7564, 2011, doi: 10.1021/nn202554t.

[90]   Y. Yoshimura, M. Tomita, F. Mizutani, and T. Yasukawa, "Cell pairing using microwell array electrodes based on dielectrophoresis," *Analytical Chemistry*, vol. 86, no. 14, pp. 6818–6822, 2014, doi: 10.1021/ac5015996.

[91]   C. Wu, R. Chen, Y. Liu, Z. Yu, Y. Jiang, and X. Cheng, "A planar dielectrophoresis-based chip for high-throughput cell pairing," *Lab on a Chip*, vol. 17, no. 23, pp. 4008–4014, 2017, doi: 10.1039/c7lc01082f.

[92]   M. Kobayashi, S. H. Kim, H. Nakamura, S. Kaneda, and T. Fujii, "Cancer cell analyses at the single cell-level using electroactive microwell array device," *PLoS ONE*, vol. 10, no. 11, pp. 1–10, 2015, doi: 10.1371/journal.pone.0139980.

[93]   Y. Yang, H. S. Rho, M. Stevens, A. G. J. Tibbe, H. Gardeniers, and L. W. M. M. Terstappen, "Microfluidic device for DNA amplification of single cancer cells isolated from whole blood by self-seeding microwells," *Lab on a Chip*, vol. 15, no. 22, pp. 4331–4337, 2015, doi: 10.1039/c5lc00816f.

[94] A. Morimoto *et al.*, "High-density dielectrophoretic microwell array for detection, capture, and single-cell analysis of rare tumor cells in peripheral blood," *PLoS ONE*, vol. 10, no. 6, pp. 1–19, 2015, doi: 10.1371/journal.pone.0130418.

[95] S. H. Kim and T. Fujii, "Efficient analysis of a small number of cancer cells at the single-cell level using an electroactive double-well array," *Lab on a Chip*, vol. 16, no. 13, pp. 2440–2449, 2016, doi: 10.1039/c6lc00241b.

[96] D. K. Wood, D. M. Weingeist, S. N. Bhatia, and B. P. Engelward, "Single cell trapping and DNA damage analysis using microwell arrays," *Proc Natl Acad Sci USA*, vol. 107, no. 22, pp. 10008–10013, 2010, doi: 10.1073/pnas.1004056107.

[97] H.-C. Moeller, M. Mian, S. Shrivastava, B. G. Chung, and A. Khademhosseini, "A microwell array system for stem cell culture," *Biomaterials*, vol. 29, no. 6, pp. 752–763, 2008, doi: 10.1161/CIRCULATIONAHA.110.956839.

[98] J. Yuan and P. A. Sims, "An Automated Microwell Platform for Large-Scale Single Cell RNA-Seq," *Scientific Reports*, vol. 6, no. June, pp. 1–10, 2016, doi: 10.1038/srep33883.

[99] K. Patel *et al.*, "Automated Digital Microfluidic Sample Preparation for Next generation DNA sequencing," *Journal of Laboratory Automation*, vol. 16, no. 6, pp. 405–414, 2011, doi: 10.1016/j.jala.2011.07.001.

[100] B. Cordovez, D. Psaltis, and D. Erickson, "Trapping and storage of particles in electroactive microwells," *Applied Physics Letters*, vol. 90, no. 2, pp. 7–10, 2007, doi: 10.1063/1.2430775.

[101] S. H. Kim, T. Yamamoto, D. Fourmy, and T. Fujii, "Electroactive microwell arrays for highly efficient single-cell trapping and analysis," *Small*, vol. 7, no. 22, pp. 3239–3247, 2011, doi: 10.1002/smll.201101028.

[102] A. Mansoorifar, A. Koklu, A. C. Sabuncu, and A. Beskok, "Dielectrophoresis assisted loading and unloading of microwells for impedance spectroscopy," *Electrophoresis*, vol. 38, no. 11, pp. 1466–1474, 2017, doi: 10.1002/elps.201700020.

[103] G. N. Abdelrasoul *et al.*, "DNA aptamer-based non-faradaic impedance biosensor for detecting *E. coli*," *Analytica Chimica Acta*, vol. 1107, pp. 135–144, 2020, doi: 10.1016/j.aca.2020.02.004.

[104] C. Polonschii, S. David, S. Gáspár, M. Gheorghiu, M. Rosu-Hamzescu, and E. Gheorghiu, "Complementarity of EIS and SPR to reveal specific and nonspecific binding when interrogating a model bioaffinity sensor; Perspective offered by plasmonic based EIS," *Analytical Chemistry*, vol. 86, no. 17, pp. 8553–8562, 2014, doi: 10.1021/ac501348n.

[105] G. N. Abdelrasoul *et al.*, "Non-invasive Point-of-Care Device to Diagnose Acute Mesenteric Ischemia," *ACS Sensors*, vol. 3, no. 11, pp. 2293–2302, 2018, doi: 10.1021/acssensors.8b00558.

[106] Y. Ren *et al.*, "A Simple and Reliable PDMS and SU-8 Irreversible Bonding Method and Its Application on a Microfluidic-MEA Device for Neuroscience Research," *Micromachines (Basel)*, vol. 6, no. 12, pp. 1923–1934, 2015, doi: 10.3390/mi6121465.

[107] H. Bruus, "Acoustofluidics 1: Governing equations in microfluidics," *Lab on a Chip*, vol. 11, no. 22, pp. 3742–3751, 2011, doi: 10.1039/c1lc20658c.

[108] N. Couniot, D. Flandre, L. A. Francis, and A. Afzalian, "Signal-to-noise ratio optimization for detecting bacteria with interdigitated microelectrodes," *Sensors and Actuators, B: Chemical*, vol. 189, pp. 43–51, 2013, doi: 10.1016/j.snb.2012.12.008.

[109] X. Guo, R. Zhu, and X. Zong, "A microchip integrating cell array positioning with *in situ* single-cell impedance measurement," *Analyst*, vol. 140, no. 19, pp. 6571–6578, 2015, doi: 10.1039/c5an01193k.

[110] A. Mansoorifar, A. Koklu, and A. Beskok, "Quantification of cell death using an impedance-based microfluidic device," *Analytical Chemistry*, vol. 91, no. 6, pp. 4140–4148, 2019, doi: 10.1021/acs.analchem.8b05890.

[111] L. Menze, "Development of a Multisectorial Electroactive Nanowell Platform for Selective Single-Cell Sorting and Quantification," M.Sc. Thesis, University of Alberta, Edmonton, 2021.

[112] L. Menze, P. A. Duarte, L. Haddon, M. Chu, and J. Chen, "Selective Single-Cell Sorting Using a Multisectorial Electroactive Nanowell Platform," *ACS Nano*, 2021, doi: 10.1021/acsnano.1c05668.

[113] P. O. Bagnaninchi and N. Drummond, "Real-time label-free monitoring of adipose-derived stem cell differentiation with electric cell-substrate impedance sensing.," *Proc Natl Acad Sci U S A*, vol. 108, no. 16, pp. 6462–6467, Apr. 2011, doi: 10.1073/pnas.1018260108.

[114] W. Liang, X. Yang, J. Wang, Y. Wang, W. Yang, and L. Liu, "Determination of dielectric properties of cells using ac electrokinetic-based microfluidic platform: A review of recent advances," *Micromachines (Basel)*, vol. 11, no. 5, 2020, doi: 10.3390/mi11050513.

[115] K. Asami, "Characterization of biological cells by dielectric spectroscopy," *Journal of Non-Crystalline Solids*, vol. 305, no. 1–3, pp. 268–277, 2002, doi: 10.1016/S0022-3093(02)01110-9.

[116] K. Heileman, J. Daoud, and M. Tabrizian, "Dielectric spectroscopy as a viable biosensing tool for cell and tissue characterization and analysis," *Biosensors and Bioelectronics*, vol. 49, pp. 348–359, 2013, doi: 10.1016/j.bios.2013.04.017.

[117] K. Asami, Y. Takahashi, and S. Takashima, "Dielectric properties of mouse lymphocytes and erythrocytes," *BBA - Molecular Cell Research*, vol. 1010, no. 1, pp. 49–55, 1989, doi: 10.1016/0167-4889(89)90183-3.

[118] T. Kakutani, S. Shibatani, and M. Sugai, "Electrorotation of non-spherical cells: Theory for ellipsoidal cells with an arbitrary number of shells," *Bioelectrochemistry and Bioenergetics*, vol. 31, no. 2, pp. 131–145, 1993, doi: 10.1016/0302-4598(93)80002-C.

[119] K. Asami, T. Hanai, and N. Koizumi, "Dielectric analysis of *Escherichia coli* suspensions in the light of the theory of interfacial polarization," *Biophysical Journal*, vol. 31, no. 2, pp. 215–228, 1980, doi: 10.1016/S0006-3495(80)85052-1.

[120] K. Asami and T. Yonezawa, "Dielectric behavior of wild-type yeast and vacuole-deficient mutant over a frequency range of 10 kHz to 10 GHz," *Biophysical Journal*, vol. 71, no. 4, pp. 2192–2200, 1996, doi: 10.1016/S0006-3495(96)79420-1.

[121] Y. Polevaya, I. Ermolina, M. Schlesinger, B. Z. Ginzburg, and Y. Feldman, "Time domain dielectric spectroscopy study of human cells II. Normal and malignant white blood cells," *Biochimica et Biophysica Acta - Biomembranes*, vol. 1419, no. 2, pp. 257–271, 1999, doi: 10.1016/S0005-2736(99)00072-3.

[122] F. Bordi, C. Cametti, and A. Di Biasio, "Determination of cell membrane passive electrical properties using frequency domain dielectric spectroscopy technique. A new approach," *BBA - Biomembranes*, vol. 1028, no. 2, pp. 201–204, 1990, doi: 10.1016/0005-2736(90)90154-G.

[123] J. Yang, Y. Huang, X. Wang, X. B. Wang, F. F. Becker, and P. R. C. Gascoyne, "Dielectric properties of human leukocyte subpopulations determined by electrorotation as a cell separation criterion," *Biophysical Journal*, vol. 76, no. 6, pp. 3307–3314, 1999, doi: 10.1016/S0006-3495(99)77483-7.

[124] M. B. Sano, E. A. Henslee, E. Schmelz, and R. V. Davalos, "Contactless dielectrophoretic spectroscopy: Examination of the dielectric properties of cells found in blood," *Electrophoresis*, vol. 32, no. 22, pp. 3164–3171, 2011, doi: 10.1002/elps.201100351.

[125] C. Vaillier, T. Honegger, F. Kermarrec, X. Gidrol, and D. Peyrade, "Label-Free Electric Monitoring of Human Cancer Cells as a Potential Diagnostic Tool," *Analytical Chemistry*, vol. 88, no. 18, pp. 9022–9028, 2016, doi: 10.1021/acs.analchem.6b01648.

[126] K. V. Kaler and T. B. Jones, "Dielectrophoretic spectra of single cells determined by feedback-controlled levitation," *Biophysical Journal*, vol. 57, no. 2, pp. 173–182, 1990, doi: 10.1016/S0006-3495(90)82520-0.

[127] Y. Huang, R. Holzel, R. Pethig, and Xiao-B.Wang, "Differences in the AC electrodynamics of viable and non-viable yeast cells determined through combined dielectrophoresis and electrorotation studies," *Physics in Medicine and Biology*, vol. 37, no. 7, pp. 1499–1517, 1992, doi: 10.1088/0031-9155/37/7/003.

[128] W. M. Arnold and U. Zimmermann, "Rotating-field-induced rotation and measurement of the membrane capacitance of single mesophyll cells of Avena sativa," *Zeitschrift fur Naturforschung - Section C Journal of Biosciences*, vol. 37, no. 10, pp. 908–915, 1982, doi: 10.1515/znc-1982-1010.

[129] P. Marszalek, J. J. Zielinsky, M. Fikus, and T. Y. Tsong, "Determination of electric parameters of cell membranes by a dielectrophoresis method," *Biophysical Journal*, vol. 59, no. 5, pp. 982–987, 1991, doi: 10.1016/S0006-3495(91)82312-8.

[130] A. Rosenthal and J. Voldman, "Dielectrophoretic traps for single-particle patterning," *Biophysical Journal*, vol. 88, no. 3, pp. 2193–2205, 2005, doi: 10.1529/biophysj.104.049684.

[131] Y. J. Lo, Y. Y. Lin, U. Lei, M. S. Wu, and P. C. Yang, "Measurement of the Clausius-Mossotti factor of generalized dielectrophoresis," *Applied Physics Letters*, vol. 104, no. 8, pp. 1–6, 2014, doi: 10.1063/1.4866344.

[132] L. Wu, L. Y. Lanry Yung, and K. M. Lim, "Dielectrophoretic capture voltage spectrum for measurement of dielectric properties and separation of cancer cells," *Biomicrofluidics*, vol. 6, no. 1, pp. 1–10, 2012, doi: 10.1063/1.3690470.

[133] P. Han *et al.*, "Continuous Label-Free Electronic Discrimination of T Cells by Activation State," *ACS Nano*, vol. 14, no. 7, pp. 8646–8657, 2020, doi: 10.1021/acsnano.0c03018.

[134] J. Chen, S. MacKay, and Y. Feng, *Bionanotechnology: Engineering Concepts and Applications*, 1st ed., vol. 1. McGraw Hill, 2021.

[135] A. J. Goldman, R. G. Cox, and H. Brenner, "Slow viscous motion of a sphere parallel to a plane wall-II Couette flow," *Chemical Engineering Science*, vol. 22, no. 4, pp. 653–660, 1967, doi: 10.1016/0009-2509(67)80048-4.

[136] L. Korson, W. Drost-Hansen, and F. J. Millero, "Viscosity of water at various temperatures," *Journal of Physical Chemistry*, vol. 73, no. 1, pp. 34–39, 1969, doi: 10.1021/J100721A006/ASSET/J100721A006.FP.PNG_V03.

[137] R. Soffe, S. Baratchi, S. Y. Tang, P. Mcintyre, A. Mitchell, and K. Khoshmanesh, "Discontinuous dielectrophoresis a technique for investigating the response of loosely adherent cells to high shear stress," *BIODEVICES 2016 - 9th International Conference on Biomedical Electronics and Devices, Proceedings; Part of 9th International Joint Conference on Biomedical Engineering Systems and Technologies, BIOSTEC 2016*, vol. 1, no. Biostec, pp. 23–33, 2016, doi: 10.5220/0005654700230033.

[138] A. El-Gaddar, M. Frénéa-Robin, D. Voyer, H. Aka, N. Haddour, and L. Krähenbühl, "Assessment of 0.5 T static field exposure effect on yeast and HEK cells using electrorotation," *Biophysical Journal*, vol. 104, no. 8, pp. 1805–1811, 2013, doi: 10.1016/j.bpj.2013.01.063.

[139] G. Le Brun, M. Hauwaert, A. Leprince, K. Glinel, J. Mahillon, and J. P. Raskin, "Electrical Characterization of Cellulose-Based Membranes towards Pathogen Detection in Water," *Biosensors (Basel)*, vol. 11, no. 2, 2021, doi: 10.3390/bios11020057.

[140] T. N. G. Adams, P. A. Turner, A. V. Janorkar, F. Zhao, and A. R. Minerick, "Characterizing the dielectric properties of human mesenchymal stem cells and the effects of charged

elastin-like polypeptide copolymer treatment," *Biomicrofluidics*, vol. 8, no. 5, pp. 1–14, 2014, doi: 10.1063/1.4895756.

[141] C. Y. Yang and U. Lei, "Quasistatic force and torque on ellipsoidal particles under generalized dielectrophoresis," *Journal of Applied Physics*, vol. 102, no. 9, 2007.

[142] N. M. Figueiredo and A. Cavaleiro, "Dielectric Properties of Shape-Distributed Ellipsoidal Particle Systems," *Plasmonics*, vol. 15, no. 2, pp. 379–397, Apr. 2020, doi: 10.1007/s11468-019-01051-3.

[143] C. W. Einolf and E. L. Carstensen, "Passive electrical properties of microorganisms. IV. Studies of the protoplasts of *Micrococcus lysodeikticus*," *Biophys J*, vol. 9, no. 4, pp. 634–643, 1969, doi: 10.1016/S0006-3495(69)86408-8.

[144] A. R. Hyler, D. Hong, R. V. Davalos, N. S. Swami, and E. M. Schmelz, "A novel ultralow conductivity electromanipulation buffer improves cell viability and enhances dielectrophoretic consistency," *Electrophoresis*, vol. 42, no. 12–13, pp. 1366–1377, 2021, doi: 10.1002/elps.202000324.

Appendix A
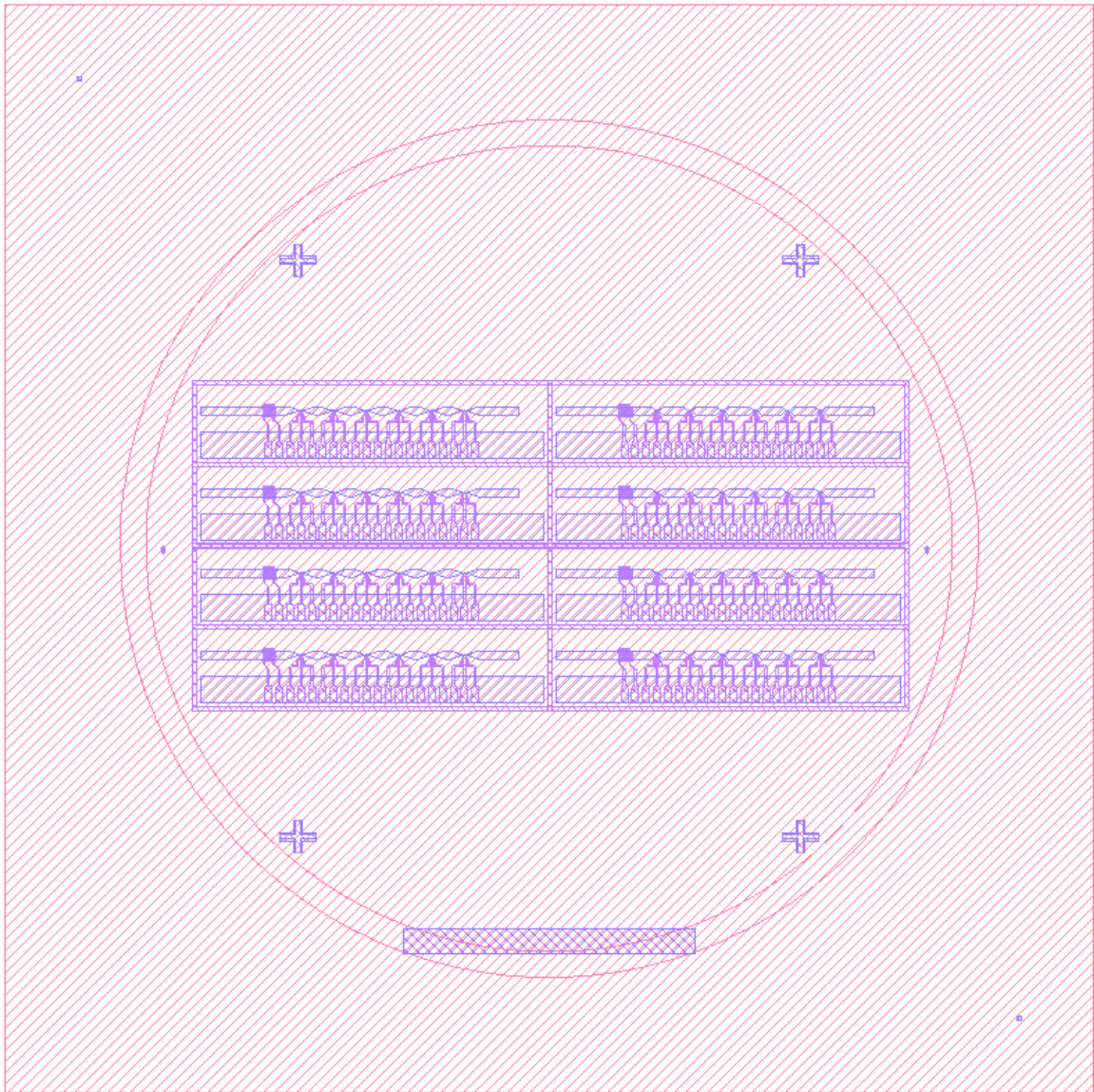
Figure A. 1: Mask design of the Coulter counter chip. Each wafer provides 8 chips
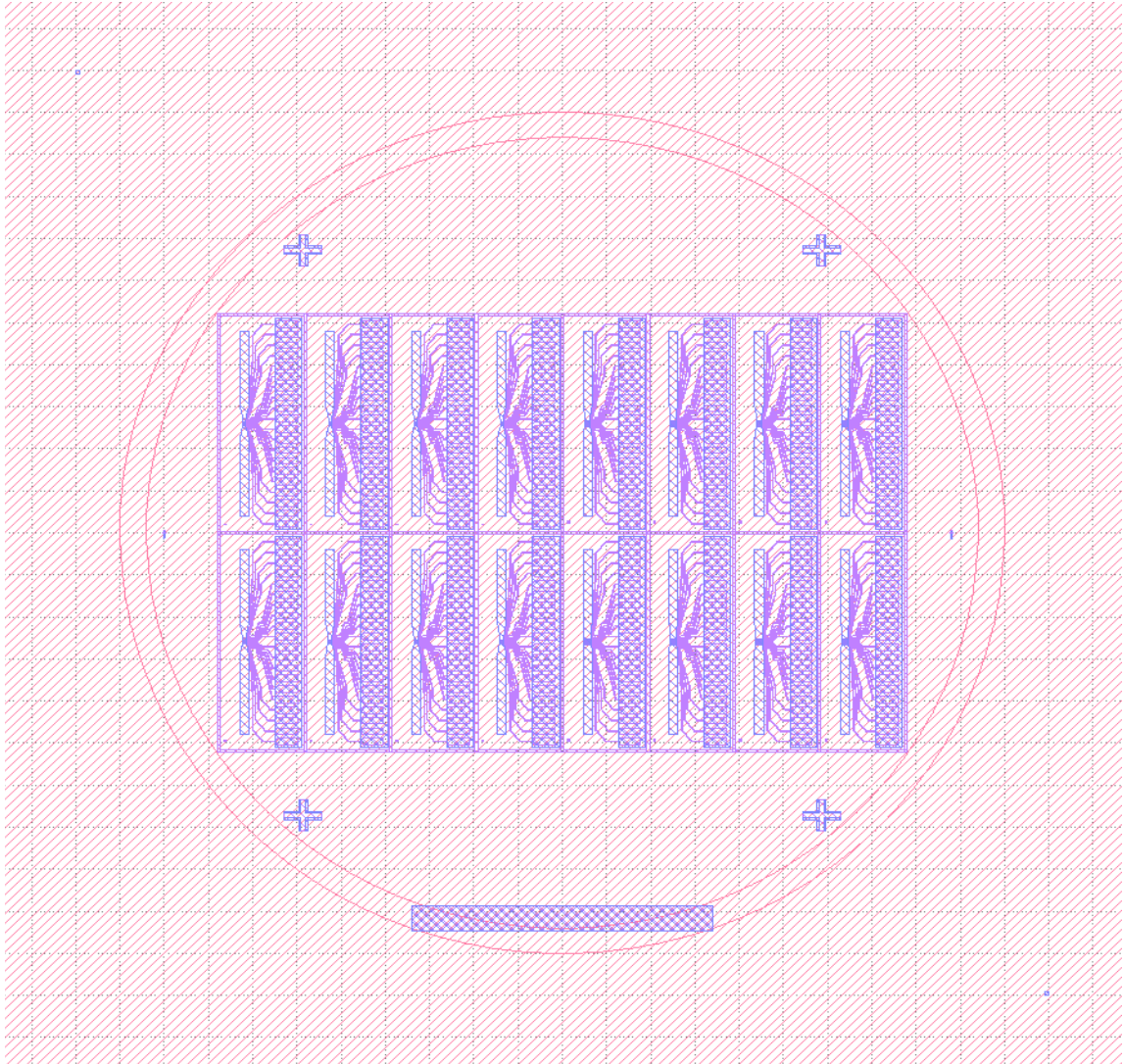
Figure A. 2: Mask design of the validation chip based on microwells. Each wafer provided 16 chips
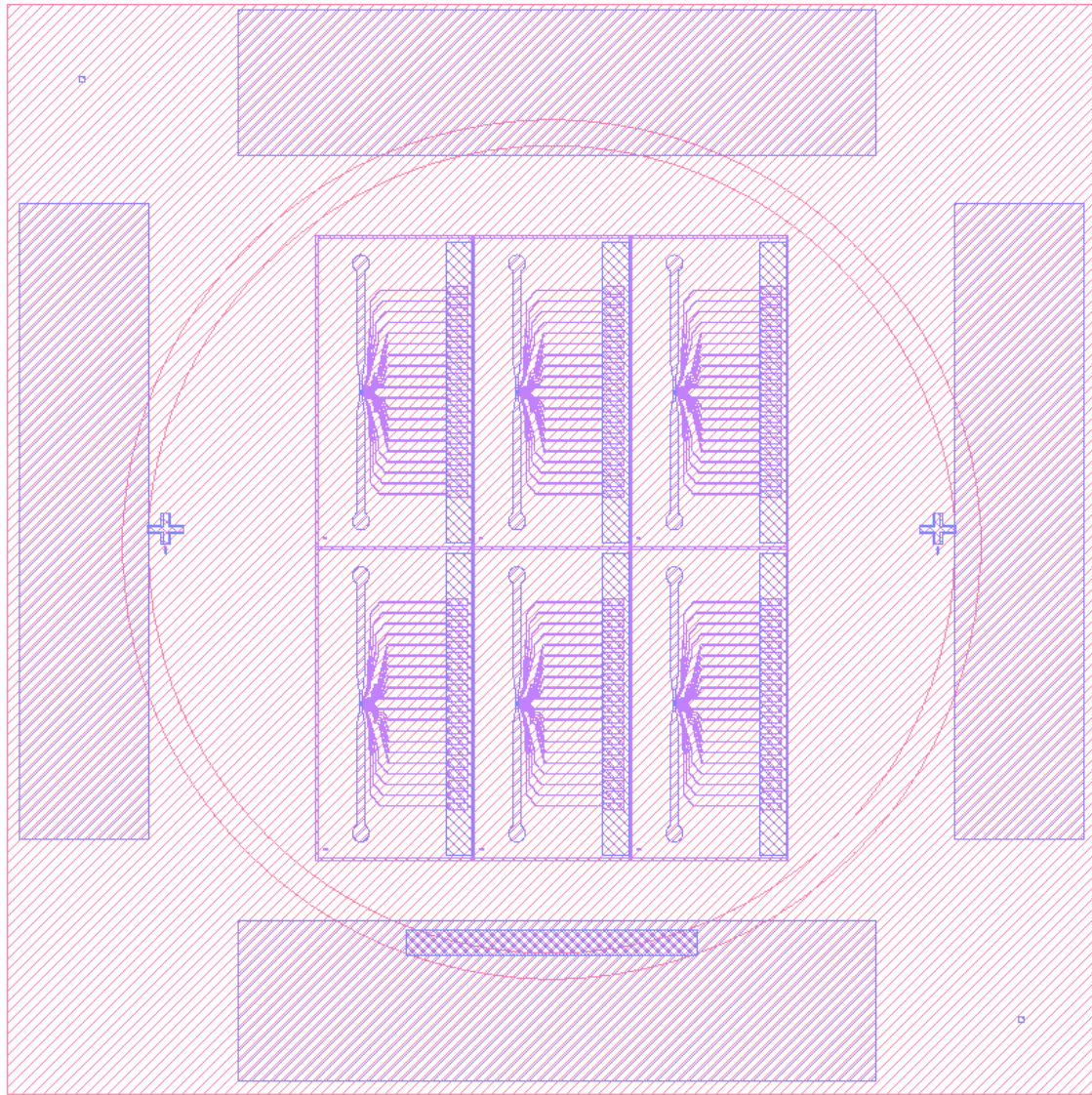
Figure A. 3: Mask design of the chip based on microwells. Each wafer provided 6 chips, 3 chips have microwells with 20 µm diameter and 3 have 15 µm in diameter.
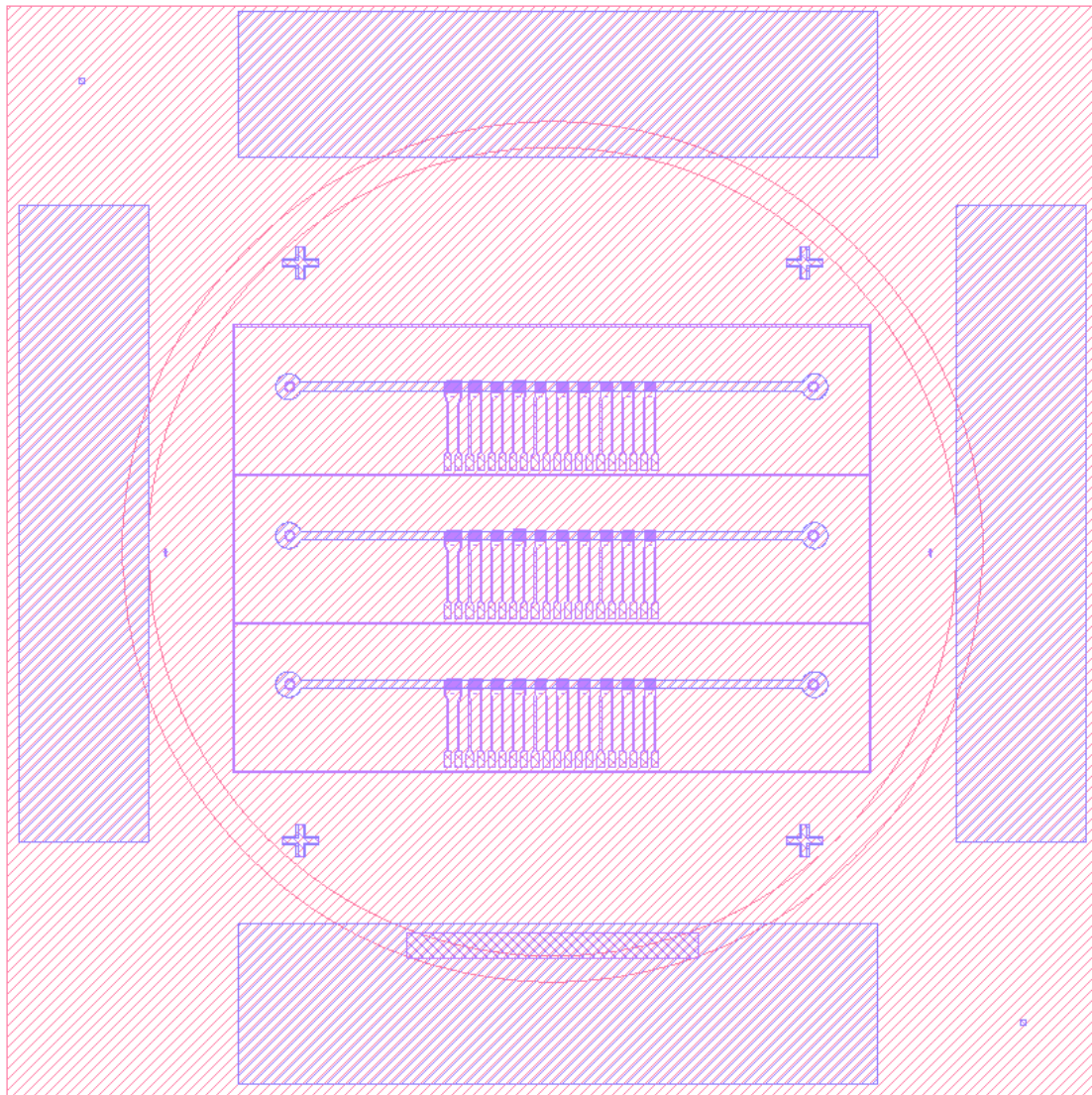
Figure A. 4: Mask design of the chip employed for the dielectric characterization of *S. sclerotiorum* ascospores.